ELNES INVESTIGATIONS OF SPINELS

by Frances Thérèse Docherty

Submitted for the degree of Ph.D. at the University of Glasgow.

April 2001

Acknowledgements

A number of people have helped me during this thesis. In particular I would like to thank Professor A.J. Craven and Dr. D.W. McComb for their advice and invaluable discussions. I am also grateful to Dr. W.A.P. Nicholson and Dr. M. MacKenzie for training and assistance in operating the HB5 microscope. The technical staff of the solid state physics group at the University of Glasgow have provided excellent support, in particular Dr. S. McFadzean, for maintenance of the HB5 STEM.

A number of people outwith my own group have also provided invaluable assistance. Professor A.R. West, Dr J. Skakle and Mr. J. Marr of the solid state chemistry group at the University of Aberdeen provided expertise and use of facilities for the syntheses of the spinels. Dr. Skakle also assisted with collection and refinement of the X-ray and neutron diffraction data. Dr. R. Smith of the ISIS facility at Rutherford Appleton Laboratory also assisted with the neutron diffraction data, and Mr. W. Higgison of the Department of Geology at the University of Glasgow provided training in the use of their X-ray diffractometer. I would also like to thank Dr. D. Apperley of the University of Durham for use of their NMR service, and Dr. I.P. Parkin of the Department of Chemistry of University College London for providing a sample of magnesium ferrite spinel.

I am also grateful to the University of Glasgow for the provision of a scholarship, and to the EPSRC for time at ISIS to carry out the neutron diffraction experiments.

Finally I would like to thank my family, especially my parents Mary and Frederick Docherty for their continual support and encouragement which has allowed me to undertake this work.

Declaration

This thesis is a record of the work carried out by me in the Department of Chemistry and the Department of Physics and Astronomy at the University of Glasgow. The work described herein is my own. Some of the work given in this thesis can be found in the following papers:

"ELNES Investigations of the structure and electronic properties of chromium spinels", F.T. Docherty, and D.W. McComb, Inst. Phys. Conf. Ser. (1999) **161** 203.

"ELNES investigations of the oxygen K-edge in spinels", F.T. Docherty, A.J. Craven, D.W. McComb and J. Skakle, Ultramicroscopy (2001) **86** 273.

This thesis has not previously been submitted for a higher degree.

Summary

Electron energy loss spectroscopy (EELS) provides information about the energy loss suffered by primary electrons when they interact with a specimen. The resulting energy loss spectrum contains edges due to the excitation of core electrons to unoccupied states in the conduction band. These edges exhibit fine structure, known as energy-loss near-edge structure (ELNES), which is dependent on the local chemical and structural environment of the absorbing atom.

The interactions that cause ELNES are complex and not well understood, making the interpretation of the fine structure from complex materials very difficult. The understanding of this technique can be improved by examining data collected from a series of compounds with the same crystal structure, to investigate the effect on the fine structure of changing the element in a specific crystallographic site. Further understanding can also be obtained by modelling the fine structure and investigating how changes in the model modify the spectral features.

The aim of this project is to improve the understanding of the fundamental interactions which cause ELNES by collecting and modelling the near-edge structure from a series of spinels, which have the general formula AB_2O_4. Chapter 1 provides an introduction to the theory of ELNES and reviews studies of this type which have been carried out previously. It also gives an introduction to the structure and chemistry of spinels and details the experiments planned in this study.

In chapter 2 a detailed description is given of the key features of the HB5 scanning transmission electron microscope (STEM) used to acquire EELS data, and the mode of operation used. This chapter finishes with an account of how the data was acquired, and the processing routine employed.

A discussion of the three main methods used to model the fine structure is given at the start of chapter 3. It is followed by a more detailed description of the multiple scattering technique, and the FEFF code, which was exclusively used to simulate the fine structure.

Chapter 4 describes the syntheses of most of the spinels used in this study. Since these materials are used as standards in the EELS experiments, it is crucial that they are well characterised. This chapter therefore also describes the characterisation techniques employed, including X-ray and neutron diffraction, energy-dispersive X-ray analysis (EDX) and nuclear magnetic resonance (NMR). Information on structural parameters and purity was obtained from these techniques and where possible the results from different methods are compared and found to be consistent.

The ELNES data recorded is first presented in chapters 5 and 6. In both chapters attempts have been made to correlate the observed features in the ELNES with the structural information obtained in chapter 4. Chapter 5 explores the oxygen K-edges from all of the spinels synthesised. Extra fine structure in the region up to 10eV beyond the edge onset is observed for the chromium and iron-containing compounds, and is assigned to transitions to states created by mixing of oxygen

2p and metal 3d orbitals. The possible fingerprints in the oxygen K-edge ELNES corresponding to a high degree of inversion in the spinel structure and for tetragonal distortions of the cubic structure are discussed. Simulations of the experimental data using the multiple scattering code FEFF8 are also presented in this chapter. Good agreement was obtained in the case of magnesium aluminate, but relatively poor agreement was obtained in the cases of the chromites and ferrites. It is though that this may be due to the influence of factors such as magnetic effects which are not considered in the calculations.

For a full interpretation of the ELNES present on the oxygen K-edges, the cation edges must also be considered. These are addressed in chapter 6. The first part of this chapter compares the L_3 and L_2-edges recorded in this study with simulations from the literature. The relationship between the intensity of these edges and the number of d-holes in the metal, and the pairing of the d-electrons is then explored. The methods available to obtain the intensities of these edges, and the difficulties encountered are discussed. The second part of this chapter presents the magnesium and aluminium K-edges acquired. The fine structure recorded in this study is compared to examples from the literature recorded from materials in which the magnesium and aluminium ions are in similar co-ordination environments to these ions in the spinel structure.

Chapter 7 compares some of the oxygen edges and metal edges recorded to investigate the consistency of the information obtained from each type of site. The findings of the study are summarised in chapter 8 and suggestions for further work that could undertaken are made.

Contents

Chapter 1

Introduction

1.1 Background

In 1925 de Broglie postulated that electrons have wave-like characteristics, and this was subsequently demonstrated by Davisson and Germer (1927) and Thompson and Reid (1927). Since electrons have a shorter wavelength than light, and are charged particles that can be guided in a controlled manner, the concept of the electron microscope soon evolved. Knoll and Ruska reported the first such instrument in 1932, and within a year the resolution limit attainable by light microscopy had been surpassed.

A variety of types of interactions can occur between the incident electrons and the atoms in the sample. These can generally be classified into two types: elastic

and inelastic. When electrons are elastically scattered their energy remains essentially constant, but the direction of their trajectory changes. During inelastic scattering the magnitude of the velocity of the electron is altered and its kinetic energy is reduced. A number of techniques have been developed which are based on specific types of interactions. Traditionally electron microscopy was dominated by the use of the direct and diffracted electron beams. However, it was discovered that a lot of information about the sample could be obtained from the inelastically scattered electrons, and the consequent secondary emission generated when energy was given to atoms in the sample. The study of these interactions forms the basis of analytical electron microscopy. The aim of this thesis has been to develop a better understanding of the fundamental interactions that occur in the technique of energy-loss near-edge structure (ELNES). This technique is part of the field of electron-energy loss spectroscopy (EELS), in which the energy lost by incident electrons during inelastic scattering processes is analysed. This chapter will give an overview of this technique, discuss the aims of the project, and describe the chemistry of the materials analysed in this study.

1.2 Energy-loss near-edge structure

1.2.1 Basic principles

EELS is a powerful analytical technique that provides information about the energy-loss suffered by electrons as they interact with a specimen. It can be

utilised to obtain information on the structure, bonding and electronic properties of a material (Egerton, 1996). The basic principle of the technique is to direct fast electrons of a known energy at a sample that is thin enough for the electrons to pass through. The interactions of the fast electrons with the specimen result in excitations of electrons in the sample into unoccupied energy levels in the conduction band. A spectrum is obtained by analysing the energy lost by the incident electrons.

A typical energy-loss spectrum can be divided into three main regions. Figure 1.1 shows a spectrum recorded from a transition metal nitride (Garvie *et al*, 1994). The most intense feature is the zero-loss peak, which is the signal from the fast electrons that have lost no detectable amount of energy as they passed through the sample. In the region up to an energy-loss of ~50eV the spectrum is dominated by collective excitations of the valence electron density *i.e.* plasmons. At higher energy-losses ionisation edges occur due to excitation of core electrons into the conduction band.

When observed at high enough energy resolution, two types of fine structure can be observed on the ionisation edges. Energy loss near-edge structure (ELNES) is intensity variation within ~30-50eV of the edge onset. Extended energy loss fine structure (EXELFS) is a much weaker feature observed from the end of the ELNES region to many hundreds of eV beyond the edge threshold. As will be discussed in section 1.4.2, the fine structure is a direct measure of the unoccupied density of states (DOS) of the excited atom. Since the distribution of unoccupied energy levels in an atom is influenced by its local electronic and structural

chemistry, analysis of the fine structure shows promise as a technique for investigating the chemistry of materials. Because the EXELFS signals are so weak they are often obscured by edges at higher energies, severely restricting the usefulness of this technique. ELNES, however, can be related to the electronic and structural chemistry of the atom.

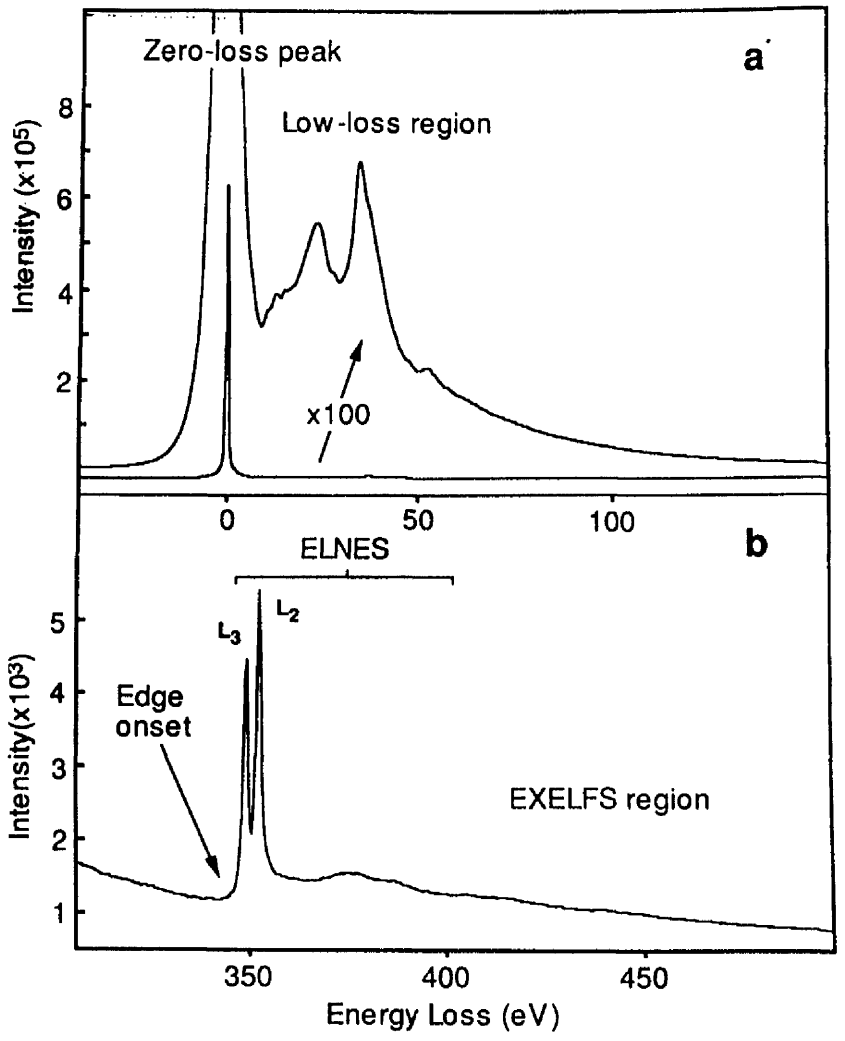

Figure 1.1 *A typical electron energy-loss spectrum from a transition metal nitride. The main features are the zero-loss peak, the low-loss region and the edges resulting from the excitation of core electrons. The core-loss region has been enlarged in b to show the fine structure.*

An advantage of this technique compared to bulk characterisation methods is that the fast electron must pass very close to the atom in order to excite a core electron, so ELNES can be obtained with very high spatial resolution by performing the technique in a modern analytical electron microscope. This means the variation in the chemistry of a material over a range of less than a nanometre can be studied. This is particularly useful in a variety of situations. For example, in the study of many technologically important materials that have interfaces, such as semiconductors, a sufficiently high spatial resolution can be attained to gain an understanding of the chemistry across the interface. The high spatial resolution attainable in the electron microscope means that ELNES shows great promise as a probe of the chemistry of materials on a sub-nanometer scale.

1.2.2 Limitations of the technique

Unfortunately the interactions which cause ELNES are complex and not well understood, making the interpretation of fine structure data difficult for poorly characterised materials. One approach to improving understanding of ELNES is to collect "fingerprints" from atoms in a well-defined environment from a number of samples with the atom in the same surrounding in each specimen, and attempt to identify features in the spectra which indicate the presence of an atom in that environment. This method can be complemented by simulating the near-edge structure and investigating how changes in the model modify spectral features. The main simulation methods used to do this will be discussed in chapter 3.

A number of studies of families of compounds with the same type of structure or general formula have been undertaken to improve our understanding of near edge structure by looking for trends as the metal in the structure is varied. For example, a number of binary metal oxides have been investigated by Paterson and Krivanek (1990) and Krivanek and Paterson (1990), Leapman *et al*, (1982), Weng and Rez (1998) and de Groot *et al* (1989). Craven (1995) has reported similar studies on transition metal carbides and nitrides. A logical progression is to study a family of metal oxides containing two metals and examine what effect the second metal has on the fine structure. Some work of this type has been done by McComb *et al.* (1991), who have compared the silicon L_3 and L_2 edge ELNES from a number of neosilicates in which all silicon atoms are tetrahedrally co-ordinated to oxygen. Studies of this type show a number of factors influence the fine structure, and it cannot be interpreted in terms of a simple co-ordination fingerprint.

1.3 Aims of the project

Clearly more work has to be done to understand the fine structure of series of compounds of this type if ELNES is ever to be used to characterise complex structures. The aim of the project is therefore to improve the understanding of ELNES by developing an interpretative framework for a ternary metal oxide system. Spinels are compounds with the general formula AB_2O_4 where A and B are metal ions. This class of mineral was chosen as a suitable system to study since spinels have well-defined structures which comprise of MO_4 tetrahedra and

MO_6 octahedra, where M is a metal ion. The metal ions present can be systematically varied to investigate the idea of a co-ordination fingerprint, and the incorporation of transition metals will allow the role of the occupation of the d-orbitals in perturbing the electronic structure at neighbouring sites to be investigated. An introduction to this class of material will be given in section 1.5.

It was hoped to achieve an understanding of the origins of the fine structure in this system by correlating experimental data with models of the fine structure. The remainder of this chapter will give a more detailed introduction to ELNES, and to the structure and chemistry of spinels. The final section will describe the key experiments planned, and the structure of the thesis.

1.4 Origins of the fine structure

1.4.1 General description

Egerton (1996) gives an excellent account of the theory of ELNES, and EELS in general. Therefore only the key points pertinent to the understanding of the interpretation of the fine structure presented in this thesis will be briefly discussed in this section.

Core-loss edges result from the excitation of a core electron from its initial state into one of the many unoccupied states in the conduction band. The minimum

energy required for this transition is the binding energy of the subshell. The inner shell binding energy depends on the atomic number of the atom from which the electron is excited, so core loss edges can be used for elemental analysis. Unlike some other compositional determination techniques, EELS can identify and measure the amount of almost all of the light elements in a sample, so a complete quantified compositional analysis can be obtained by this method.

The fast incident electron may impart more energy to the core electron than the minimum required for excitation to the lowest unoccupied level, so the signal is not confined to a peak, but extends beyond the threshold. The final state of the core electron is one in a range of unoccupied states in the conduction band. It will preferentially reside in regions with high densities of empty states. The greatest probability of electrons filling certain unoccupied states, results in the intensity in the ionisation edges being greatest at the corresponding energy levels above the Fermi level. Therefore ELNES is a probe of the density of unoccupied states. The energy level distribution is easily perturbed by changes in the atom's local environment, and this consequently alters the fine structure. Thus interpretation of near-edge structure can provide information about structure, bonding and co-ordination in the vicinity of the atom.

1.4.2 Transition probabilities and the dipole selection rule

The probability of a core electron being excited into a particular unoccupied state in the conduction band can be obtained by considering Fermi's golden rule of

quantum mechanics. This rule gives an expression for the differential cross section for scattering with momentum transfer q as

$$\frac{d^2I}{d\Omega dE} = \frac{4\gamma^2}{a_o^2 q^4} \left| < f \left| \exp(iq.r) \right| i > \right|^2 \rho(E) \qquad (1.1)$$

where $|i\rangle$ represents the inner shell electron wavefunction

$|f\rangle$ represents the final unoccupied state wavefunction

and $\rho(E)$ is the density of states for final state electrons with energy E.

The operator in Equation 1.1 can be expanded as

$$exp(iq.r) = 1 + i(q.r) + \text{higher order terms} \qquad (1.2)$$

so Equation 1.1 can be expressed as the sum of three terms. The first of these, arising from the unity term in Equation 1.2, will be zero since the final and initial states are orthogonal wavefunctions. Since $q.r$ is an odd function, the second integral containing $i(q.r)$ will be zero if the initial and final states have the same symmetry about the centre of the excited atom, such that the product is even. Therefore this term is only non-zero if one of the states has even and the other has odd symmetry. This forms the basis of the dipole selection rule, which states that $\Delta\ell = \pm 1$, where ℓ is the angular momentum quantum number. Therefore an electron in a state with *s*-like symmetry can only be excited to a *p*-like state, but an electron initially in a state with *p*-like symmetry can be excited to a state which is *s*- or *d*-like in character.

For the dipole rule to be valid the higher order terms must be negligible, so that the third integral will not contribute to the energy dependence of the fine

structure. For this to be the case requires $q.r << 1$. Collecting the signal over a limited angular range ensures that these terms are not important.

The dipole approximation means that equation 1.1 is equivalent to

$$\frac{d^2I}{d\Omega dE} \propto |M(E)|^2 \rho(E) \tag{1.3}$$

where $M(E)$ is the atomic transition matrix element representing the probability of excitation from the initial to final state. To a first approximation it can be assumed that $M(E)$, varies slowly over the 10-20eV beyond threshold. Therefore changes in the transition probability can be attributed to changes in $\rho(E)$.

As well as the symmetry considerations, the core wavefunction is assumed to be highly localised at the atomic site of the excited atom, so $\rho(E)$ must be interpreted as a site and symmetry projected density of states. The orbitals that interact to form the bands of electrons in which the electron can reside are particularly sensitive to changes in the valence of the central atom, and to local structure and bonding. This sensitivity is reflected in changes in the fine structure. Hence ELNES provides information on local structural and electronic chemistry.

1.5 Spinels

1.5.1 General structure

There are many general introductions to this class of mineral, (West, 1988; Blasse, 1964; Burdett, 1995; Wold and Dwight, 1993; Borg and Dienes, 1992; Smart and Moore, 1995). The general formula for spinel is AB_2O_4 where A is a divalent metal ion and B is a trivalent metal ion. Spinels have a cubic close packed array of oxide ions in which the cations occupy one eighth of the tetrahedral and half of the octahedral interstices.

The crystal structure is characterised by two parameters; the lattice constant *a*, and the oxygen parameter *u*. The oxygen anions form a cubic sublattice, and their positions are defined by *u*, as shown in Table 1.1 (Henry and Londsdale, 1969). In an ideal spinel $u = 0.375$, but for most spinels $u \neq 0.375$ resulting in a displacement of the oxygen ions along <111> directions. For example, an anion at 0.375 0.375 0.375 could be displaced to 0.387 0.387 0.387 in a typical spinel, *i.e.* it is displaced along the body diagonal. As *u* increases the tetrahedra expand at the expense of the octahedra, although the bond lengths in the octahedra all remain equal.

The spinel unit cell contains eight AB_2O_4 units, of which there are two types. As shown in Figure 1.2, the metal ion is tetrahedrally co-ordinated to the oxygen ions in one type of octant, and is octahedrally co-ordinated to oxygen ions in the

Atom type	Co-ordinates
Mg	0,0,0 0.25,0.25,0.25 + face centring
Al	0.625,0.625,0.625 0.375,0.875,0.125 0.875,0.125,0.375 0.125,0.375,0.875 + face centring
O	*u*,*u*,*u* -*u*,-*u*+0.5,*u*+0.5 -*u*+0.5,*u*+0.5,-*u* *u*+0.5,-*u*,-*u*+0.5 *u*+0.75,*u*+0.25,-*u*+0.75 -*u*+0.25,-*u*+0.25,-*u*+0.25 *u*+0.25,-*u*+0.75,*u*+0.75 -*u*+0.75,*u*+0.75,*u*+0.25 + face centring

Table 1.1 Cation and anion positions in an ideal normal spinel unit cell

adjoining octants. In normal spinels all B^{3+} ions are in octahedral sites, and all A^{2+} ions are in tetrahedral sites. Inverse spinels have 50% of the trivalent B ions in tetrahedral sites and the remaining 50% of the trivalent B ions, and all the divalent A ions occupying octahedral sites. Intermediate phases with random cation distributions between these two extremes also exist. These partially inverse spinels can be characterised by defining an inversion parameter, λ, which is the fraction of tetrahedral sites occupied by B^{3+} ions.

1.5.2 Deviations from ideal structure

A number of spinels which are generally thought to be completely normal or completely inverse are actually partially inverse. The degree of inversion can be influenced by a number of factors such as growth method, thermal history and impurity content of the spinel, (for example, Schmocker and Waldner, 1976).

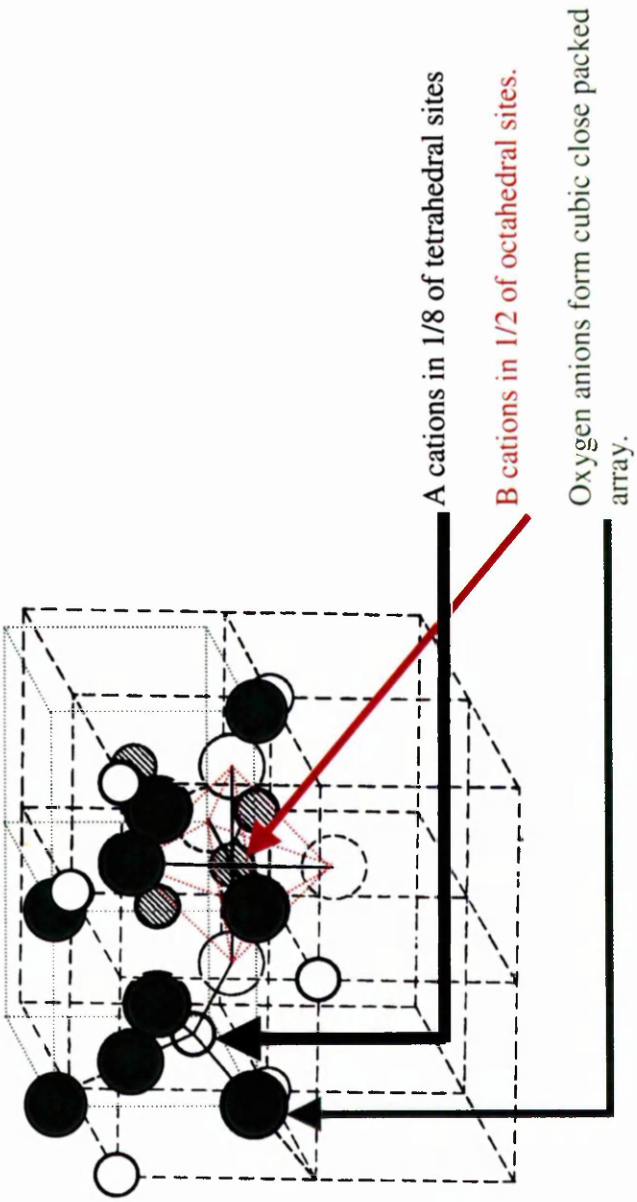

Figure 1.2 *Part of the structure of normal spinel showing the two types of AB_2O_4 units of which the structure is comprised.*

The most common methods for determining the degree of inversion are Rietveld refinement using X-ray or neutron powder diffraction data, (Peterson *et al.*, 1991; Metz *et al.*, 1989; Mocala and Navrotsky, 1989; Baudour *et al.*, 1992) and Mossbauer spectroscopy, (Banerjee *et al.*, 1967). The use of magic angle spinning nuclear magnetic resonance (NMR), (Gobbi *et al.*, 1985; Millard et *al.*, 1995), electron spin resonance (ESR), (Schmocker and Waldner,1976), extended X-ray absorption fine structure (EXAFS), (Harris *et al.*, 1997; Yao *et al.*,1991) and magnetic moment data, (West, 1988) have also been reported. Some of these techniques have been used and will be discussed in Chapter 4.

Some spinels are tetragonally distorted due to the Jahn Teller effect (Dunitz and Orgel, 1957; McClure, 1957). Large deviations from cubic symmetry are predicted for d^4 and d^9 ions in octahedral sites, and d^3, d^4, d^8 and d^9 ions in tetrahedral sites. The ratio of c/a can be greater or less than 1, depending on the type of ion and type of site involved.

If spinels are to be used as reference materials in EELS experiments, it is important that they are well characterised, and any possible structural deviations have been identified. In chapter 4 the syntheses and characterisation of the spinels studied will be described. The discrepancies from the ideal structure identified in that chapter will be considered when interpreting the ELNES data presented in Chapters 5 and 6.

1.5.3 Technological applications

It has been stated that spinels are a good ternary system to study because the ions in the octahedral and tetrahedral sites can be systematically varied and the effect on the ELNES investigated. Another reasons for choosing spinels is because they are an important class of technological materials. The most commercially important spinels are the ferrites due to their interesting electrical and magnetic properties (see, for example, West 1988). Most of these compounds have the inverse spinel structure. The chromites have been used as catalysts (see for example Aly and Baumgarten, 2001, Jebarathinam *et al*, 1994, Murthy and Ghose, 1994) and pigments (see for example Corradi *et al*, 1993). Nickel and manganese-containing spinels are also used in thermistors (see for example Torii *et al*, 1996 and Fritsch *et al*, 1998). Most of the spinels with useful applications are doped with a third metal or had some of their metal ions substituted. Therefore a solid understanding of the ELNES from simple spinels forms the first step in interpreting the data from these more complex materials.

1.6 Planned experiments

It was thought that the easiest system to understand would be the normal spinels, since the interpretation of the ELNES data would be simplified by the fact only one type of metal ion occupied each type of metal site. Chromium spinels were chosen because the chromium (III) ion has a strong preference for octahedral co-ordination. The degree of inversion is determined by a number of factors

including the Madelung energy and mixing entropy for the octahedral sites. However, in the case of the chromium spinels octahedral site preference is thought to be principally due to the much higher negative ligand field stabilisation energy (LFSE) for the Cr^{3+} ion in octahedral as opposed to tetrahedral sites (Dunitz and Orgel, 1957, Cox, 1995). Therefore the structure of these compounds is likely to be close to the ideal normal spinel, and this has been confirmed by the neutron diffraction studies discussed in section 4.3.3. No other ion present in the common spinels has such a strong preference for a particular type of site so most other spinels are likely to be at least slightly inverse. After the initial study on normal spinels the effect of inversion was considered by studying a series of aluminate and ferrite spinels in which there were normal, partially inverse and completely inverse members in each series.

Chapters 2 and 3 will describe the instrumentation used to acquire the EELS data, and the modelling techniques used to simulate them, respectively. In Chapter 4 the syntheses and characterisation of the spinels analysed will be described. The next two chapters will present and discuss the ELNES data acquired, and chapter 7 will comprise of an overall discussion of the results obtained. The final chapter will summarise the findings of the project and suggest further work that could be undertaken.

Chapter 2

Electron Energy-Loss Spectroscopy Instrumentation and Techniques

2.1 Introduction

The aim of this chapter is to describe the scanning transmission electron microscope (STEM) used to acquire the EELS data, and the particular mode of operation employed. The EELS spectrometer will also be described in detail. The remainder of the chapter will give describe the specimen preparation and give a detailed account of the parameters considered when recording the data. The data processing routine used will then be discussed. A number of accounts of the use of this STEM for acquiring PEELS data have been given previously (see for example, Garvie *et al.* 1994, Garvie and Craven, 1994 and Craven, 1995).

2.2 Instrumentation

2.2.1 The VG HB5 STEM

All EELS experiments have been conducted on the VG microscopes HB5 dedicated STEM in the Department of Physics and Astronomy in the University of Glasgow. This instrument is operated at 100kV and has been modified to include post-specimen lenses, a z-lift stage and a second condenser lens (Craven and Buggy, 1981). A schematic diagram of the main components of this microscope is shown in figure 2.1. The path of the electrons through the microscope when it is set-up for the collection of EELS data is also indicated. The dashed lines show the additional lenses present, but not employed, when acquiring EELS data.

The electron source is a cold field emission gun (FEG) that can produce a small highly convergent electron beam with much higher intensity than from thermionic sources. It is made from a pointed (310) orientation single crystal of tungsten, which has a low work function, and has been sharpened electrolytically. The extremely sharp tip allows the generation of a very high electric field, since

$$E = \frac{V}{r} \tag{2.1}$$

where r is the radius of curvature of the tip, typically less than 0.1μm, and V is the applied voltage, which is of the order of 4kV. The high electric field induces quantum tunnelling of electrons. The FEG requires an operating vacuum of the order 10^{-11}mbar. Gas adsorbed on the tip raises the work function of the tungsten crystal, thus decreasing the current intensity. This is regularly removed by passing a high current through the

wires supporting the crystal to remove the contaminants, and is known as "flashing" the tip.

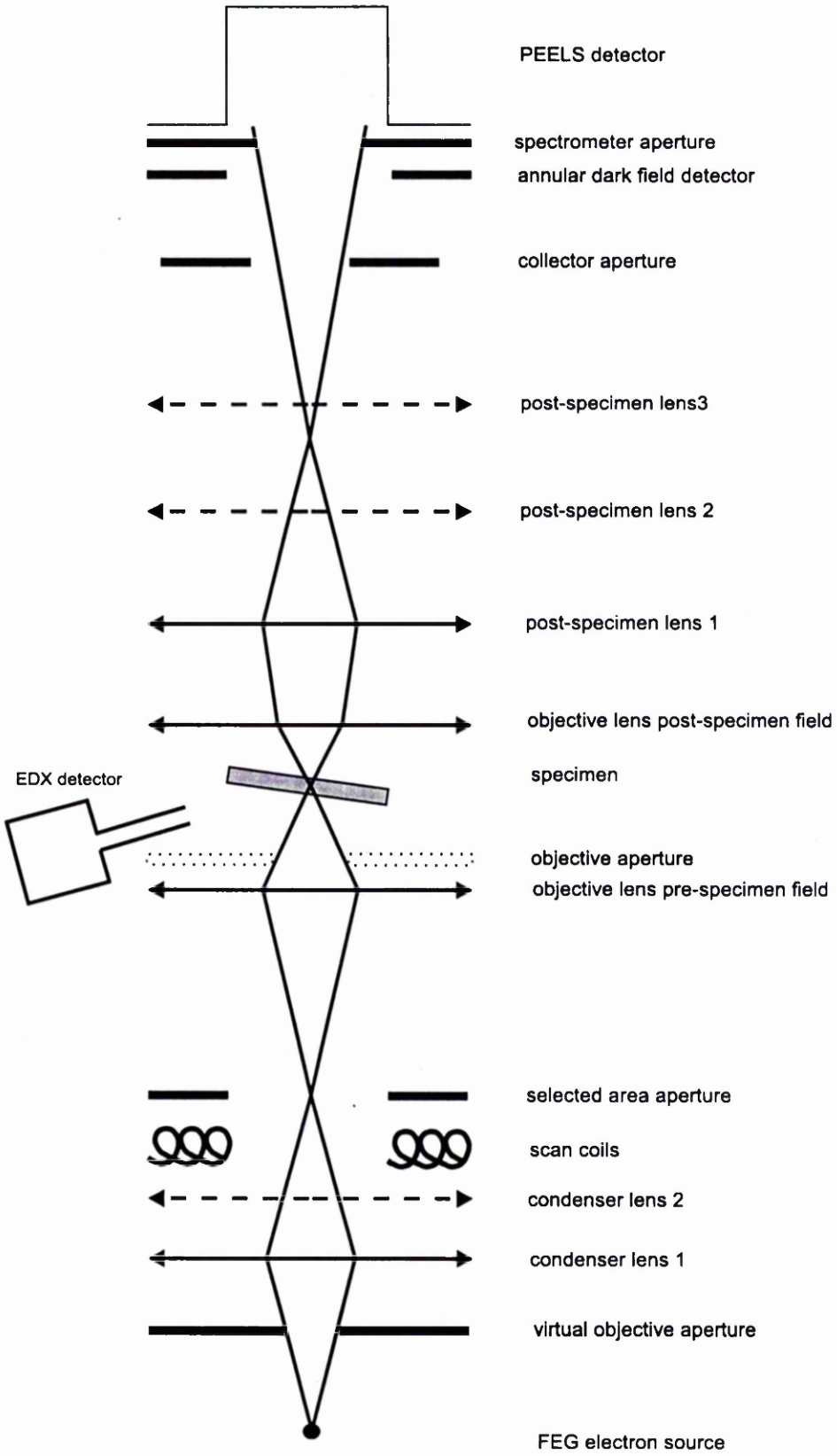

Figure 2.1 *The main components of the HB5 STEM. The lenses represented by dashed lines are not in use when acquiring EELS data.*

The main chamber of the microscope operates with a vacuum of the order of 10^{-8}mbar. A differential pumping aperture between the gun and main chamber protects the ultra-high vacuum required by the gun. There is a very low leakage rate of molecules from the chamber to the gun, whilst the electron beam is not impeded by this aperture.

The virtual objective aperture (VOA) is a beam-defining aperture situated before the condenser lenses. Under particular operating conditions the VOA can be electron optically regarded as a replacement real objective aperture (ROA). This is particularly useful for energy-dispersive X-ray analysis (EDX), since the ROA is close to the specimen in the STEM, and can give rise to a large contribution to the EDX spectrum due to stray scattering.

Only condenser lens C1 is employed for analytical electron microscopy. It is focussed so that the image plane is coplanar with the selected area aperture (SA) and thus allows the removal of stray electrons. It also allows an image of the edge of the aperture to be used to correct the condenser astigmatism. The specimen sits close to the centre of the objective lens field. An optimum standard lens setting is always employed, and the sample is moved up or down in the z-direction to attain best focus at this current setting.

Three post-specimen lenses can provide varying degrees of angular compression of the electron beam. The first post-specimen lens produces an angular compression of ten, which is the greatest possible with the Gatan 666 spectrometer, and is therefore used to obtain the largest possible signal for EELS. After the post-specimen lenses there is a collector aperture (CA) which defines the entrance angle into the spectrometer. An image of the area being analysed can be obtained using a bright field, or one of two

annular dark field (ADF) detectors which are situated after the CA. These detectors are scintillators, placed concentrically about the optic axis, which emit photons when hit by an electron. The photon signals are amplified in a photomultiplier, and the display is generated as in a normal SEM (Goldstein, 1992). A spectrometer aperture, is located after the bright and dark field detectors. It acts as a spray aperture and removes any stray electrons before the spectrometer entrance.

The HB5 is also fitted with a lithium-doped silicon energy-dispersive X-ray analysis (EDX) detector, fitted with a beryllium window. The EDX detectors and procedures used will be described in section 4.4.

2.2.2 The PEELS Spectrometer

The main components of the Gatan 666 parallel recording spectrometer used are shown in figure 2.2. The object plane for the spectrometer is the image of the source formed by post-specimen lens 1. Two pre-spectrometer quadrupole lenses can be adjusted to ensure the source is focussed on the detector. The electrons pass through an electrically isolated drift tube, and are deflected as they pass through a magnetic field. The electrons with the greatest energy loss are deflected most, in a process that is analogous to the splitting of white light in a prism. In the perpendicular direction the electrons off axis experience a restoring force at the entrance and exit of the prism, bringing them to a focal point in the dispersion plane.

The electrons reach an yttrium aluminium garnet (YAG) scintillator, which is optically coupled to a semiconductor photodiode array comprising 1024 diodes. This collection method, known as parallel electron energy loss spectroscopy (PEELS), allows the

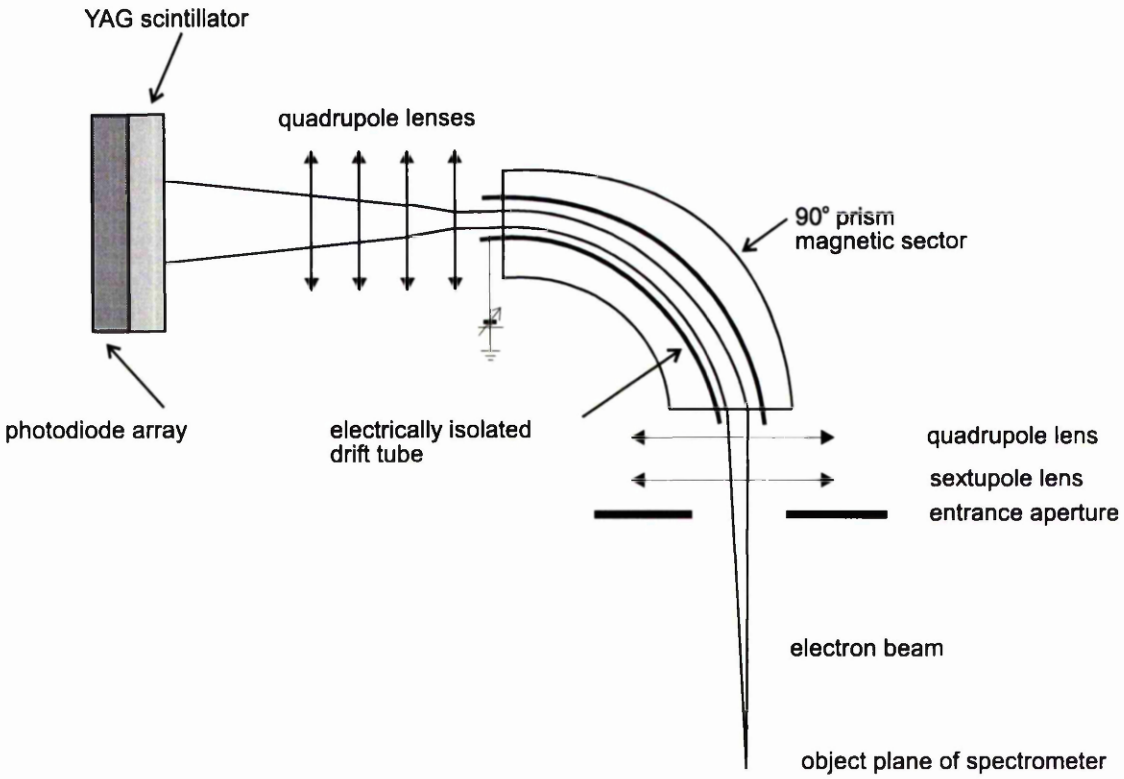

Figure 2.2 The main features of the Gatan 666 parallel recording spectrometer

spectrum to be collected over a wide energy range simultaneously, rather than channel by channel. The spacing between diode elements in the array is 25μm, but the spectrometer dispersion is typically 2μm/eV. The necessary magnification between the spectrometer and scintillator is achieved using four quadrupole lenses, and can range from 0.05 to 2eV/channel, defining the energy range studied. A voltage may also be applied to the electrically isolated drift tube to vary the energy offset. The diode array consists of 1024 channels. The normal procedure is to position the zero loss peak at around channel 200, and set the energy of the channel of the zero loss peak with the most counts to 0eV. To record a core-loss edge, a voltage is applied to the drift tube so that the energy-loss range of interest is recorded on the diode array. For example, to record an oxygen K-edge, a voltage would be applied to the drift tube so that the channel on the diode array that had been set to 0eV for the zero loss peak would now

correspond to an energy loss of ~510eV. Since the edge onset for the oxygen K-edge is around 532eV, the edge would be recorded in the middle of the diode array.

2.3 Acquisition and Processing of EELS Data

2.3.1 Specimen Preparation

All samples were prepared by crushing the powders in an agate mortar and pestle, and then dispersing the particles in propan-2-ol. After allowing any larger particles to settle at the bottom, a few drops from near the surface of the suspension were dropped onto a holey carbon film coated copper grid, using a Pasteur pipette, and the solvent was allowed to evaporate.

2.3.2 Acquisition of EELS Data

The alignment of the HB5 to collect EELS data, as shown in figure 2.1, was achieved in the following manner.

The largest VOA was centred on the optic axis of the lower column. This was achieved by wobbling the objective lens current and mechanically moving the VOA until the ADF image became stationary and pulsed in and out of focus. The selected area aperture was then inserted and the condenser astigmatism corrected. The next step was to position the ROA on the optic axis by accurately wobble centring it, using an ADF image at a magnification of at least x 100 000. The condenser lens was also aligned if necessary but this was generally not required. The microscope was then set to the

rocking beam diffraction mode. The position of the ROA was then marked by centring the locate on the image of the ROA. The next step was to remove the ROA and use the Grigson coils to centre the beam on the spectrometer axis. The collector aperture was then inserted and mechanically aligned to the spectrometer axis. Finally the post-specimen lenses were mechanically aligned to this axis.

The collection angle was defined by a 1mm-diameter collector aperture preceding the STEM detectors. A 1.25mm diameter spray aperture was fitted after the STEM detectors to remove stray scattering from the edge of the collector aperture. This set-up gave a probe with a diameter of 1nm containing ≈0.2nA, a probe half-angle of 11mrad and a collection half-angle of 12mrad.

The response of the photodiode array used to collect the data is non-linear above 10 000 counts per acquisition, and saturates at 16 000 counts per acquisition. Therefore integration times had to be chosen which gave less than 10 000 counts per acquisition. The only time this had to be considered was during the collection of the low-loss spectra, since the count rates for the core-loss edges were always less than this cut-off. To collect the low-loss region, 100 read-outs, each of 0.04s acquisition time were always recorded. The number of counts per channel in the zero loss peak were kept to less than 10 000 per acquisition using either the attenuator or beam-blanking system. The beam-blanking system was preferred since the amount of blanking could be altered, depending on the thickness of the particle, to maximise the count rate.

All spectra were recorded by scanning a raster over an area of specimen of approximately 100Å^2, and at an energy dispersion of 0.1eV/channel. The dispersion of the spectrometer was calibrated by applying known voltages to the flight tube of the

spectrometer and observing the displacement of the spectrum. This was done under computer control using the voltage scan module (VSM) of the spectrometer (Krivanek *et al.* 1987). A 100μm VOA was used. This set-up resulted in an energy resolution, defined as the full-width half maximum (FWHM) of the zero-loss peak, recorded through a hole in the carbon film, of between 0.5 and 0.6eV.

All spectra, except for edges at energy losses greater than 1keV, were recorded using the above set-up, and in the following manner. Each core loss edge spectrum was recorded during a single integration of 8 seconds duration. The low-loss spectra were recorded as a sum of 100 acquisitions, each of 40ms seconds duration, during which the beam was unblanked for ~1ms. The normal procedure for each particle was to record a low-loss spectrum followed by an oxygen K-edge and then the one or two metal $L_{2,3}$ edges, as appropriate. The same sequence of spectra was recorded a further seven times, with each set at a different position on the diode array. The position on the array was altered by changing the voltage applied to the drift tube. For example, seven oxygen K-edge spectra were recorded using voltage scan module (VSM) values ranging from 530-536eV, in consecutive 1eV steps. This procedure was followed in order that the channel to channel gain variations on the photodiode array could be removed during the data processing. The series of spectra also verified that there were no changes in edge shape due to beam damage. The dark currents for each acquisition set-up were also recorded for each particle.

To obtain a sufficiently high signal to noise ratio to record core-loss edges at energies greater than 1keV, a 250μm VOA had to be used, at a dispersion of 0.5eV/channel. The remainder of the set-up initially remained as described above. However, an acquisition time of around 16 seconds was required to collect edges of adequate quality using this

set-up. This acquisition time was sufficiently long for the sample to drift, which meant that two consecutive edges could not be recorded which were identical. This raised problems with the processing, since a core-loss spectrum and low-loss spectrum could not be collected from a particle without possible changes in the thickness of the particle occurring during the acquisitions. This meant that the deconvolution stage in the processing, described in section 2.3.3, was not accurate since the thickness of the particle was different when the low-loss and core-loss spectra were recorded. To reduce the acquisition time the collector aperture was removed, and the 2mm ADF used. This reduced the acquisition time to 6 seconds per acquisition, which was short enough to collect a low-loss and two core-loss spectra consecutively without drift occurring. These changes in the experimental set-up for high-energy edges, resulted in a degradation of the energy resolution, defined as previously, to 1eV/channel.

2.3.3 Processing of EELS Data

For each core-loss edge of interest in each particle studied, the low loss region, core loss edges at a number of energy offsets, and the dark current for each acquisition set-up were recorded. In this section examples are given of various parts of the processing routine. The spectrum used in all examples is the oxygen K-edge from a magnesium aluminate sample.

All data was processed using the Gatan EL/P Version 3.0 software. The first step in the data processing routine is the removal of the "dark current" from each spectrum. This is the detector background signal due to offsets in the detector and thermal leakage from the diode capacitors. The dark current is dependent on the acquisition set-up and is obtained by recording a spectrum for each acquisition set-up when the tip is switched

off. The energy scales are then calibrated for the spectra that have had the dark current removed. The most intense channel in the low-loss spectrum is set to 0eV. For each of the core-loss spectra, the energy scale was calibrated by setting the channel that corresponded to 0eV in the low-loss spectrum to the VSM energy offset value at which the core-loss spectrum was recorded. To remove the fixed "pattern noise" due to small channel-to-channel gain variations present in the array, a number of spectra collected at slightly different energy offsets, as described in section 2.3.2, are aligned and summed.

The core-loss edges are generally superimposed on a background comprised of various contributions from different scattering processes. These include the tails of plasmons and core-edges at lower energies. This background can be modelled using an inverse power-law of the form

$$B_j = AE_j^{-r} \tag{2.2}$$

where B_j is the number of counts in the background at channel j in the background fitting region, E_j is the energy loss at channel j, and A and r are constants. By taking the logarithm of Equation 2.2 a straight line can be fitted to the background and extrapolated into the edge region. Figure 2.3 shows the results of a power-law background subtraction. The blue spectrum is the raw data that has only had the dark current removed. The purple line shows the background model of the form AE^{-r}. The green spectrum shows the edge after the background has been removed. The accuracy of the fit depends on the size and position of the window used to model the background. The best fit was judged to be that which gave a background, after subtraction, comprising of small, random, noise-like intensities about the x-axis in the pre-edge region, as shown in the inset in Figure 2.3, rather than large positive or negative intensities. The window chosen in this case ranged from 522-529eV. In the pre-edge

region the intensity oscillates around zero, showing a good background fit has been chosen.

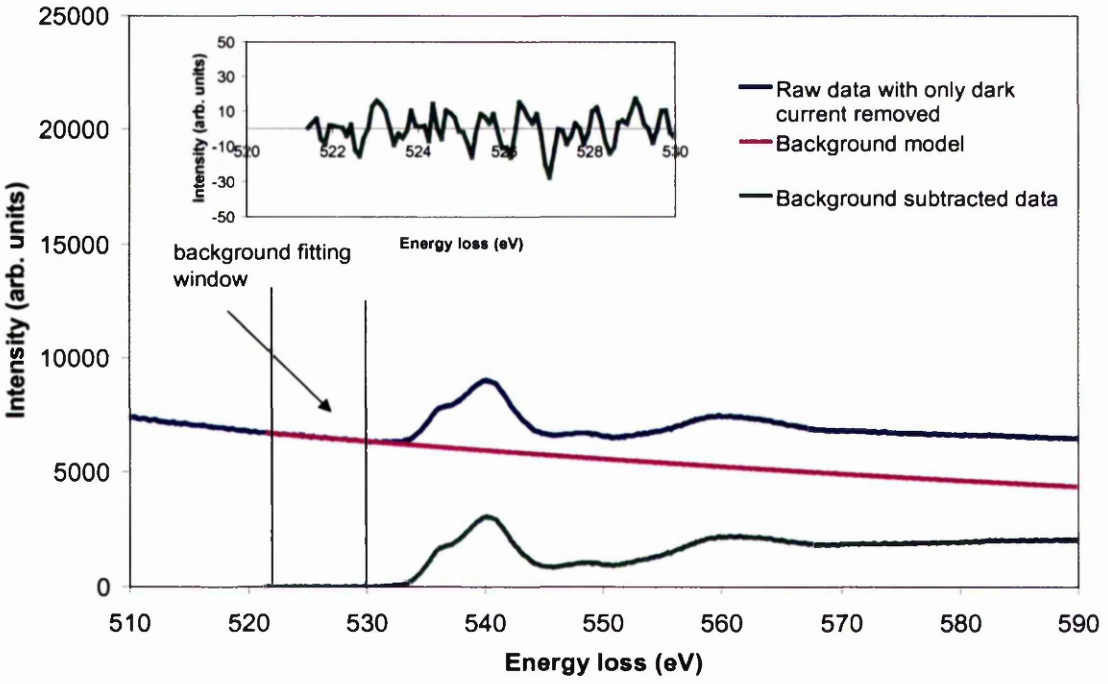

Figure 2.3 Background subtraction using a fit of the form AE^{-r}

The next step in the processing routine is to remove plural scattering contributions from the spectra. This removes the contributions of energy-losses that are due to a combination of the excitation of core and valence electrons. The effect of these interactions is to shift the intensity away from the edge onset to higher energy-losses, according to the probability distribution represented by the shape of the low-loss spectrum. This is equivalent to a convolution operation, and so a deconvolution can be performed, using the low loss spectrum, to remove this effect. The method used was the Fourier-Ratio deconvolution technique. A detailed description of this technique and other deconvolution methods is given by Egerton (1996). Figure 2.4 shows the multiple scattering contributions significantly add to the intensity distribution at the higher energy-losses in the ELNES region for a sample of thickness $t/\lambda = 0.561$.

The thickness, t, is computed from the low-loss spectrum using the formula

$$t = \lambda \ln(\frac{I_t}{I_o}) \tag{2.3}$$

where I_o is the sum of zero-loss peak counts, I_t is the sum of the total spectrum counts, and λ is the inelastic mean free path. Further discussion of this procedure is again given by Egerton (1996). Since the multiple scattering can obscure features in the fine structure for thick specimens, and give misleading intensities, EELS data has only been processed for which $\frac{t}{\lambda} < 1$.

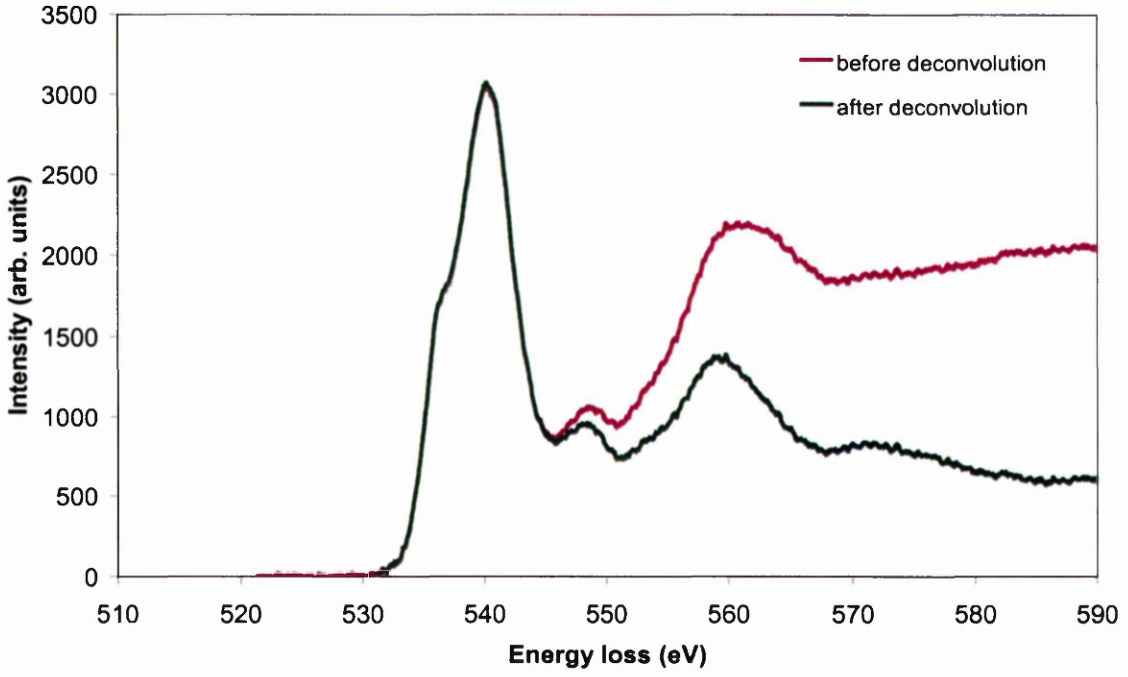

Figure 2.4 *The removal of multiple scattering contributions to the edge using the Fourier deconvolution method. The result is a decrease in intensity away from the edge onset.*

The final step in the data processing routine is to remove the effect of the finite point spread function of the detector. This is done using the "sharpening" function in EL/P. The basic procedure is that a Gaussian function is fitted to the top half of the

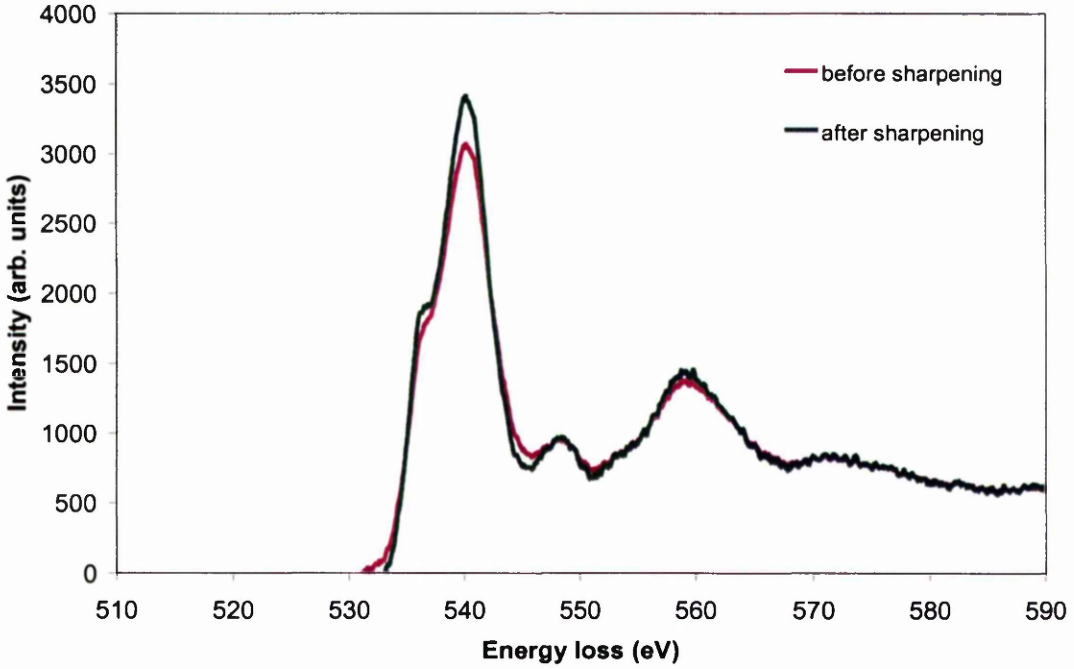

Figure 2.5 *The effect of sharpening to remove the point spread function of the diode array.*

experimental zero loss peak. This is then subtracted from the zero loss peak and the residual is Fourier transformed. The core-loss spectrum Fourier tranform is divided by the zero loss peak residual Fourier transform and the ratio is then inverse Fourier transformed. The effect of this is to remove the effect of the tail of the zero loss peak which can obscure the detail observed in the fine structure. An example is shown in figure 2.5. It can be seen that the shoulder on the left-hand side of the first peak is more pronounced after sharpening.

Chapter 3

Near-edge Structure Modelling Techniques

3.1 Introduction

Electronic structure calculations can be classified into three main types, namely molecular orbital, multiple scattering and band structure calculations. Each of these will be described in turn, their relative merits assessed, and examples of their applicability referred to. A more detailed description of multiple scattering calculations, and in particular the multiple scattering code FEFF, which has been used for all simulations, will then be given.

3.2 Molecular Orbital Theory

The simplest and most easily interpreted approach to modelling fine structure is molecular orbital theory (Glen and Dodd, 1968). The basic idea is that the core electron is excited from its initial state into an unoccupied molecular orbital. The

molecular orbitals are formed by the interaction of the atomic orbitals of the excited atom with those of the neighbouring atoms. The near-edge structure is assigned to transitions between an occupied core state and unoccupied molecular orbitals. The X_α method (Slater and Johnson, 1972) is one of the most powerful and popular methods used to calculate the energy levels in this way. This approach has been used to aid the interpretation of fine structure data from a variety of solids, including titanium oxides, carbides and nitrides (Fischer, 1970 and 1972). This method, combined with multiple scattering calculations, which will be described in section 3.4, has also been used to interpret the fine structure of neosilicates with a reasonable degree of success, (McComb *et al.*, 1991; McComb *et al.*, 1992; Hansen *et al.*, 1994).

A disadvantage of this method is that it is difficult to incorporate the effect of more distant neighbouring atoms, whose presence can have a considerable effect on the near-edge structure. The molecular orbital approach has been used to account for gross features in near-edge structure, and can be interpreted relatively easily, but this simple method cannot explain more subtle fine structure features.

3.3 Band Structure Calculations

The most rigorous approach to obtaining the fine structure for crystalline materials is from band structure calculations. These calculations have greatly improved due to the introduction of density functional theory (DFT). The fundamental idea behind this theory will be considered in this section.

The total energy of a system of interacting ions and electrons can be written as

$$E_{total} = E_{e-e} + E_{e-ion} + E_{ion-ion} \tag{3.1}$$

where the first term in equation 3.1 describes the kinetic energy of the electrons and the potential energy of their interaction with each other. The second and third terms describe the potential energy of the interaction between the electrons and ions, and between the ions themselves, respectively.

The basis of density functional theory is the Hohenberg-Kohn theorem (Hohenberg and Hohn, 1964) which states that the first term, E_{e-e}, can be expressed as a functional of the ground-state electronic density, and that the second term, E_{e-ion}, can also be written in terms of the electronic density. The ion-ion term can be calculated from classical electrostatics for point charges, so the total energy of the interacting system can be written as a functional of the electron density. This expression for the total energy with respect to the electron density can be minimised to find the ground-state energy and density.

This results in only having to determine the ground-state properties of the electron gas for a structural arrangement of nuclei that act as an external potential on the electrons. Kohn and Sham (Kohn and Sham, 1965) have shown that it is possible to map the many-body problem of an interacting electron gas in the presence of an external potential to an exactly equivalent set of self-consistent single-electron equations. The function is then written in terms of a set of single-particle electronic states $\{\Psi_i\}$. Minimising the Kohn-Sham energy functional with respect to the set of wave functions $\{\Psi_i\}$ yields the Kohn-Sham equations which must be solved self-consistently. When these equations are solved such that the occupied states generate the same electron density used to construct the potential, then the ground-state density and energy have been found.

The Kohn-Sham equations include a term related to the exchange-correlation functional. Since it is extremely difficult to calculate this for a complex system the local density approximation (LDA) is used. This approximation assumes that the exchange-correlation energy per electron at a certain point in the electron gas is the same as it would be at the same point in a homogeneous electron gas of the same density. This is difficult to justify since the electron density is usually varying rapidly in systems of interest. However, the justification for it mainly comes from its success in predicting physical properties.

Since DFT is very successful at obtaining the total energy of the system it is particularly useful for calculation of physical properties such as bulk moduli. Although the eigenvalues of the equations solved in this technique are not physical eigenvalues the method still generates wavefunctions that can be successfully used to model fine structure as discussed below. There are a variety of techniques that can be used to solve for the ground-state properties of the electron gas. Some of these methods will be discussed below.

The starting point in calculating probability of the excitation of a core electron into the conduction band in band structure calculations is Fermi's golden rule, which gives an expression for the double differential cross-section for scattering, $\frac{d^2I}{d\Omega dE}$, with momentum transfer, ***q***, as

$$\frac{d^2I}{d\Omega dE} = \frac{2\pi}{\hbar}\rho(E)\left(\frac{e^2}{\varepsilon_o}\right)^2\left|\frac{< f|\exp(iq.r)|i >}{q^2}\right|^2 \qquad (3.2)$$

where $|i\rangle$ represents the inner shell electron wavefunction

$|f\rangle$ represents the final unoccupied state

and $\rho(E)$ is the density of states for final state electrons with energy E.

As discussed in section 1.4.2, the operator in equation 3.2 can be expanded and, within the dipole approximation, the only term that does not approximate to zero and has to be considered is

$$\frac{d^2I}{d\Omega dE} = \frac{2\pi}{\hbar}\rho(E)\left(\frac{e^2}{\varepsilon_o}\right)^2\left|\frac{q.<f|r|i>}{q^2}\right|^2 \tag{3.3}$$

As a consequence of the dipole selection rule, described in section 1.4.2, equation 3.2 can be simplified to

$$\frac{d^2I}{d\Omega dE} = \frac{2\pi e^2}{\hbar\varepsilon_o q^2}\left[|m_{L+1}|^2\rho_{L+1}(E) + |m_{L-1}|^2\rho_{L-1}(E)\right] \tag{3.4}$$

where the matrix element is defined as

$$m_{L\pm1} = \langle f_{L\pm1}|r|i_L\rangle \tag{3.5}$$

since the matrix element is assumed to vary slowly in the region 10 to 20eV above the threshold. As discussed in section 1.4.2, the fine structure can then be directly related to the site and symmetry-projected density of unoccupied states.

The initial wavefunction $|i\rangle$ is a well-defined atomic wavefunction and can be calculated from appropriate Hartree-Fock atomic theory. The calculation method therefore depends on how the unoccupied final state wavefunction is calculated. There are many one-electron band theory techniques, which are based on self-consistently calculating occupied and unoccupied states.

The atomic orbitals modelled need to represent the oscillatory behaviour of the crystal orbitals in the core regions. One class of band structure calculations uses linear muffin-

tin orbital (LMTO) basis functions to represent the crystal orbitals (Andersen, 1975 and Skriver, 1984). This method assumes the muffin-tin approximation, in which the crystal is divided into the largest possible non-overlapping spheres about each nucleus. The potentials inside the spheres are assumed to be spherically symmetric, and the potential outside the spheres assumed to be constant. Other techniques invoking the muffin-tin approximation include the augmented plane wave (APW), (Andersen, 1975), and augmented spherical wave (ASW), (Williams and Kubler, 1979) methods. Both use products of radial wave functions and spherical harmonics inside the muffin tins, but expand the wavefunction in the space between the muffin tins as plane waves and spherical waves respectively. These methods are well suited to many materials including oxides and transition elements, and have been successfully applied to transition metals and their carbides, nitrides and oxides (for example, Grioni *et al.,* 1989, Lie *et al*, 1998, Hébert-Souche *et al.,* 2000). However they work best for simple structures, and are not good for interfaces, which require large supercells.

Pseudopotential methods (for example, Pickett, 1989 and references therein) are based on the idea that the wavefunctions of the core states are independent of the environment of the atom, and are therefore the same in a free atom and crystal. This means that the interactions of the frozen core states, band states and nuclear potential, with the external ionic potential, can be considered separately and combined. It generally involves the use of a linear combination of plane waves and an appropriate mixture of atomic wavefunctions from the occupied states of the ion core. This technique works well for semiconductors and light elements (Weng *et al.,* 1989), and can handle large supercells.

A further type of band structure calculation is similar to the real-space multiple scattering method, discussed in section 3.4, but is carried out in reciprocal space. These

Korringa-Kohn-Rostoker (KKR) calculations (Korringa, 1947 and Kohn and Rostoker, 1954) consider an infinite system, and a Bloch condition is imposed on the wavefunction, whereas multiple scattering calculations use a small cluster, of normally less than one hundred atoms, around the excited atom.

Band structure calculations often model the intermediate ELNES region well, but are not so accurate near the threshold region due to the effect of the core hole on the energy level distribution, or at greater than 5-10eV beyond the edge threshold, where the calculations may not converge. However, a variety of approximations have been developed to include the many-body effects which influence the fine structure at the edge onset.

As a result of the dipole selection rule, and the core wavefunction being localised at a particular atomic site, the band structure calculations must produce site and symmetry projected densities of states in order to model the ELNES. This is not readily available from some band structure methods, and even when available, many published results only quote the complete band structure, and not the components of interest.

A disadvantage of this method is the considerable computing power required. The resources necessary increase further when it is desirable to incorporate imperfections in the compounds, such as a defect, and an infinite perfect crystal lattice cannot be assumed. This type of calculation requires the use of a supercell, which includes the imperfection and is used as the unit cell for the compound. These calculations require considerable computational resources even for calculations on simple compounds and the use of supercells increases the computational effort required even further.

3.4 Multiple Scattering Calculations

3.4.1 General Principles

The third approach to modelling fine structure, multiple scattering calculations, can incorporate deviations from the perfect crystal structure found in many real materials. Multiple scattering calculations are based on the concept that the excited core electron wave can be scattered by the neighbours of the excited atom. The interaction of the scattered wave with the original outgoing electron wave, at the site of the excited atom, creates an interference pattern that results in the near-edge structure. Electrons having energies up to ~30eV above the threshold, *i.e.* in the ELNES region, undergo plural scattering whereas electrons with energies corresponding to the EXELFS region mainly undergo single scattering, as shown in figure 3.1. Multiple scattering is important in the near-edge region because the ejected electron has a longer inelastic mean free path at low kinetic energies, and backscattering therefore occurs in a larger volume of the specimen, as shown in figure 3.2 (Seah and Dench, 1979).

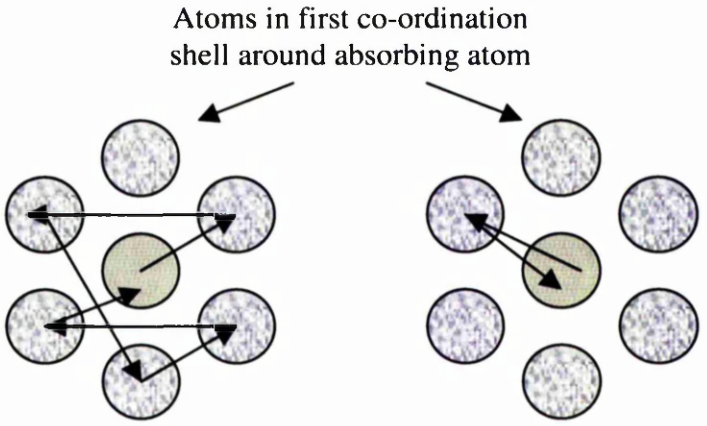

Figure 3.1 *In the ELNES region multiple scattering events are important, whereas in the EXELFS region single scattering is dominant.*

The effect of neighbouring atoms on the near-edge structure depends on their scattering potentials, and the resultant change in phase of the electron wave. The atoms surrounding the excited atom can be divided into shells, according to their distance from the central excited atom, and all inter and intra-shell scattering paths can be calculated and given a relative amplitude. The number of neighbouring atoms from which the excited electron can scatter, and the number of scattering events, can be progressively increased, so the importance of certain scatterers and scattering paths can be identified.

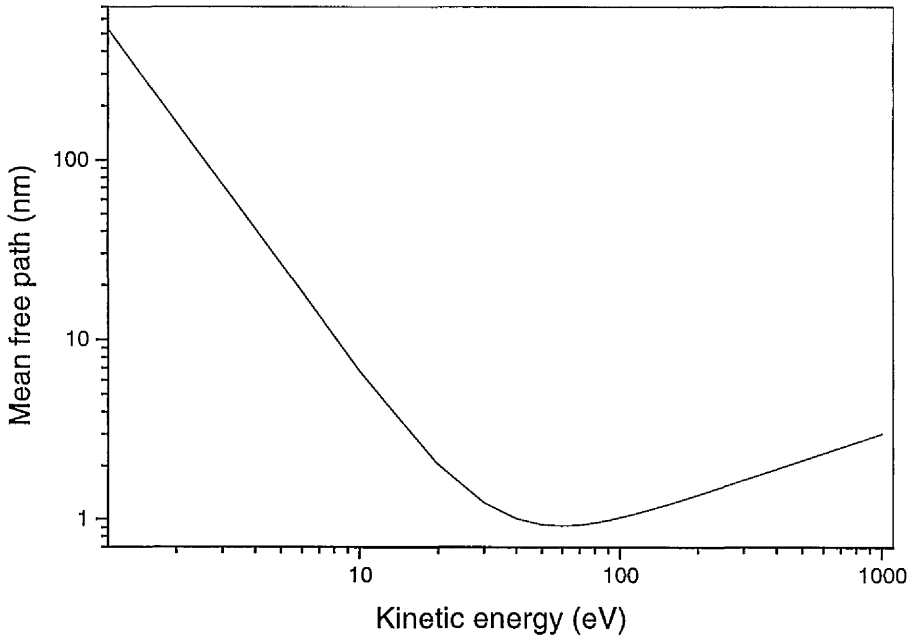

Figure 3.2 *The ineleastic mean free path of an electron, as a function of its energy above the Fermi level.*

3.4.2 Multiple Scattering Theory

Multiple scattering theory employs a one-electron approximation to describe the excitation processes. The spatial and energy dependence of the DOS can be expressed

in terms of the imaginary part of the one-electron Green's function operator, $G=[H-E]^{-1}$ where E is the electron energy and H is the effective one-electron Hamiltonian. In this section the key points of the calculation will be introduced. A detailed description can be found in a number of books on the subject (for example, Heine, 1980 and Durham, 1988).

The starting point to explain the theory of multiple scattering is again Fermi's golden rule:

$$\frac{d^2I}{d\Omega dE}=\frac{2\pi}{\hbar}\rho(E)\left(\frac{e^2}{\varepsilon_o}\right)^2\left|\frac{<f|\exp(iq.r)|i>}{q^2}\right|^2 \tag{3.2}$$

However, instead of calculating the final states as in band structure calculations, it is equivalent and much faster to re-express equation 3.4 in terms of the electron Green's function, which can be solved for directly. The Green's function describes the propagation of the electron wave from a point, *r*, to a point, *r'*. Formally it is defined as

$$G(r,r',E)=\sum_n\frac{\Psi_n(r)\Psi_n^*(r')}{E+i0-E_n} \tag{3.6}$$

where *i0* is a positive, infinitesimal quantity to prevent equation 3.6 being undefined when $E=E_n$. It is related to the density of states, *n(E,r)*, by

$$n(E,r)=-\frac{1}{\pi}\mathrm{Im}\,G(r,r',E) \tag{3.7}$$

A more detailed discussion of the origin of the definition of the Green's function in equation 3.6, and the Green's function's relation to the density of states, stated in equation 3.7, is given in Appendix 1.

The Green's function can be expressed as a sum over all multiple scattering paths, Γ, that the electron can take away from the absorbing atom and back. This leads to the relation, in matrix notation, for the fine structure, χ, (Rehr, 1993),

$$\chi = \sum_{\Gamma} \mathrm{Im} < e^{2i\delta_1} \sum_{m} < 1m | \boldsymbol{G}\boldsymbol{t}_N \ldots \boldsymbol{G}\boldsymbol{t}_2 \boldsymbol{G}\boldsymbol{t}_1 \boldsymbol{G} | 1m >> \qquad (3.8)$$

where t_i is the scattering matrix for site i and describes the diffusion of an electron by an atom at that site

δ_l is the $l=1$ partial-wave phase shift at the absorbing atom

and the outer brackets indicate a thermal and configurational average.

Real space multiple scattering calculations of this type, which are based on a multiple scattering Green's function formalism, are equivalent to Koringa-Kohn-Rostoker (KKR) band structure calculations, provided the multiple scattering expansion converges.

3.4.3 Main Steps of Multiple Scattering Calculations

3.4.3.1 Construction of Potentials

The first step in all multiple scattering calculations is to construct the scattering potentials of the atoms in the cluster considered. The "muffin-tin" approximation, described in section 3.3, is normally employed because it retains a spherical symmetry around each atom, ensuring that the elements of the scattering matrix keep a simple form.

There are two common ways to calculate the scattering potentials. The first is the Mattheiss prescription (Mattheiss, 1964). The main steps to this procedure are:

1. Obtain the charge densities for the neutral atoms from a self-consistent field atomic calculation, often by way of the Hartree-Fock-Slater description.
2. Place these atomic charge densities on each site of the chosen geometry and spherically average the superposed charge densities about the atom whose potential is required.
3. Taking this spherical, superposed charge density, the Poisson equation is solved for the Coulomb part of the potential and the exchange correlation potential is found using a local approximation of the X_α type.

The normal use of the Mattheiss prescription is to assume that the actual charge densities will be close to the result generated by the superposition of the atomic charge densities and not repeat the calculation. It is therefore used as an approximation to the alternative self-consistent calculations. The self-consistent method gives a better estimate of the charge densities. To calculate the potential self-consistently the same prescription can be used as above. After construction of the potentials, new wavefunctions which include modifications due to the presence of the neighbouring atoms can be found for each type of atomic site, and new charge densities, which now include charge transfer, can be calculated and put into step 1 of the above prescription. This procedure is repeated until the calculation converges.

From the output of the Mattheiss prescription or a self-consistent calculation, the phase shifts can be generated, and then the t-matrices, which are the components of the multiple scattering calculations, can be found.

3.4.3.2 Core hole effects

When an electron is excited from a core level into the conduction band, a core hole is created and the electrons remaining in their ground-states experience an increased effective charge from the nucleus. This results in the relaxation of the remaining core electrons to screen the effective nuclear charge, and this perturbs the unoccupied DOS. There are a number of approaches to including the core hole effect in the calculation. In the calculations presented here the effect of the core hole is created using a modified electronic configuration for the absorbing atom by removing a core electron from the appropriate level, and adding an extra electron to the valence band and allowing the system to fully relax. No change is made to the nuclear configuration for the absorbing atom. Therefore, when simulating the oxygen K-edge, the normal nuclear configuration for an oxygen atom is used, and the electronic configuration becomes $1s^1 2s^2 2p^5$ for the absorbing atom.

3.4.3.3 Path Enumeration

Once the scattering potentials for each type of site have been calculated, the electron scattering paths are enumerated. One approach to defining the paths included in the multiple scattering calculations is to employ multiple scattering path expansions where only important scattering paths, such as single and double scattering paths, are included in the calculation. This type of calculation is suitable for the simulation of EXELFS spectra where the single scattering contribution is dominant. However, in the ELNES region the multiple scattering expansion fails to converge rapidly (Ankudinov *et al.*, 1998). In order to achieve convergence in the ELNES region a full multiple scattering calculation is required, where multiple scattering paths to infinite order are included.

The full multiple scattering calculation requires the inversion of the matrix *[1+TG]*, where *T* is the matrix defining the scattering properties of the surrounding atoms and G is the Green's function describing the propagation of the electron wave. This is a very difficult task because the size of the matrix grows very rapidly as the number of atoms in the calculation increases. The computational effort required for such a calculation is a severe limitation of the full multiple scattering method and restricts the cluster sizes that can be used. The other disadvantage of this method is that it is a global approach and no insight can be gained into the individual role of each scatterer or scattering path. However, once the convergence of the calculation has been confirmed using the full multiple scattering approach, calculations using only low order scattering events such as single and double scattering paths can be used to obtain a more detailed understanding of the importance of certain scatterers and scattering paths.

3.4.3.4 Broadening

The final step in the simulation of the fine structure is the addition of broadening to the theoretical spectrum, to allow fair comparison with the experimental data. Three contributions to the broadening must be considered. Firstly, there is a lifetime broadening contribution arising from the fact that the electron will only remain in the excited state for a finite time, before returning to the ground-state, and emitting an X-ray or Auger electron in the process. The core hole lifetime, τ_h, is determined by the speed of the de-excitation mechanism and is related to the energy broadening, Γ_i, by the Uncertainty Principle as

$$\Gamma_i \tau_h \approx \hbar \tag{3.10}$$

The second contribution is the final state lifetime, which is related to the ineleastic mean free path of the ejected electron. The final state lifetime broadening is proportional to the square of the energy above the threshold, so the fine structure is progressively damped with increasing energy loss. The level of detail, which can be observed in the experimental data, is also limited by the instrumental resolution. This includes factors such as the thermal spread of the electron energies and the spectrometer resolution. It is common practice to convolve the simulated fine structure with a Lorentzian function whose width is dependent on the amount of broadening required.

3.4.4 The FEFF code

3.4.4.1 FEFF version 7

The multiple scattering code, FEFF, version 7, (Zabinsky *et al.*, 1995), was initially used to model the fine structure. There are four main stages to the FEFF calculations:

1. The code first calculates the potential for each free atom type using a relativistic Dirac-Fock-Slater atom code, and then overlaps these using the Mattheiss prescription to construct the muffin-tin potentials, and calculates the scattering phase shifts.

2. The next step is to define all the possible multiple scattering paths, out to a pre-defined limit. This is achieved by starting with the single scattering path from the absorbing atom to its nearest neighbour and back. Two new paths are

generated by replacing the nearest neighbour with the second nearest neighbour in the single scattering event, and by adding an extra scattering event to the initial single scattering path, as shown in figure 3.3. Two new paths are created from each of these paths in turn in a similar manner. In this way all possible scattering paths are identified. The number of paths is limited by restraining the number of scattering events that can occur, and by confining the maximum path length the electron can travel.

3. In the third module the code calculates the effective scattering amplitude and total scattering phase shift using a scattering matrix algorithm. At this point in

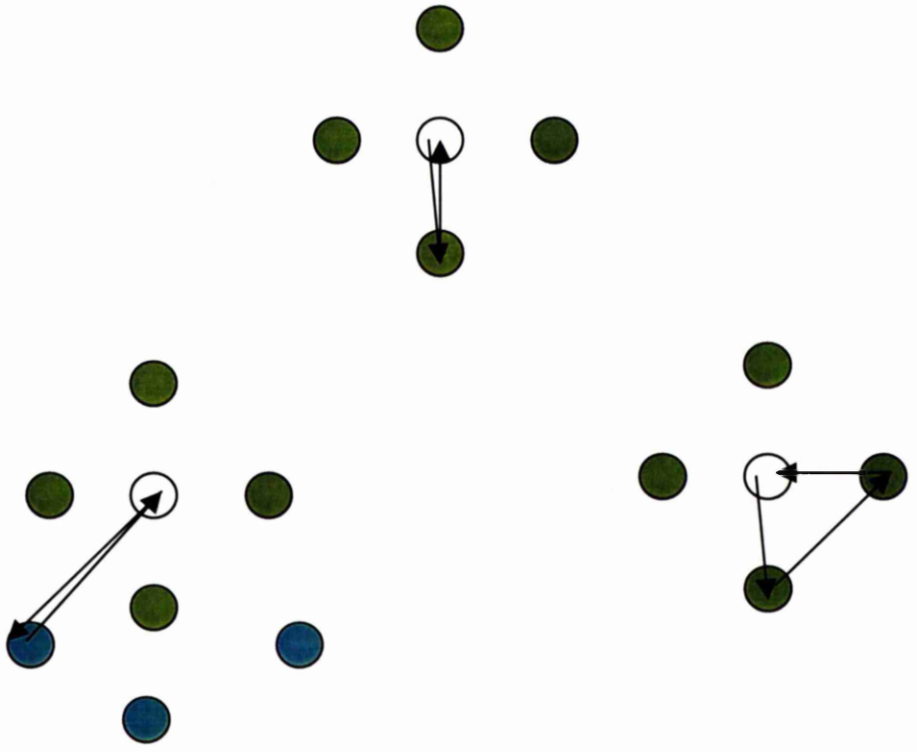

Figure 3.3 *The shortest scattering path is (a) single scattering from the absorbing atom to its nearest neighbour. The second and third shortest scattering paths are created by (b) single scattering from the second nearest neighbour and (c) double scattering from two of the nearest neighbours.*

the calculation equivalent paths are identified and their degeneracies taken into account when determining their overall importance. If desired, filters can then be applied to remove paths of lesser importance, *i.e.* those that do not have a large relative scattering amplitude.

4. The final stage of the calculation is to combine the scattering parameters from the remaining paths to obtain the final spectrum.

The input file for these calculations was generated using the ATOMS, version 2.46b code. This is a program which was written by Bruce Ravel, one of the authors of the FEFF code, which generates a list of co-ordinates of the atoms surrounding the absorbing atom of interest from the compound's crystallographic data. The output from ATOMS is the FEFF input file.

There are a large number of parameters that can be varied in the FEFF calculation, for which default values are provided. Typical choices made by the user include the definition of the number of atoms in the cluster surrounding the central atom, the maximum scattering path length, and the number of times the electron can be scattered by the atoms in the cluster. It is possible to filter out unimportant scattering paths with low relative scattering amplitudes from contributing to the final stages of the calculation. This is valid since many low amplitude paths cancel one another due to random phase incoherence and may be excluded from contributing to the final spectrum since they are negligible. The user again defines the maximum relative scattering amplitude considered to be insignificant.

In the initial calculation the maximum scattering path length was set to 10Å. This value was chosen since it was estimated that all scattering path lengths of any significance would be much smaller than this, so this large value meant that no important paths would be excluded from the calculation. No filters were employed to ensure that no important paths were being discarded at any stage of the calculation. Figure 3.4 shows the effect of progressively including more scattering events and more shells in the calculation. The shells used are defined in table 3.1.

Initially only single, double and triple scattering events, *i.e.* scattering from up to three atoms, were considered for up to a six shell cluster, for the oxygen K edge of magnesium aluminate. This choice was made based on the work done on MgO (for example, Rez, 1991), in which all experimental features had been reproduced in a multiple scattering calculation, and had been interpreted in terms of up to triple scattering, from up to four shells.

No. of shells in cluster	No. of atoms in cluster	Cluster radius (Å)
1	4	1.928
2	16	3.131
3	23	3.558
4	29	4.243
5	44	4.648
6	68	5.108

Table 3.1 *A description of the shells used in the multiple scattering calculations shown in Figure 3.3.*

To test for convergence, the calculations for spinel were repeated for scattering from up to four atoms, which is also shown in figure 3.4. A comparison of up to three and four scattering events simulations show that convergence has not been attained, since new features are present in the latter. For example, a small peak at ~535eV can be observed

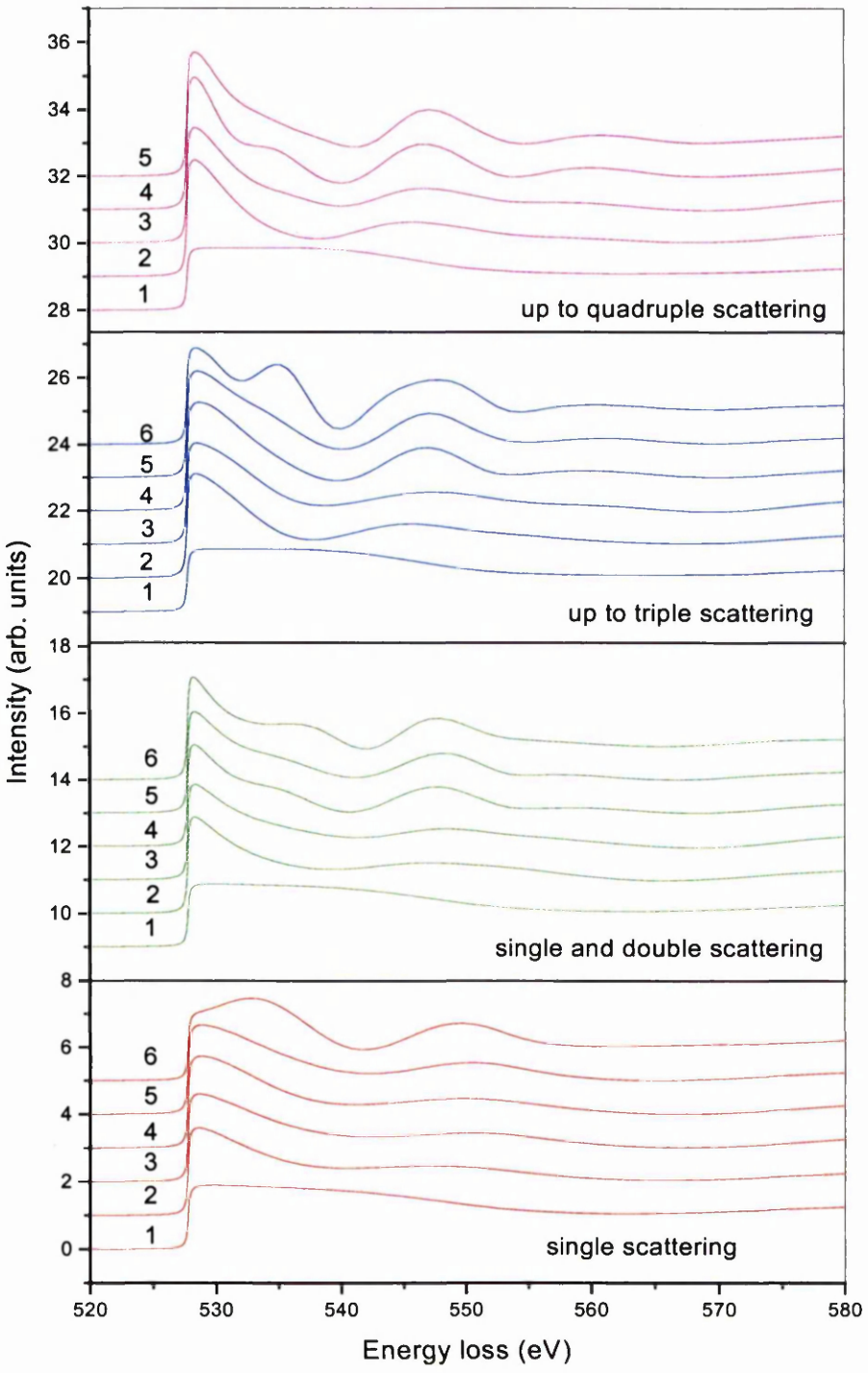

Figure 3.4 *Variation in simulated ELNES spectra as the number of scattering events and cluster size changes. The number at the left hand side of each spectrum is the number of shells in the cluster.*

when up to double scattering from four shells is considered. This feature disappears in the calculation for up to triple scattering from the same number of shells, but reappears when up to four scattering events from four shells is calculated.

By scattering from up to four atoms from five shells the limits of the computational resources available had been reached. The decision not to employ filters, and allow all paths generated to contribute to the final spectrum enormously increased the computational power required. Table 3.2 illustrates how rapidly the number of paths increases as the number of shells and number of scattering events increases. However it was felt that the improper use of path filtering could introduce artifacts into the calculation, which was also not desirable.

Number of scattering events

Number of shells in cluster	**1**	**2**	**3**	**4**
1	2	4	14	35
2	5	31	404	5381
3	8	65	1197	19844
4	10	101	2302	38356
5	13	201	6315	99091
6	16	438	16068	-

Table 3.2 *The number of scattering paths, up to 10Å in length, as a function of the number of shells and scattering events.*

Many published comparisons of multiple scattering calculations and experimental ELNES spectra only employ a low number of scattering events and increase the cluster size until good agreement between the experiment and model is found, but they fail to

comment on convergence. It has already been stated in section 4.4.3 that multiple scattering calculations are the real space equivalent of KKR band structure calculations provided the multiple scattering expansion converges. Convergence is therefore crucial if these calculations are to be used to provide a valid interpretation of fine structure data.

3.4.4.2 FEFF, version 8

The authors of the FEFF code, who believe that a multiple scattering expansion does not converge, and is not reliable in the ELNES region, have addressed this problem. They have released an upgraded program, FEFF, version 8, which can include full multiple scattering by a matrix inversion. The main stages of the calculation are as described in Section 3.4.1 for FEFF 7. However, there are a number of key differences between FEFF 8 and earlier versions of the program.

Firstly, the potential is calculated self-consistently in FEFF 8, which provides a better estimate of the Fermi energy, and allows the evaluation of occupation numbers and charge transfer between atoms. In previous versions the potentials were calculated non-self-consistently, using a superposition of atomic charge densities, which does not properly account for charge transfer in ionic crystals. Accurate estimation of the charge density is particularly important at the edge onset because the electrons have large inelastic mean free paths in this region, as discussed in section 3.4.1. Therefore any errors in the phase shift will quickly accumulate to a large error due to the high number of scattering events in this region. Secondly, it is possible to do full multiple scattering calculations using FEFF8, whereas in previous versions it was only possible to use

higher-order path expansions, and, as discussed above, these do not converge fully in the ELNES region.

For all the multiple scattering simulations presented in the results sections, the potentials have been calculated self-consistently using a cluster of around thirty atoms. Full multiple scattering has been used in all calculations, and the effect of the core hole has been included using the approximation described in Section 3.4.3.2, unless stated otherwise. The use of other optional parameters in the code will be discussed as necessary in the result sections.

Chapter 4

The Syntheses and Characterisation of Spinels

4.1 Introduction

In this chapter the preparative methods and reaction conditions used to synthesise a number of chromite, aluminate and ferrite spinels will be described. It was necessary to synthesise these samples due to the lack of commercial availability of the spinels desired, and the poor purity levels of some of those that were available. The remainder of the chapter will outline the analytical techniques used to characterise and determine the purity of these samples, and the results obtained will be presented. In particular X-ray and neutron diffraction, energy-dispersive X-ray analysis (EDX) and nuclear magnetic resonance spectroscopy (NMR) will be discussed and the results from these various methods compared where appropriate.

4.2 Syntheses of spinels

4.2.1 Preparative methods

The use of a variety of techniques to synthesise spinels has been reported in the literature. Most of these methods are based on the basic ceramic technique, in which the component materials in the solid state are reacted at elevated temperatures to form the desired product. For the syntheses of spinels the general reaction is

$$AO + B_2O_3 \xrightarrow{\text{heat}} AB_2O_4 \qquad (4.1)$$

The general procedure is to grind together stoichiometric amounts of the appropriate metal oxides under acetone in an agate mortar and pestle, and then heat the reaction mixture in a non-reactive container at appropriate temperatures. This approach is the simplest and has been reported to successfully synthesise a variety of spinels including nickel aluminate (Mocala and Navrotsky, 1989; Roelofsen *et al.,* 1992), magnesium aluminate (Wood *et al.,* 1986, Millard *et al.,* 1992), cobalt ferrite (De Guire *et al.,* 1989) and zinc ferrite (O'Neill, 1992).

The disadvantage of the basic ceramic technique is that a product layer is formed where the reactants are in intimate contact, but for further reaction to take place interdiffusion of cations must occur through the product layer, as shown in figure 4.1. These diffusion rates are slow, decreasing further as the thickness of the product layer increases, and are the rate-determining step in reactions of this type. The reaction rate will therefore depend on the particle size, degree of homogeneity in the reaction mixture, and the intimacy of contact between the grains. The mixture must be reground at regular intervals for the reaction to reach completion.

It is possible to decrease the generally very high reaction temperatures required by modification of the basic ceramic technique. A common method is to decrease the particle size in the reaction and increase the intimate contact between the reactants. This can be achieved using a coprecipitation method, in which the metal cations are brought into contact by the decomposition of appropriate hydroxides, carbonates or oxalates, for example. This approach has been successful in a number of syntheses including a variety of chromites (Whipple and Wold, 1961) and zinc ferrite (Kamiyama *et al.,* 1992, Jeyadevan *et al.,* 1994).

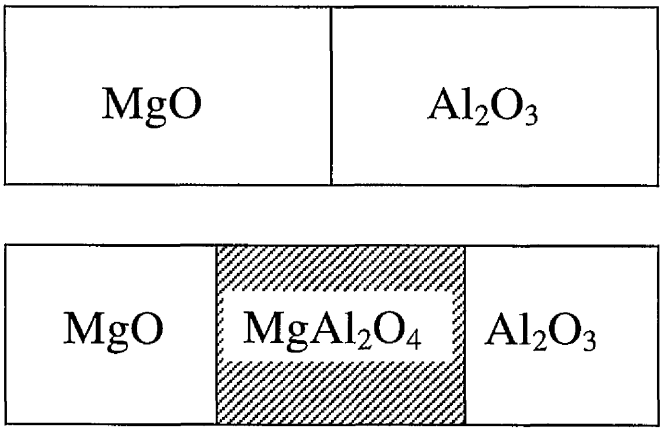

Figure 4.1 In solid state reactions a product layer forms where the reactants are in intimate contact. In the case of magnesium aluminate for example, further reaction requires the counterdiffusion of Mg^{2+} ions to the Al_2O_3 sites, and of the Al^{3+} ions to the MgO sites. The reaction rate becomes progressively slower as the product layer thickens.

A relatively new variation on the ceramic technique is the self-propagating high temperature synthesis (SHS) technique. These highly exothermic reactions normally include the appropriate metal oxides in a precursor form, an oxidiser and a fuel. For example, the synthesis of magnesium chromite has been reported using magnesium nitrate, chromium nitrate and urea (Manoharan, 1992). The nitrates decompose to give intimate mixtures of the metal ions, but the nitrate also acts as an oxidiser, and the urea

is the fuel. The heating of this mixture to about 625K results in spontaneous combustion, and the production of fine crystalline spinel particles.

For the syntheses of spinels in this project, the general approach has been to use the basic ceramic technique in the first instance, since this is the simplest method. It is only when this has been unsuccessful that other methods have been employed.

4.2.2 Syntheses of Chromite Spinels

The chromite spinels were synthesised during a visit to the Solid State Chemistry Group at the University of Aberdeen. These samples were all made using a basic ceramic technique, as described in section 4.2.1. The parent oxides used were Cr_2O_3 (Johnson Matthey), CoO, NiO, CuO and ZnO (all Aldrich) and were at least 99% pure. Cr_2O_3, CoO and ZnO were heated at 600°C, NiO at 300°C, and MgO at 980°C overnight to remove any impurities such as water or carbonates. After these heat treatments the samples were kept in a desiccator to avoid further contamination. Particular care was taken to remove water from MgO since this compound is hygroscopic.

Stoichiometric amounts of the parent oxides required to make 3g of product were ground together in an agate mortar and pestle, under acetone, and pressed into pellets after the acetone had evaporated completely. The pellets were placed in gold- or platinum-lined crucibles and heated as detailed in table 4.1. Each heating period was of 16-18 hours duration. The samples were heated in air, with the exception of copper chromite which was heated in an oxygen environment to prevent reduction of the Cu(II) ion. After each heating period the samples were reground and their phase purity

investigated using X-ray diffraction, which will be discussed in section 4.3. This procedure was repeated until the samples were determined to be single-phase spinel.

4.2.3 Syntheses of aluminate spinels

The parent oxides used to synthesise the aluminate spinels were Al_2O_3 (Fischer) that was 99% pure, and the other relevant metal oxides described in the syntheses of the chromite in section 4.2.2. With the exception of zinc aluminate, the aluminate spinels were synthesised in the University of Glasgow in an identical manner to the chromites. Since Al_2O_3 is a refractory material, higher temperatures were required to initiate the reaction than for the chromites. These reaction conditions are also listed in table 4.1. The samples were heated in palladium-lined crucibles because platinum and gold melt at these higher temperatures.

The zinc aluminate sample was synthesised using the method described by O'Neill and Dollase (1994), in which excess zinc oxide is used in the reaction. This excess is then removed when the product has formed by washing the zinc aluminate and zinc oxide mixture in dilute nitric acid. The zinc oxide reacts with nitric acid to form zinc nitrate that is soluble and can be filtered off.

4.2.4 Syntheses of ferrite spinels

Cobalt ferrite, nickel ferrite and zinc ferrite were synthesised in the Univeristy of Glasgow using a basic ceramic technique. The parent oxides were Fe_2O_3 (Alfa), which was 99% pure, and the other appropriate oxides listed previously in the syntheses of the chromites. The reaction conditions are listed in table 4.1.

O'Neill *et al* (1992), have discussed the difficulty in controlling the stoichiometry of magnesium ferrite when it is synthesised at low temperatures. To avoid these problems the flux decomposition method suggested in their paper was attempted. However, this was unsuccessful which may be due to the fact that an alumina rather than platinum crucible was used, since platinum was unavailable. Therefore some of this material was obtained from Dr. I. Parkin and co-workers of University College London, who has developed the syntheses of ferrites using the self-propagating high temperature technique (Kuznetsov *et al*, 1998, Parkin *et al*, 1999).

Compound	**Number of heating periods**	**Reaction temperature (°C)**	**Atmosphere**
$MgAl_2O_4$	3	1300	Air
$NiAl_2O_4$	5	1300	Air
$ZnAl_2O_4$	3	1300	Air
$MgCr_2O_4$	2	1250	Air
$CoCr_2O_4$	2	1250	Air
$NiCr_2O_4$	4	1250	Air
$CuCr_2O_4$	2	950	Oxygen
$ZnCr_2O_4$	2	950	Air
$CoFe_2O_4$	4	1100	Air
$NiFe_2O_4$	4	1100	Air
$ZnFe_2O_4$	4	1100	Air

Table 4.1 *Reactions conditions for the spinels synthesised using a basic ceramic method. The magnesium ferrite sample was made using the self-propagating high temperature technique.*

4.3 Diffraction techniques

X-ray diffraction is a quick and easy method to confirm the identity of reaction products, and to find and identify any major impurities present. As well as identifying phases and impurities present in the sample, diffraction data can be used to obtain crystallographic information, such as lattice parameters, and in the case of spinels, the oxygen parameter and degree of inversion, using the Rietveld refinement technique. This type of information is essential for accurate interpretation of the EELS data, and for proper representation of the spinels in the simulations.

Unfortunately, this method of analysing X-ray diffraction data is not suitable for obtaining crystallographic information for all the spinels synthesised. This is because the X-ray scattering length depends on the atomic number, so the difference in scattering between, for example, cobalt and chromium, is too small to be meaningfully analysed. However, unlike the X-ray scattering factor, the neutron scattering length does not vary monotonically with atomic number. All the metals involved have sufficiently different scattering lengths that neutron diffraction data can be used to determine the occupancies of each type of site.

This section will begin with an introduction to the general principles of diffraction. The X-ray and neutron diffraction experiments will then be described in more detail. In the final part of this section the Rietveld refinement of the diffraction data will be discussed and the results obtained presented.

4.3.1 Diffraction of X-rays and neutrons by crystals

In this section the diffraction of X-rays by crystals will be considered. The same treatment can be applied to other forms of radiations, such as neutrons and electrons. When a crystal is irradiated by a beam of near monochromatic X-rays, at a general angle of incidence θ, a small fraction of the beam will be scattered in a variety of directions due to the interactions of the X-rays with the electrons of the atoms or ions in the crystal. Figure 4.2 shows the diffraction of X-rays by two consecutive lattice planes. The diffracted waves will generally be out of phase with each other, resulting in destructive interference, and no diffracted beam will be detected.

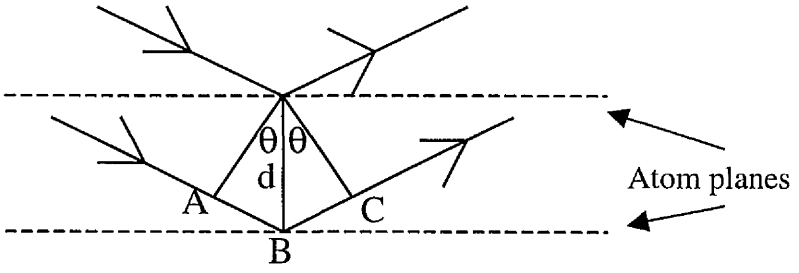

Figure 4.2 *The extra distance, AB+BC, travelled by the second wave must equal a whole number of wavelengths for constructive interference to occur.*

For the beams to interfere constructively after diffraction, the extra distance travelled by the second beam must equal a whole number of wavelengths, $n\lambda$, so the two waves remain in phase. The distance AB travelled by the second beam is equal to $d\sin\theta$, where d is the spacing between the planes and θ is the angle of incidence. The total extra distance travelled by the second wave, $AB+BC$, is therefore $2d\sin\theta$. For many angles of incidence the extra path length does not equal an integer number of wavelengths and destructive interference occurs. However, there is constructive interference at angles for which

$$n\lambda = 2d\sin\theta \tag{4.2}$$

This condition is known as Bragg's Law. This simple approach by Bragg can be used to explain the general idea of X-ray diffraction. A mathematically rigorous treatment of diffraction by Laue, (McKie and McKie, 1974) provides the same result.

The number, positions and intensity of the diffracted beams are fundamentally determined by the crystal structure of the specimen, as shown by the Bragg equation. The intensity, however, can be affected by the nature and wavelength of radiation used. When a powder sample is irradiated by a beam of intensity I_p, the intensity I, of the beam reflected by plane (hkl) is given by (Langford and Louer, 1996);

$$I = I_p K\lambda^3 V^{-2} m_{hkl} PLF_{hkl}^2 v \tag{4.3}$$

where K depends on whether X-rays or neutrons are used

V is the volume of the unit cell

m_{hkl} is the multiplicity of the reflection by planes <hkl>

P is the polarisation factor

L is the Lorentz factor

F_{hkl} is the structure factor, taking into account thermal effects

v is the effective diffracting volume of the sample, including the effects of absorption

4.3.2 Acquisition of X-ray Data

The discussion so far has only considered diffraction by a single crystal. In the powder diffraction method the sample is ground to a fine powder, which means that the particles in the powder are randomly oriented with respect to the beam. The advantage

of this method is that since the orientation is random, for every set of lattice planes, some of the particles will be oriented at the Bragg angle.

The powder samples were prepared by grinding the specimen with acetone in an agate mortar and pestle to form a slurry. This mixture was dispersed on a glass slide. The acetone was allowed to evaporate leaving a flat layer of fine powder with randomly oriented crystals.

All of the X-ray data were collected using cobalt K_α radiation (λ=1.78897Å) on a Phillips PW 1050/35 X-ray diffractometer, with a vertical goniometer and iron filter. The diffraction patterns were collected from 4 to 80° 2θ using 0.02° increments of the detector, at a rate of 2° per minute. Figures 4.3 - 4.5 show the X-ray diffractograms recorded for all the samples synthesised. The identities of the compounds were confirmed by comparing the positions and intensities of the diffracted beams with those in the data bank maintained by the Joint Committee on Powder Diffraction Standards (JCPDS). The appropriate JCPDS number is listed next to each compound in the figures.

Figure 4.3 shows the XRD patterns from the aluminates. For all of these samples low intensity extra peaks, which have been marked with asterisks, are present. The nickel aluminate sample was heated five times, in case these peaks were due to the presence of unreacted material, but these heat treatments had no effect on the number or intensities of these peaks. The XRD pattern was also obtained from a greater than 99% pure magnesium aluminate sample that had been purchased from Alfa Aesar. The same impurity peaks were also present in this spectrum. All attempts to identify the origin of these peaks using the JCPDS files were unsuccessful, so batches of each sample were

sent to the University of Aberdeen for analysis. The peaks were also present on the diffractograms obtained from the Phillips diffractometer in Aberdeen, but were not present when the spectra were recorded on their Stoe Stadi/P diffractometer, suggesting their origin was an instrumental effect. Further evidence for this was provided by a thorough analysis of the commercial magnesium aluminate sample by electron probe microanalysis (EPMA) in Aberdeen, and by energy-dispersive X-ray analysis (EDX) in Glasgow, which will be discussed in section 4.4. No impurities were found by either method, and EPMA confirmed the sample was stoichiometric magnesium aluminate. Therefore it was assumed that the aluminate samples were single phase spinel.

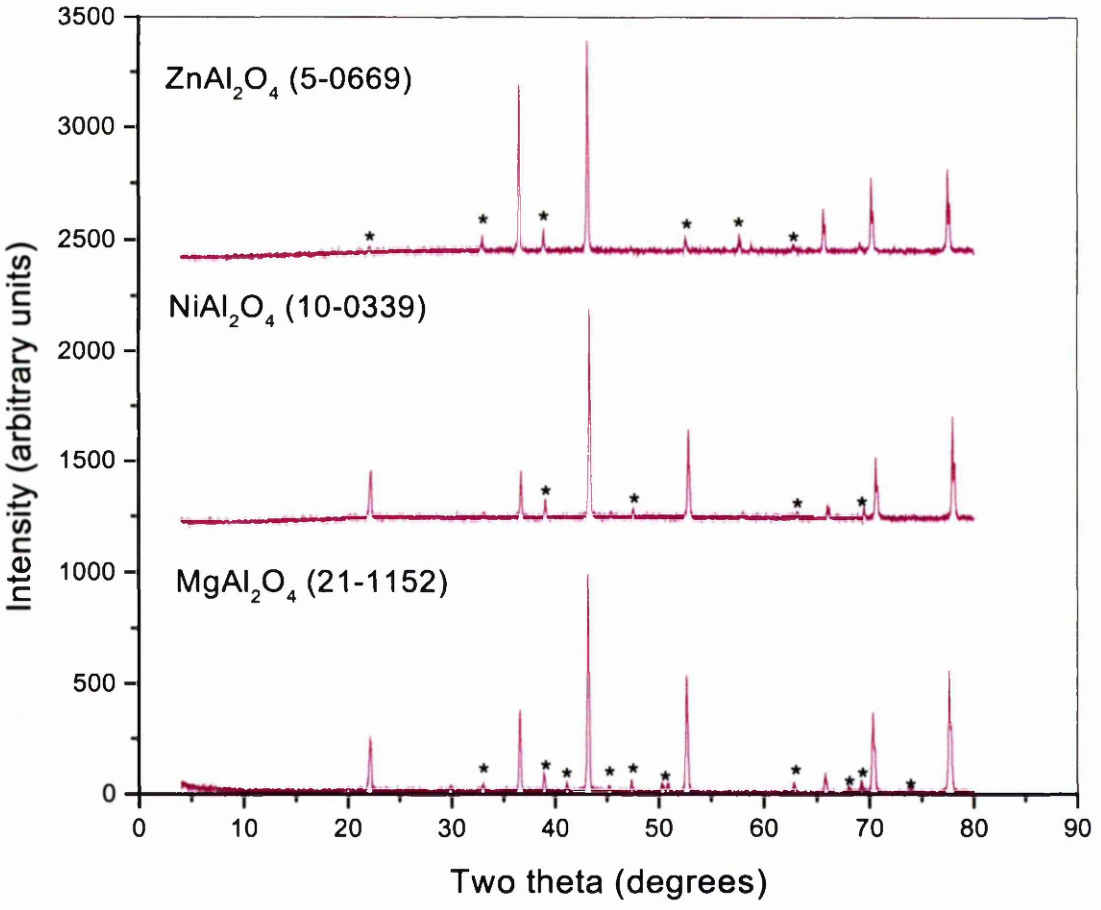

Figure 4.3 *The XRD patterns from the aluminate spinels. The small impurity peaks marked with asterisks are assigned to instrumental effects.*

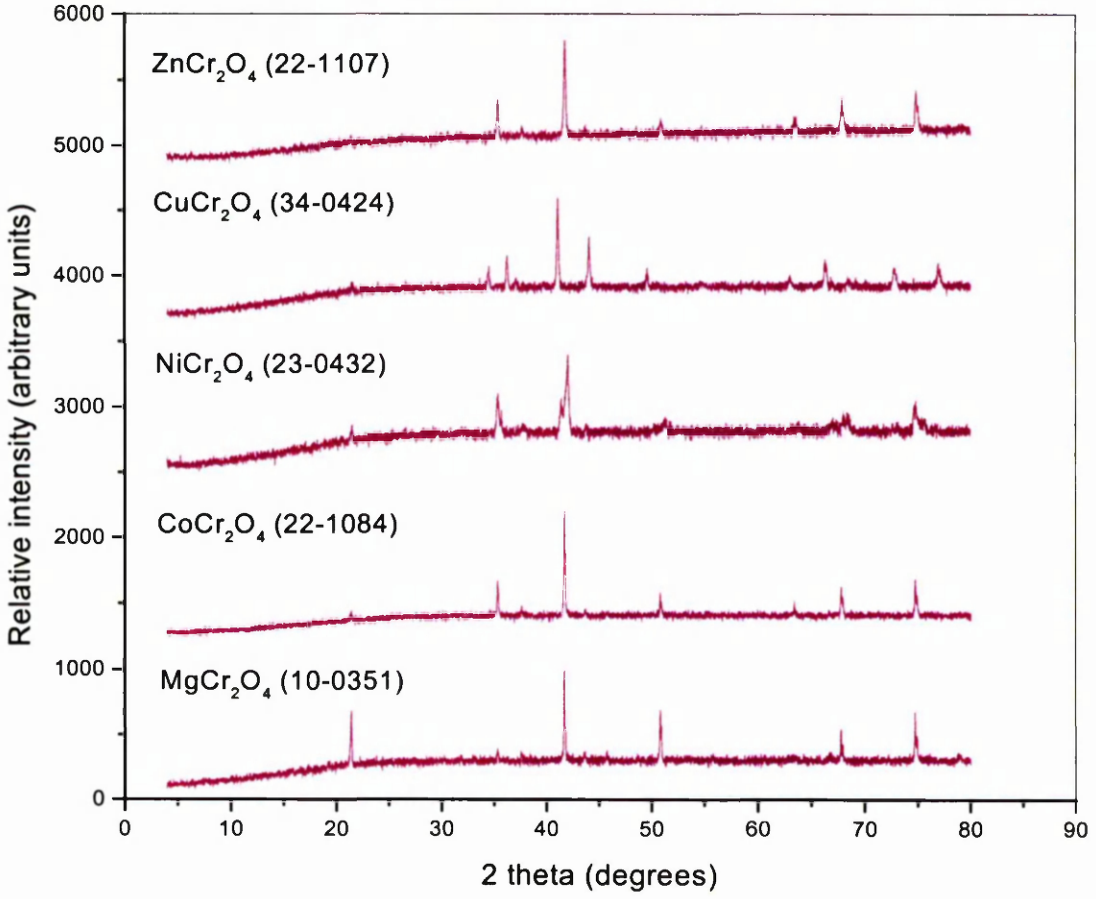

Figure 4.4 XRD spectra from the chromite spinels

Figure 4.4 shows the XRD results from the chromites. The background on these spectra is much bigger due to fluorescence effects, resulting from the cobalt source X-rays inducing emission of chromium characteristic X-rays from the samples, as described in section 4.4.1. It is interesting to note that there is some splitting in the main peak for nickel chromite. This is because this compound is slightly tetragonal, with a c/a ration of 1.02, as discussed in section 4.3.3. In the XRD pattern for copper chromite, which has a c/a ratio of 0.91, the main peak has completely split and extra peaks appear in the pattern due to the removal of the degeneracy of sets of planes such as (112) and (211).

The results from the ferrites are shown in figure 4.5. The samples appear to be single phase, with the exception of a couple of very low intensity peaks in the nickel ferrite and zinc ferrite samples, which have again been marked by an asterisk. There is a hint of these peaks in the other ferrites, but their presence cannot be confirmed in those cases. These occur at the same angle as the extra peaks found in the aluminate samples which were assigned to instrumental effects. It may be that these effects are common to all the spinels, and their visibility depends on their intensity relative to the most intense peaks for the aluminates and ferrites. In the case of the chromites, the large background due to fluorescence effects would obscure them.

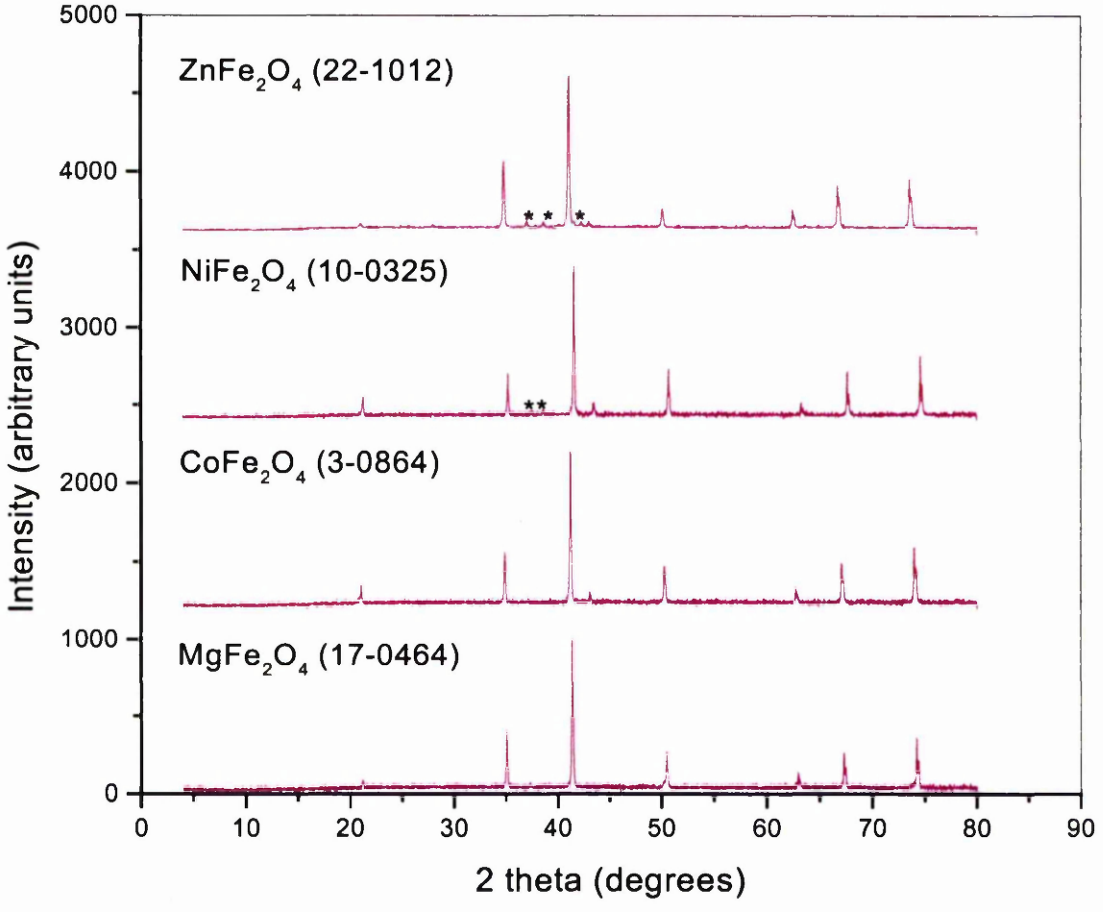

Figure 4.5 The XRD patterns from the ferrite spinels

4.3.3 Neutron diffraction experiments

Powder neutron diffraction data were collected on the medium resolution, high intensity powder diffractometer, POLARIS, at the ISIS facility at the Rutherford Appleton laboratory. Neutrons are produced at ISIS by bombarding a tantalum target with high-energy protons. This spallation process yields around 15 neutrons per proton, giving a high neutron flux suitable for diffraction experiments.

A schematic diagram of the Polaris powder diffractometer is shown in figure 4.6. Unlike in X-ray diffraction where a monochromatic source and variable collection angle are used, POLARIS employs the time-of-flight technique, in which the diffraction angle is fixed, and neutrons with a variety of wavelengths are used. The relation between the time-of-flight of the neutrons and the d-spacings in the crystal lattice can be derived by considering the wavelengths of the neutrons and the distance they travel. The neutron wavelength can be expressed as shown in equation 4.1

$$\lambda = \frac{h}{mv} \tag{4.4}$$

where h is Planck's constant and m and v are the mass and velocity of the neutron respectively. The neutron velocity is simply related to the distance travelled, d, and the time-of-flight, t as

$$v = \frac{L}{t} \tag{4.5}$$

Equations 4.4 and 4.5 can be combined with Bragg's equation (4.2) to relate the time-of-flight to the lattice parameter, d as

$$t = \frac{2mL}{h} d \sin\theta \tag{4.6}$$

Since L is a constant for the detector and h and m are constants, $t \propto d$, and the d-spacings are discriminated by the time of the arrival of the neutrons at the detector. This set-up takes advantage of the full "white" spectrum, greatly reducing the time required to collect high quality data.

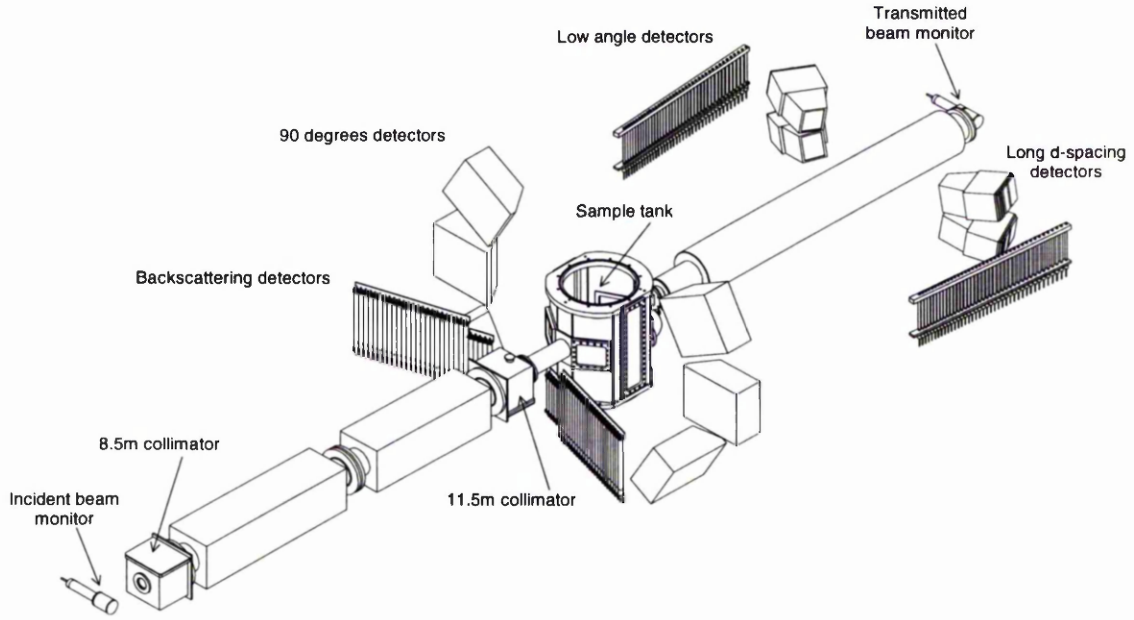

Figure 4.6 *The POLARIS powder diffractometer at the ISIS neutron source. The diagram is from the POLARIS User Guide, courtesy of Dr. R. Smith.*

The instrument receives a polychromatic beam of neutrons from the ambient temperature water moderator, and the incident and transmitted neutron flux is monitored by two low efficiency glass scintillator detectors ~4m before the sample position and ~2.5m after it. Two sets of collimators in the incident beamline allow the beam size to be reduced to match the sample size therefore minimising the background from the sample equipment environment. POLARIS has four banks of detectors. Two banks of ZnS scintillator detectors are placed at a low angle, and at $2\theta \sim 90^{\circ}$. Two banks of ^{3}He gas detectors are arranged at low angles and at backscattering angles.

4.3.3 **Rietveld Refinement**

In this technique least-squares refinements are carried out until the best fit is obtained between the entire observed powder diffraction pattern taken as a whole, and the entire simulated pattern. The diffraction pattern is recorded as a series of intensities, y_is, at each of several thousand increments, i, in the pattern. The best fit sought is the best least-squares fit to all of the thousands of y_is simultaneously until the residual, S, as defined in equation 4.7 is minimised.

$$S_y = \sum_i w_i (y_i - y_{ci})^2 \qquad (4.7)$$

where $w_i = \frac{1}{y_i}$,

y_i = observed (gross) intensity at the ith step,

y_{ci} = calculated intensity at the ith step,

and the sum is over all data points. The calculated pattern is simultaneously based on the refined models for the crystal structure, instrumental effects and other specimen characteristics such as lattice parameter, which all contribute to the number and position of the peaks, and their intensities, as described by equations 4.2 and 4.3 in section 4.3.2. A detailed review of this method can be found in the book edited by Young (1992).

Figure 4.7 shows the neutron diffractograms acquired at POLARIS. Structures were refined by Dr. Skakle, of the University of Aberdeen, using the program TF14LS (Smith and Hull, 1994 and David *et al*, 1992) using data collected over the time-of-flight range 1400-19500μs in the highest resolution, back-scattering detectors. For the refinements, the occupancies of all sites were constrained to be full, and the overall

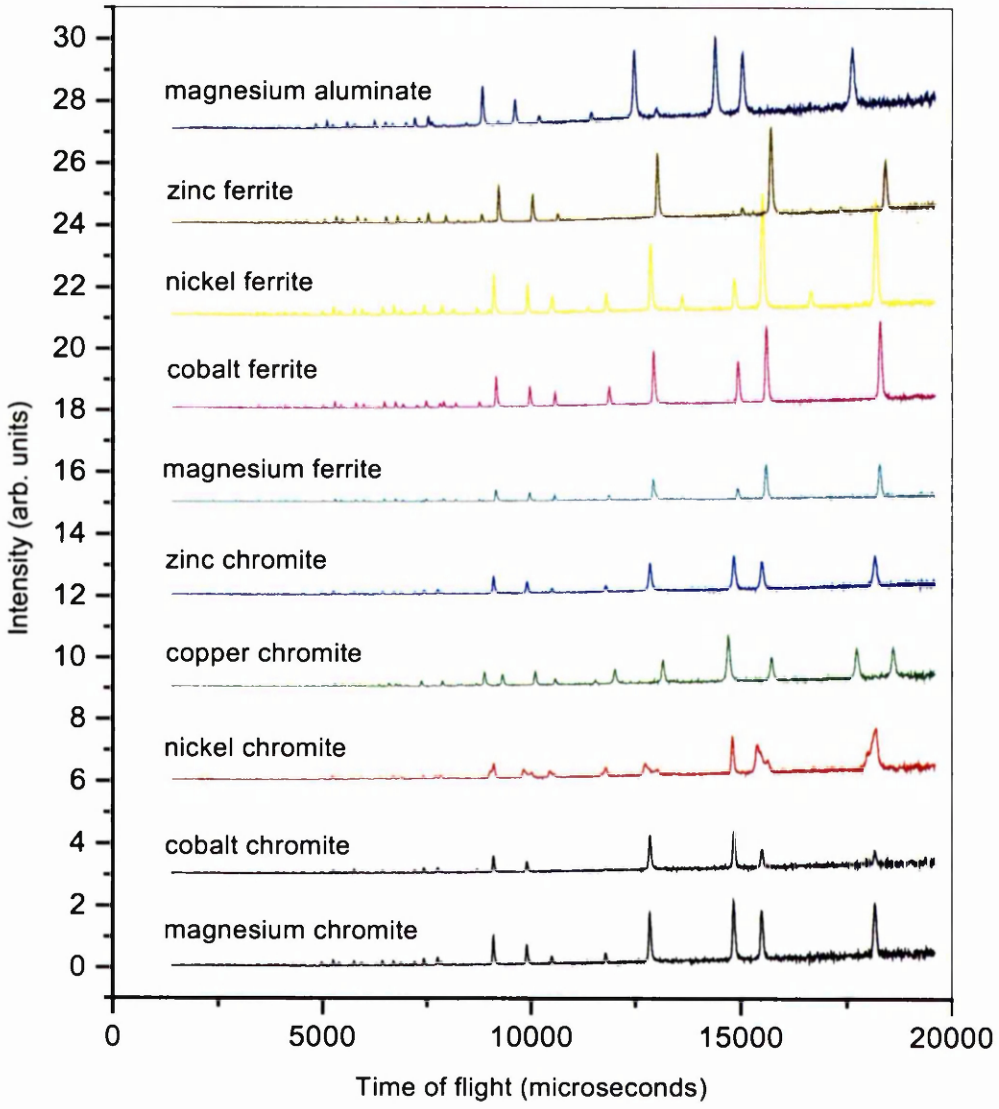

Figure 4.7 *The diffraction patterns obtained by time-of-flight neutron diffraction at POLARIS.*

stoichiometry of each spinel was constrained to be AB_2O_4. A silicon standard was used for an instrument calibration. Figure 4.8 shows the simulated and experimental data from magnesium aluminate and the difference between the two profiles.

The nickel aluminate and zinc aluminate samples were synthesised after the beam-time at the neutron facility. However, the atomic numbers of the elements in these compounds are sufficiently far apart that the refinements could be carried out using high quality XRD data. For these compounds the refinements were performed using

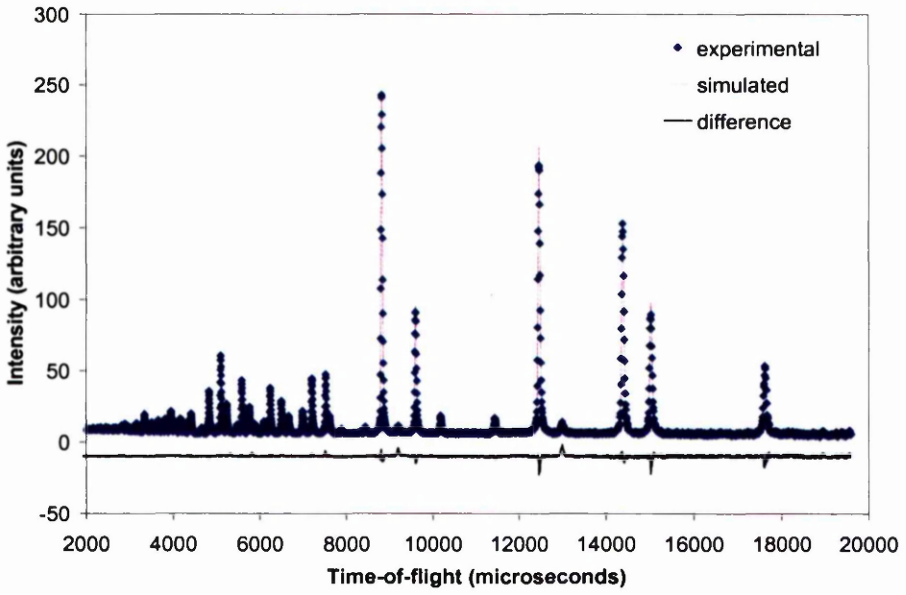

Figure 4.8 *The experimental and simulated neutron diffraction patterns for magnesium aluminate, and the difference between the spectra.*

data from a Stoe Stadi/P automated diffractometer covering a 2θ range of 8-114 degrees. Structures were refined using the Generalised Crystal Structure Analysis System (GSAS) program (von Dreele and Larson, 1998), with the same constraints as for the neutron data.

The lattice parameters, oxygen parameters and degrees of inversion obtained by the Rietveld refinements are given in table 4.2. The figures in brackets for each value give the estimated standard deviations in the final, and sometimes penultimate, figures, based on the fits between the calculated and observed patterns. For some of the chromite samples the refinement of the occupancies showed the samples to be completely normal, so they were not refined in the final cycle, and hence no error is quoted for them. In the highly symmetric cubic compounds, only one oxygen parameter is required to determine the position of the oxygen ions, *i.e.* there will be an

Compound	a(Å)	c(Å)	u	λ
$MgAl_2O_4$	8.08098(2)	8.08098(2)	0.26116(2)	0.320(9)
$NiAl_2O_4$	8.05222(7)	8.05222(7)	0.2558(4)	0.926(8)
$ZnAl_2O_4$	8.0957(7)	8.0957(7)	0.2639(3)	0.042(9)
$MgCr_2O_4$	8.33202(1)	8.33202(1)	0.26124(1)	0(-)
$CoCr_2O_4$	8.33216(2)	8.33216(2)	0.26171(1)	0.031(6)
$NiCr_2O_4$	5.84398(3)	8.41528(9)	0.47983(17) 0.26451(14)	0.000(4)
$CuCr_2O_4$	6.03137(3)	7.78388(6)	0.46529(5) 0.24649(5)	0.034(5)
$ZnCr_2O_4$	8.32800(2)	8.32800(2)	0.26161(1)	0(-)
$MgFe_2O_4$	8.38087(2)	8.38087(2)	0.25623(4)	0.875(8)
$CoFe_2O_4$	8.38730(1)	8.38730(1)	0.25641(4)	0.819(4)
$NiFe_2O_4$	8.33952(1)	8.33952(1)	0.25568(5)	1.0(-)
$ZnFe_2O_4$	8.44330(1)	8.44330(1)	0.26054(2)	0.042(4)

Table 4.2 *Crystallographic data obtained by Rietveld refinement of the X-ray and neutron diffraction results. The figures in brackets for each value give the estimated standard deviations in the final, and sometimes penultimate, figures, based on the fits between the calculated and observed patterns.*

oxygen ion at *u,u,u*. In the tetragonal unit cell, which has lower symmetry, the oxygen positions are defined using two oxygen parameters, *i.e.* there will be an oxygen ion at (0, 0.465, 0.264) in copper chromite. For all the spinels the positions of the other oxygen ions can be found by applying translations to the oxygen parameters. These translations are given in the International Tables for Crystallography (1995), under the appropriate space groups: Fd3m and I4(1)/amd for the cubic and tetragonal compounds, respectively. The results are in good agreement with previously published results which were obtained from the Inorganic Crystal Structure Data File (ICSD) in the EPSRC's Chemical Database Sevice (CDS) at Daresbury (Fletcher *et al*, 1996).

4.4 Energy-dispersive X-ray analysis

4.4.1 Introduction

XRD is a quick and easy technique for confirming the identity of a product and finding and identifying any impurities present. However, the technique is not sensitive enough to detect impurity levels of less than a few percent. In syntheses of this type it can also be difficult to detect small amounts of unreacted material by XRD, since some reactants have crystal structures that are incorporated in the structure of the product. This means that the reactant's main diffraction peaks may be close to those of the products. For example, it is difficult to detect small amounts of unreacted MgO in $MgFe_2O_4$ because the main diffraction lines for the reactant occur at the same positions as some of the spinel lines.

Therefore energy-dispersive X-ray analysis (EDX) has also been used to estimate the purities of the products. In this technique a high-energy electron beam induces the emission of characteristic X-rays from the sample, which are collected and measured to give spectra which are plots of X-ray counts against X-ray energy. The procedure is carried out in a transmission electron microscope, so it is possible to analyse the chemical composition of individual grains of material, unlike XRD, which is a bulk technique. As well as identifying impurities, the ratio of the elements presents in the particles can be determined to ascertain the homogeneity of the sample. Williams and Carter (1996) give a good introduction to this technique.

4.4.2 Generation of characteristic X-rays

When a high-energy electron beam is inelastically scattered by a sample, the energy given to the specimen can result in the excitation of core electrons to the conduction band. The excited atom returns to a lower energy configuration by replacing the missing core electron with one of the outer shell electrons. The emission of a characteristic X-ray or an Auger electron accompanies this transition. The energy of the emission depends on the difference in energy of the two electron shells involved, and is therefore characteristic of the element involved. This process is illustrated in figure 4.9.

The other mechanism for the production of X-rays results from the interaction of the electron beam with the Coulomb field of the nucleus. This interaction slows the electrons and results in the emission of X-rays. Since the magnitude of deceleration of the electrons depends on the degree of interaction between the electrons and atom, the amount of deceleration is continuous, and X-rays are therefore emitted with energies up

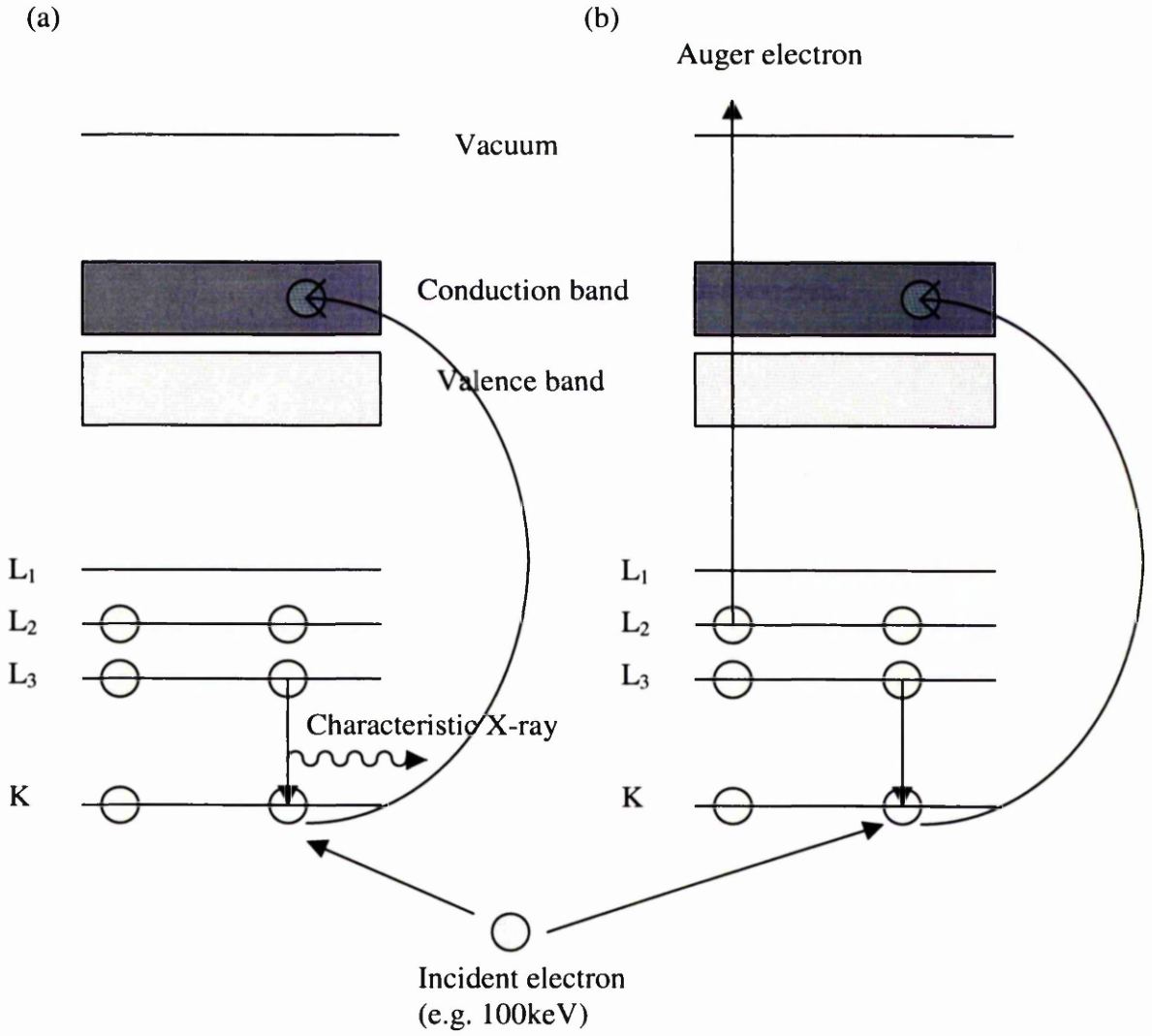

Figure 4.9 *Fast incident electrons can excite core electrons in the sample to the conduction band. The system returns to a de-excited state by the emission of (a) a characteristic X-ray or (b) an Auger electron.*

to the energy of the incident electrons. This process is known as "bremsstrahlung", which is German for "braking radiation". It results in a continuous spectrum on which the characteristic X-rays are superimposed.

4.4.3 The EDX detector

There are a number of types of EDX detector, some of which are particularly suited to low-energy X-rays or intermediate voltage analytical microscopes, for example. In this discussion the system considered is a lithium-doped silicon detector with a beryllium window, since this is the most common type, and has been employed in most experiments.

In an EDX detector the incoming X-rays pass through a thin beryllium window and interact with a layer of lithium-doped silicon. The interaction of the X-ray with the semiconductor detector generates electron-hole pairs, the number of pairs generated depending on the X-ray energy. The purpose of the lithium is to fill any recombination sites, thus creating a region of intrinsic silicon. The electron-hole pairs are separated by an applied bias. This charge pulse is converted to a voltage, then amplified through a field effect transistor, and then identified electronically as resulting from an X-ray of specific energy. The signal is then assigned to that energy in the multichannel analyser and stored.

Figure 4.10 shows a typical X-ray spectrum from cobalt chromite. The oxygen K_α peak, which has an energy of ~532eV is not present since this spectrum was recorded on a beryllium window detector, which absorbs low energy-X-rays. Elements with a lower atomic number than sodium cannot be detected using beryllium window detectors, since their X-rays are not high enough in energy to travel through the beryllium window without being absorbed. The copper lines are due to the copper grid which supported the sample in the microscope. The intensity of the bremsstrahlung is maximum at an energy of ~1.8keV. This is because it is far more likely that the braking

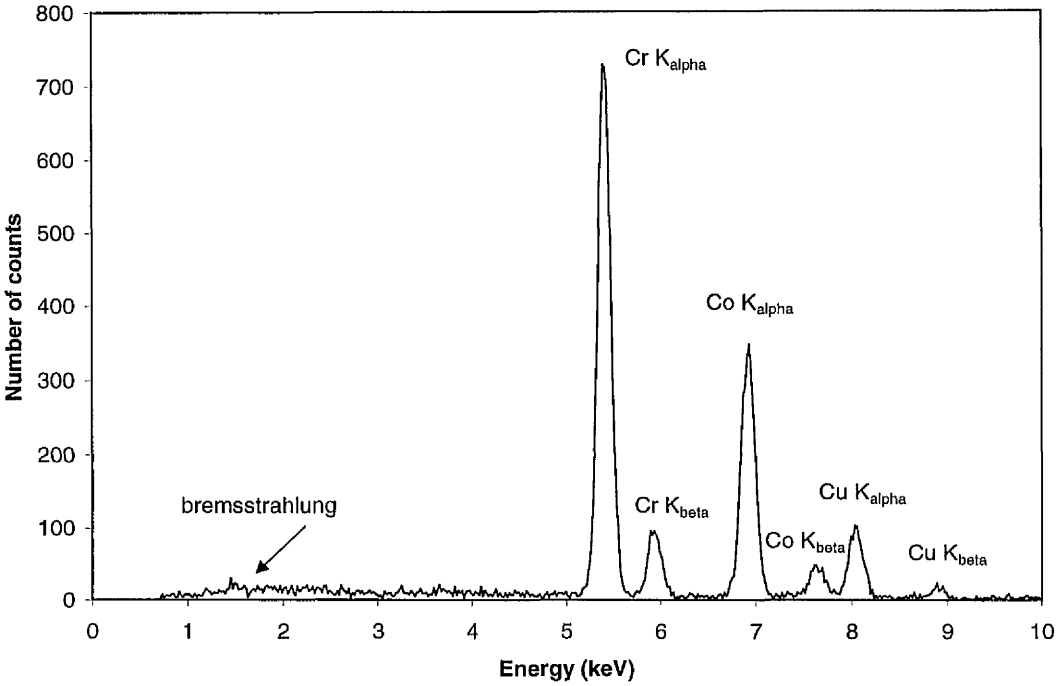

Figure 4.10 Typical EDX spectrum recorded from cobalt chromite using a lithium doped silicon detector with a beryllium window.

event causes a small loss of energy, rather than the electron losing all of its energy in one deceleration (Williams and Carter, 1996). At low energy the intensity drops to zero since the low-energy bremsstrahlung is absorbed by the detector.

4.4.4 Acquisition of EDX data

An EDX spectrum was recorded from each particle from which EELS data was acquired, on the HB5 STEM. This microscope is fitted with a beryllium window, lithium-doped silicon detector. Since X-rays with energies less than ~1kV are strongly absorbed by beryllium windows, K_α X-rays from elements below about sodium in the Periodic Table cannot be detected. Therefore it was possible to record the metal peaks of interest, but the oxygen signal could not be detected.

There were two reasons for recording the EDX spectra. Firstly, XRD can only detect the presence of impurities with concentrations greater than a few percent. To check for lower levels of impurities, an energy-dispersive X-ray analysis (EDX) spectrum was recorded for each particle from which EELS data was obtained. To derive the minimum impurity level detectable, the criterion that a peak is real if the peak intensity is greater than three times the standard deviation of the counts in the background under the peak (Williams and Carter, 1996) was assumed. It is estimated that for a typical acquisition time of 100 seconds, impurity levels greater than ~0.3% could be detected by EDX, a factor of ten greater than by XRD. However, none were found to be present above this level. Secondly, the ratio of the metal lines gave an estimate of the homogeneity of the samples, since it would be easy to identify particles that were particularly deficient or rich in a specific element. No attempt was made to quantify this ratio, and an estimate of the relative ratio of the metals was only made by eye.

4.5 Nuclear magnetic resonance

4.5.1 NMR theory

Magnetic nuclei possess an intrinsic angular momentum known as spin. The spin quantum number I is determined by the number of unpaired protons and neutrons, and normally has the value of 0, 1/2, 1, 3/2, 2,.., and is normally less than 4. The application of a static magnetic field, B_o, removes the degeneracy of the spin energy levels, giving rise to $2I+1$ such levels. If $I=1/2$, the nucleus has two energy levels and behaves as a magnetic dipole. If $I \geq 1$, the nucleus has more than two energy levels. The consecutive

energy levels are each separated by an energy ΔE, which depends on the strength of the interaction between the nucleus and the field.

The aim of the NMR experiment is to measure the frequency of the radiation required to induce transitions from one nuclear spin state to another, for a given field. The frequency, ν, required is related to the applied magnetic field, B_o, by

$$\nu = \frac{\gamma B_o}{2\pi} \tag{4.8}$$

where γ is the gyromagnetic ratio, which is the constant of proportionality relating the angular momentum, $\boldsymbol{I}$, to the magnetic moment, μ, by

$$\mu = \gamma \boldsymbol{I} \tag{4.9}$$

However, the resonant frequency also depends on the local structural environment of the atom, since the electrons in the vicinity of the nucleus shield it from the applied magnetic field by different amounts in different types of sites. This means that equation 4.8 has to be modified to

$$\nu = \frac{\delta B_o}{2\pi}(1-\sigma) \tag{4.10}$$

where σ is the shielding constant. Therefore different resonant frequencies are required for the same type of atoms in different environments. These are reported in terms of the chemical shift, which is the difference between the resonance frequency of the nucleus being studied, ν, and that of a standard, ν_o. These shifts are independent of the applied field and are reported as parts per million (ppm) on the δ-scale which is defined as

$$\delta = \frac{\nu - \nu^o}{\nu^o} \times 10^6 \tag{4.11}$$

4.5.2 Solid state NMR

The main problems associated with the application of NMR to solids are poor resolution and broad linewidths. There are two main contributions to the linewidth. The first contribution is due to direct dipolar interactions, which arise from the fact that a magnetic nucleus, *A*, behaves as a dipole and generates a secondary field, *b*, at neighbouring nuclei, *B*. The magnitude of this field is

$$b = -\frac{\gamma\hbar m_I \mu_o}{4\pi r^3}(1-3\cos^2\theta) \qquad (4.12)$$

where m_I = I, I-1,.....,-I

μ_0 is the permeability of a vacuum

r is the distance between the two nuclei

θ is the angle between the z-axis, which is also the direction of the applied field, B_o, and the vector that joins the two nuclei,

as illustrated in Figure 4.11.

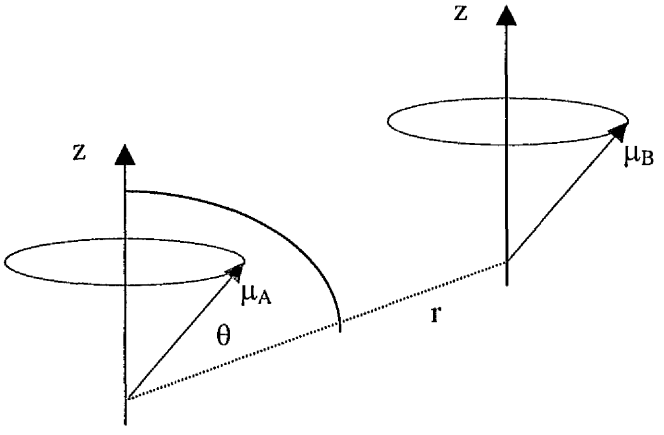

Figure 4.11 Magnetic nucleus A behaves as a dipole and generates a secondary magnetic field at nucleus B.

Half of the spins of the neighbouring nuclei experience direct dipolar interactions which oppose the applied field, B_o, and therefore require a larger field to induce a transition,

for a given frequency. However, the other half of the spins experience a field in the same direction of B_o and therefore require a reduced field to induce a transition. This results in a splitting of the NMR line, as shown in Figure 4.12. These interactions can be neglected in fluids since they average out to zero in that state of matter.

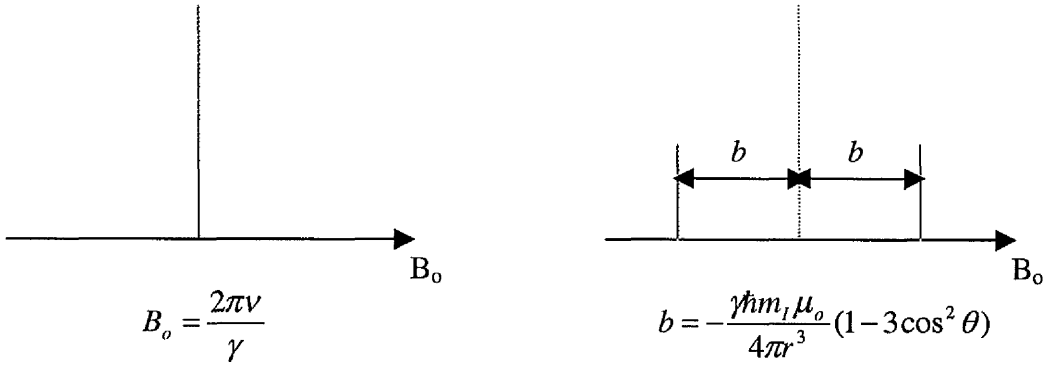

Figure 4.12 Direct-dipolar interactions cause a single line to split into two at lower and higher fields.

The second contribution to the linewidth is the anisotropy of the chemical shift. These shifts arise because the applied field induces the generation of electron currents in molecules as predicted by Lenz's law. They are dependent on the orientation of the molecule relative to the applied field, and vary as $(1-3\cos^2\theta)$. In solution the molecules tumble rapidly and so an average chemical shift value is relevant.

These contributions to the linewidth both have a $(1-3\cos^2\theta)$ term. As shown in figure 4.13, by spinning the sample such that the angle between the molecule's principal axis and the applied field is 54.74°, the $(1-3\cos^2\theta)$ term becomes zero and these contributions vanish. 54.74° is known as the magic angle, and the technique is known as magic angle spinning (MAS) NMR.

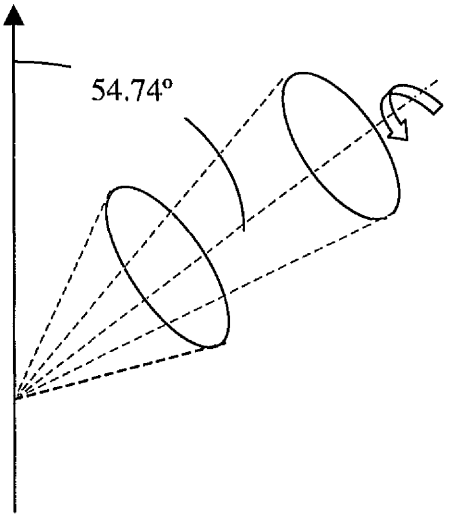

Figure 4.13 *By spinning the sample at the magic angle the internuclear vectors have an average orientation of 54.74° and the direct-dipolar interactions and anisotropy of the chemical shift average out to zero.*

4.5.3 MAS NMR instrumentation and experimental conditions

All MASNMR experiments were carried out at the NMR facility at the University of Durham. The ^{27}Al spectra were acquired at 78.2 kHz on a Varian UNITY*plus* spectrometer, equipped with a 7 Tesla magnet, and a 5mm Doty Scientific dual-channel MAS probe. Powdered samples were rotated in zirconia rotors at the angle of 54°.74 to the magnetic field vector at spinning speeds of 9.3 – 10.5 kHz. These spinning speeds were chosen to minimise the overlap of the spinning sidebands with the central peaks of interest as discussed by Millard *et al*, (1992).

The ^{27}Al MAS NMR spectra were collected at room temperature using a pulse width of 1μs or about $\frac{\pi}{9}$ relative to the solution $\frac{\pi}{2}$ (90°) pulse width (4.5μs), measured using a 1 molar aluminium trichloride solution. This pulse width is the duration of the radiofrequency field used for excitation of the nuclear spin system. It has been shown

that the relative peak intensities of the central lines in the MAS NMR spectra of ^{27}Al nuclei are dependent on pulse width, (Millard *et al*, 1992 and references therein). Since the inversion parameter is determined by the relative intensities of the central peaks, it in turn is dependent on the pulse width. Millard *et al*, (1992), have shown that the inversion parameter remains independent of pulse width, up to a maximum pulse width of 1.51μs. The 1μs chosen was well below that maximum, and therefore had no influence on the degree of inversion. The time between pulses of radiation, to allow the system to return to equilibrium, was investigated in the range 0.2 to 5 seconds. The degree of inversion was found to be independent of the delay time so a delay of 2s between pulses was chosen. Chemical shifts are reported relative to ^{27}Al in 1 molar solution aluminium trichloride at room temperature.

4.5.4 Results and comparisons to other techniques

The ^{27}Al MAS NMR spectra recorded for magnesium aluminate and zinc aluminate are shown in Figure 4.14. A spectrum could not be obtained for the nickel aluminate sample due to the magnetic nature of the Ni^{2+} ion. The spectra and chemical shifts are consistent with those of previous studies (for example, Millard *et al*, 1992 and Wood *et al*, 1996). To obtain the areas under the tetrahedral and octahedral peaks, a smooth curve was fitted to the rolling baseline for each spectra, and the area under each peak integrated. The inversion parameter, λ, is related to the intensities of the peaks by

$$\lambda = \frac{2}{\left(1+\left(\frac{^{[6]}Al}{^{[4]}Al}\right)\right)} \qquad (4.13)$$

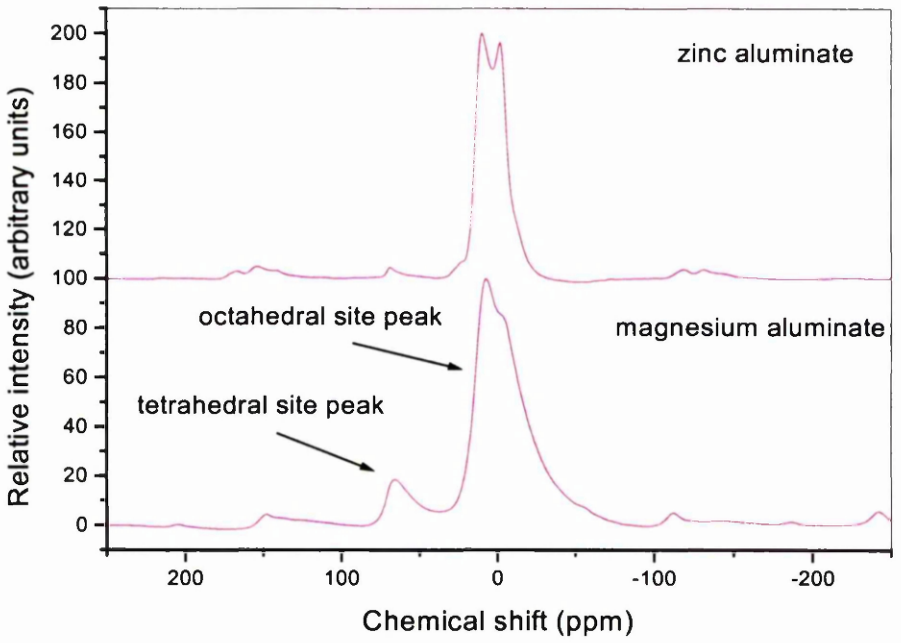

Figure 4.14 *^{27}Al MAS NMR results for magnesium aluminate and zinc aluminate.*

for λ greater than zero. The degrees of inversion for these samples are listed in Table 4.3 and the results obtained by neutron diffraction are included for comparison. It can be seen that there is very good agreement between the two techniques.

Compound	Inversion Parameter (λ)	
	^{27}Al MAS NMR	Rietveld Refinement
$MgAl_2O_4$	0.344	0.320(9)
$ZnAl_2O_4$	0.038	0.042(9)

Table 4.3 *Comparison of inversion parameters for magnesium aluminate and zinc aluminate by ^{27}Al MAS NMR and Rietveld refinement of diffraction data.*

It was mentioned in section 1.5.2 that the degree of inversion is sensitive to many factors, including the thermal history of the sample. A number of studies have been reported where changes in the degree of inversion were induced by heating the sample

to change the cation distribution, and then quickly quenching the sample to lock in the high temperature arrangement (for example, Schmocker and Waldner, 1976, Mocala *et al*, 1989, Millard *et al*, 1992, Roelofsen *et al*, 1992 and Wood *et al*, 1996). Attempts were made to produce a series of spinels with different degrees of inversion so that the sensitivity of the near edge structure to the cation distribution could be investigated.

The procedure followed was to heat the samples at a variety of temperatures between 600 and 1000°C, for between two and six weeks, and then quench the samples in chilled salt water. Neutron diffraction and ^{27}Al MAS NMR were also used to obtain the degrees of inversion for these samples.

Table 4.4 shows that similar results are again obtained by both techniques. However, the heat treatments were largely unsuccessful, in so far as only very small changes in the degree of inversion were induced. The only trend that can be observed is that the general process of heating has induced a small reduction in the inversion parameter, which is almost independent of the heating temperature. It is also interesting to note that the quenching experiments have lowered the degree of inversion, whereas all other reported experiments of this type already referred to have increased the inversion parameter. This indicates that the material was initially in an unnaturally highly inverse state, which may be due to the way the sample was synthesised. The material used for these experiments was bought commercially, so the synthesis method is unknown. The other possibility could be that impurities in the sample could influence the inversion. However, this can be ruled out as no impurities have been found in the sample by EPMA or EDX, as discussed in section 4.3.2.

Heating temperature (°C)	Heating time (weeks)	Degree of Inversion (λ)	
		^{27}Al MAS NMR	Rietveld Refinement
600	2	0.30	0.269(8)
600	8	Not available	0.264(8)
700	2	0.28	0.262(8)
800	2	0.29	0.263(7)
900	2	0.27	0.249(8)
1000	2	0.30	0.279(7)

Table 4.4 *Inversion parameters for the heat-treated samples of magnesium aluminate, obtained by ^{27}Al MAS NMR and Rietveld refinement of diffraction data.*

The heating periods are comparable with those in the literature, so the samples had time to reach a high-temperature equilibrium state. To check that the heating periods were not too short, one sample was heated for 8 weeks, as opposed to 2 weeks for the rest of the samples. However, the inversion parameter for this sample is comparable to the others, indicating that the extra time had no effect. Therefore it is thought that the reason for the poor results is that the time taken to remove the samples from the furnace was too long and allowed the samples to reach equilibrium before they were quenched. It is well known that the cations quickly redistribute. For example, the only way the inversion parameter can be recorded above 1000°C is *in situ*, since no one has been able to quench samples quickly enough to lock-in the high temperature cation distribution above this temperature. No facilities were available to improve the quenching method, so no further progress was made with this series of experiments.

Chapter 5

The Oxygen K-edge in Spinels

5.1 Introduction

In this chapter the results of a systematic study of the oxygen K-edge ELNES from a series of aluminium, chromium and iron containing spinels are presented. Extra fine structure in the region up to 10eV above the edge onset is observed for the chromium and iron-containing compounds, and is assigned to transitions to states created by mixing of oxygen 2p and metal 3d orbitals. The possible fingerprints in the oxygen K-edge ELNES corresponding to a high degree of inversion in the spinel structure and for tetragonal distortions of the cubic structure are discussed. Simulations of the experimental data using the multiple scattering code FEFF8 are presented. Good agreement was obtained in the

case of magnesium aluminate, but relatively poor agreement was obtained in the cases of the chromites and ferrites. For a full interpretation of the ELNES present on the oxygen K-edges, the cation edges must also be considered. These will be addressed in chapter 6.

5.2 Substitution of the metal (III) ion

5.2.1 General observations

Figure 5.1 shows the oxygen K-edges from the compounds whose crystallographic data are given in table 4.2. The spinel compounds investigated were selected to illustrate the effects on the ELNES of introducing different elements into both the normal and inverse crystal structures. As discussed in Chapter 1, the general formula of a spinel is AB_2O_4, where the A and B cations have formal charges of +2 and +3, respectively. In figure 5.1 the columns show the effect of changing the A^{2+} cation while keeping the B^{3+} cation the same. Conversely, the rows show the effect of changing the B^{3+} metal ion while keeping the A^{2+} metal ion the same. In the case of a normal spinel, the columns in figure 5.1 correspond to systematically varying the cation in the tetrahedral sites, while the rows illustrate systematic variation of the octahedral site metal. However, some of the spinels studied are partially or fully inverse, so the substitution of one element varies the metal on both types of sites in some cases.

In the aluminates in the left hand column of figure 5.1, each spectrum shows a peak, labelled D, with a low energy shoulder, D*, followed by two less intense peaks at higher

energies, the first of which is labelled E. This general shape is in good agreement with spectra of magnesium aluminate published by other workers (for example, Köstlmeier *et al*, 1999 and van Benthem and Kohl, 2000). The oxygen K-edge ELNES for the other aluminates studied have not been published to the best of my knowledge, so there are no data to make comparisons with. In the case of zinc aluminate, peak E has split into two features and the peak at higher energies has developed a shoulder on the low energy side. For nickel aluminate, a small pre-peak, X, is clearly visible. This is absent for zinc aluminate but there is a hint of a weak pre-peak for magnesium aluminate. The intensity of the pre-peak in magnesium aluminate was observed to vary between different grains of material but was very weak for most grains studied. This will be discussed in section 5.3.2.

When Al^{3+} is replaced by Cr^{3+}, the middle column of figure 5.1 shows that there is a major change in the shape of the oxygen K-edges. While the spectra from the chromites show features similar in shape to D*, D and E in the aluminates, there are now additional peaks prior to D*, labelled A, B and C. Peaks A and B are similar in all the chromites but peak C changes with the nature of the A^{2+} ion. The structure of the peaks beyond E is more complex than in the aluminates and changes with the nature of the A^{2+} ion. Finally copper chromite shows a pre-peak labelled Y.

With the exception of peak C, the chromite oxygen K-edges show similarities to those of the binary transition metal oxides M_2O_3, where M = Sc, Ti, V, Cr or Fe, and MO_2, where M = Ti, V or Mn (de Groot *et al*, 1989). In these binary oxides the spectra have two well-defined peaks at the edge onset, which can be compared to peaks A and B in figure 5.1,

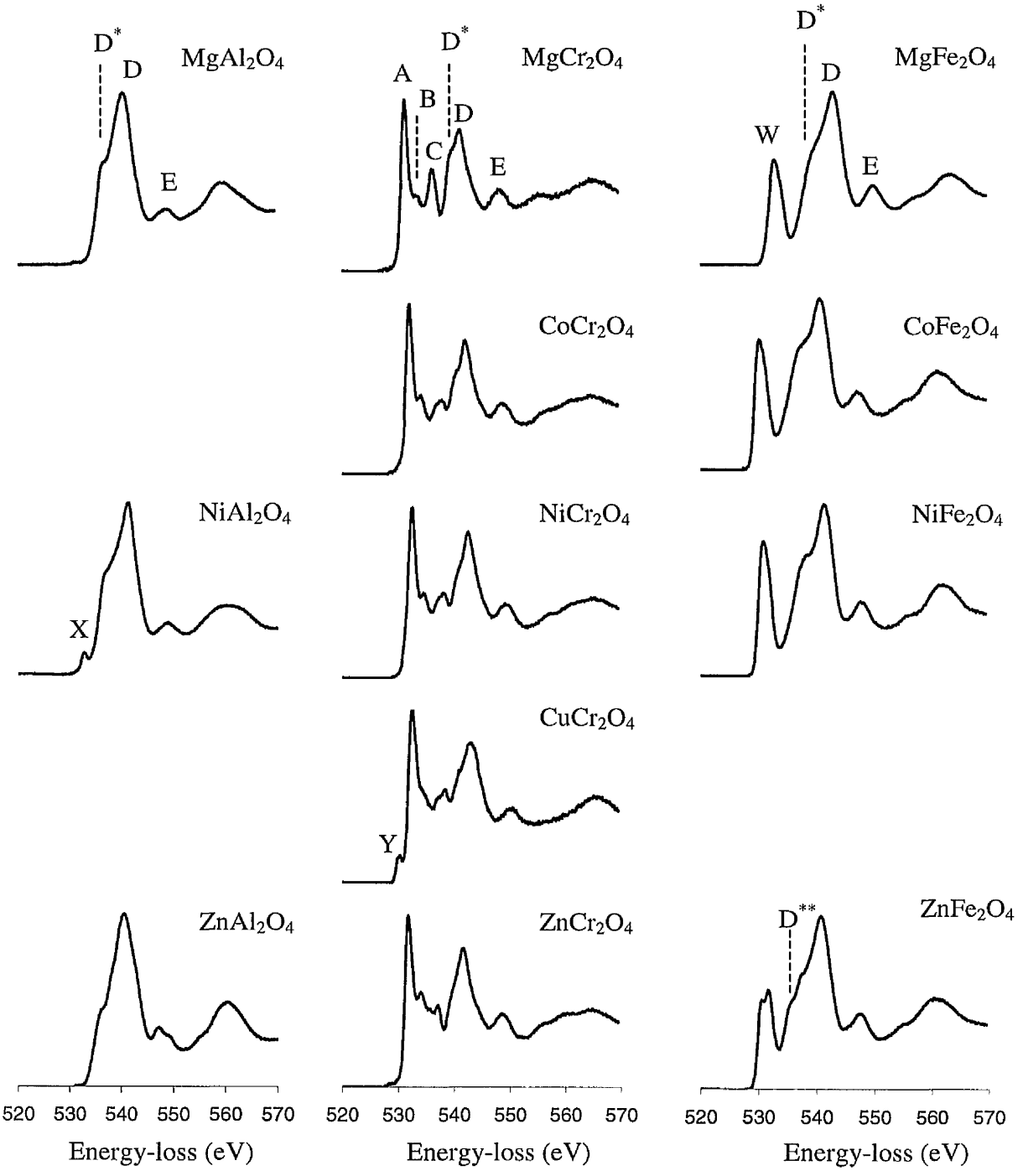

Figure 5.1 The oxygen K-edges from the spinels studied. The y-axis represents the intensity in arbitrary units. The spectra have been normalised to the height of the highest peak in each spectrum.

and a broad peak with a shoulder on the low energy side, which can be compared to features D and D* in the spinel spectra. In the binary oxides previous workers have assigned features similar to those labelled A and B in the chromite spectra as transitions to additional states of p-like character on the oxygen sites resulting from hybridisation of oxygen 2p and metal 3d orbitals (de Groot *et al*, 1989).

The right-hand column of figure 5.1 shows that the replacement of Al^{3+} or Cr^{3+} by Fe^{3+} also has a significant effect on the ELNES. Comparisons with the aluminates and chromites are complicated by the fact that magnesium ferrite, cobalt ferrite and nickel ferrite are highly inverse, whereas zinc ferrite is normal. The spectra from the ferrites exhibit features labelled D, D^* and E which are also observed for the aluminates and chromites. All ferrite spectra also have the feature labelled W. Although this occurs in the region to the left of the peak D, it cannot obviously be matched to any of the features labelled A, B or C in the chromites.

The shape of peak W is similar for all the ferrites, with the exception of zinc ferrite where it is clearly split into two peaks. The fluorescence yield X-ray absorption spectra of nickel ferrite and zinc ferrite have previously been reported (Pong *et al*, 1996). The EELS data is in good agreement with the X-ray absorption data and splitting of peak W in zinc ferrite and the non-splitting in nickel ferrite is also observed in that study. The relative intensity of peak W, with respect to peak D, is highest for cobalt ferrite and nickel ferrite. The shoulder D^* is also most prominent in the cobalt ferrite and nickel ferrite spectra. There also appears to be a second shoulder, D^{**} in the zinc ferrite spectrum, also observed by Pong *et al.*

5.2.2 The effect of hybridisation on the ELNES

Strong effects due to p-d hybridisation are expected in the unoccupied DOS when the structure contains transition metal atoms with d-bands that are not fully occupied. In the case of non-transition metal atoms such as Al and Mg, the empty 3d orbitals are too high in energy to participate in the hybridisation. In contrast the 3d levels of Zn are similar in energy to the oxygen 2p energy levels but are fully occupied. Therefore, in the samples investigated in this work, strong hybridisation between the metal 3d-orbitals and the oxygen 2p-orbitals would be expected only in the materials containing Cr^{3+}, Fe^{3+}, Co^{2+}, Ni^{2+} and Cu^{2+}. Hybridisation will result in additional unoccupied states of p-character on the oxygen sites for the excited 1*s* core electron to be excited into, and consequently additional features in the ELNES.

It has been shown that in the binary transition metal oxides the intensity of the features associated with the p-d hybridisation decreased as the number of d electrons increased (de Groot *et al*, 1989). Assuming formal oxidation states, the number of d-electrons associated with each type of site in the structure is shown in table 5.1. For the purpose of this argument nickel aluminate, magnesium ferrite, cobalt ferrite and nickel ferrite have been assumed to be completely inverse. The number of holes in the d-orbitals of each atom involved in the hybridisation is likely to be of more relevance to the unoccupied DOS of the material and this is given in brackets in table 5.1. Finally the table also states the number of holes in the d-orbitals per formula unit.

Compound	No. of d electrons (No. of d holes)		d holes per formula unit
	Tetrahedral site metal	Octahedral site metal	
$MgCr_2O_4$	0 (0)	3 (7)	14
$CoCr_2O_4$	7 (3)	3 (7)	17
$NiCr_2O_4$	8 (2)	3 (7)	16
$CuCr_2O_4$	9 (1)	3 (7)	15
$ZnCr_2O_4$	10 (0)	3 (7)	14
$MgAl_2O_4$	0 (0)	0 (0)	0
$NiAl_2O_4$	0 (0)	0 (0), 8 (2)	2
$ZnAl_2O_4$	10 (0)	0 (0)	0
$MgFe_2O_4$	5 (5)	0 (0), 5 (5)	10
$CoFe_2O_4$	5 (5)	7 (3), 5 (5)	13
$NiFe_2O_4$	5 (5)	8 (2), 5 (5)	12
$ZnFe_2O_4$	10 (0)	5 (5)	10

Table 5.1 *The number of d-electrons and holes in the compounds studied. Formal oxidation states and completely normal or inverse degrees of inversion are assumed*

The number of holes in the d-orbitals per formula unit is in the range 14 to 17 for the chromites, 10 to 13 for the ferrites and 0 to 2 for the aluminates. This almost certainly explains the large change in the ELNES when Al^{3+} is replaced by Cr^{3+} but the relatively small changes when the A^{2+} ion is substituted. Similarly, the ferrites have a significant number of holes in the d-orbitals, so peak W can be assigned to transitions to states caused

by the hybridisation of oxygen p and iron d-orbitals. As for the chromites, the substitution of the A^{2+} ion in the ferrites has a relatively small effect on the number of holes, and subsequently has little effect on the fine structure. However, the intensity of peak W, relative to peak D is highest for cobalt ferrite and nickel ferrite, which have more holes than the other ferrite materials. The number of d-holes in the chromium and iron containing compounds are quite similar, but much more detailed fine structure is observed for the chromites, suggesting other factors also influence the observed fine structure. Possible reasons will be considered in the next section.

5.2.3 Magnetic effects on the band structure

The discussion so far has assumed that the crystal orbitals are spin-independent. However, in compounds where the electron spins are magnetically ordered the energy of the spin up and spin down states can be different. This results from the effect on the energies of the exchange interaction, which is attractive between electrons with parallel spin (Cox, 1992). Figure 5.2 shows a simple diagram of a possible spin effect on the band structure for a chromite compound.

This is especially significant for transition metals since the exchange integrals are much higher for 3d orbitals than for the s and p valence orbitals of the non-transition elements (Cox, 1992). Although the long-range magnetic order disappears above the Néel temperature, the effect of the magnetic coupling on the band structure remains. For example, in chromium nitride it has been demonstrated experimentally that the edge shape is independent of temperature over a range from 133K to 533K *i.e.* well above and well

below the Néel temperature of 288K, and this shape is influenced by the antiferromagnetism in this compound (Paxton *et al* 2000).

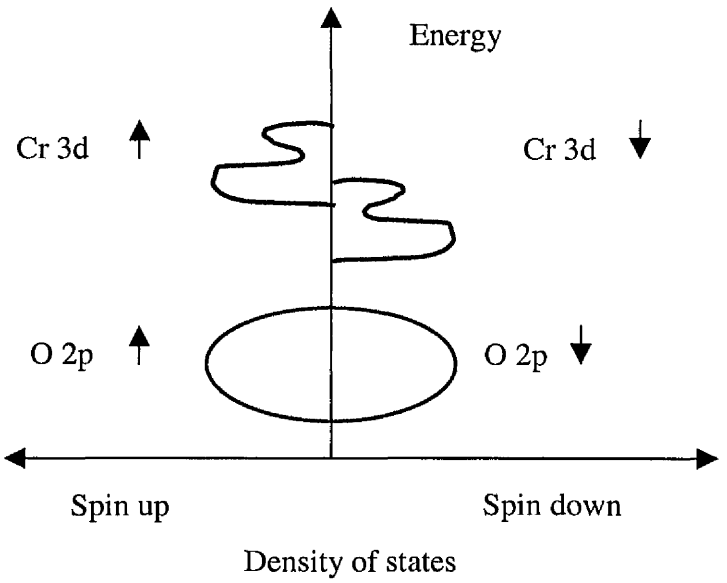

Figure 5.2 *An example of how the band structure may differ between spin up and spin down states when there is magnetic ordering present. The oxygen 2p orbitals are unaffected but the spin up and spin down Cr 3d orbitals split into different bands.*

It is known that magnesium chromite is antiferromagnetic below 16K (Blasse and Fast, 1962). Indeed it is likely that all the chromites show some form of magnetic coupling. Moriwake *et al*, (2000) have considered magnetic effects in magnesium chromite while Freyria Fava *et al* (1997) have considered them in manganese chromite. Both sets of work show significant effects on the electronic structure resulting from the magnetic coupling.

In the ferrites the iron spins on the octahedral sites are aligned in the same direction. The spins on the tetrahedral sites are also aligned, but in the opposite direction to that on the octahedral sites. Therefore a completely inverse ferrite is antiferromagnetic, since equal

numbers of opposite spins are present on each type of site. In a similar way partially inverse ferrites are ferrimagnetic, and completely normal ferrites are ferromagnetic. Pénicaud *et al* (1992) have shown that there are significant differences to the spin up and spin down contributions to the band structure for cobalt ferrite and nickel ferrite. Therefore, for these compounds, magnetic coupling is expected to influence the ELNES.

Figure 5.3 shows a simple diagram of how the d-electrons are distributed between the t_{2g} and e_g levels for an octahedrally co-ordinated chromium (III) ion and an iron (III) ion in tetrahedral co-ordination. It will be shown in section 5.4.1 that the 3d orbitals of the tetrahedral site iron dominate the hybridisation with the O 2p orbitals, rather than the 3d orbitals of the octahedral site iron, so only the tetrahedral case will be considered here. It is also known that the electrons of the iron (III) ion will form a high-spin configuration from measurement of the magnetic moment in ferrites.

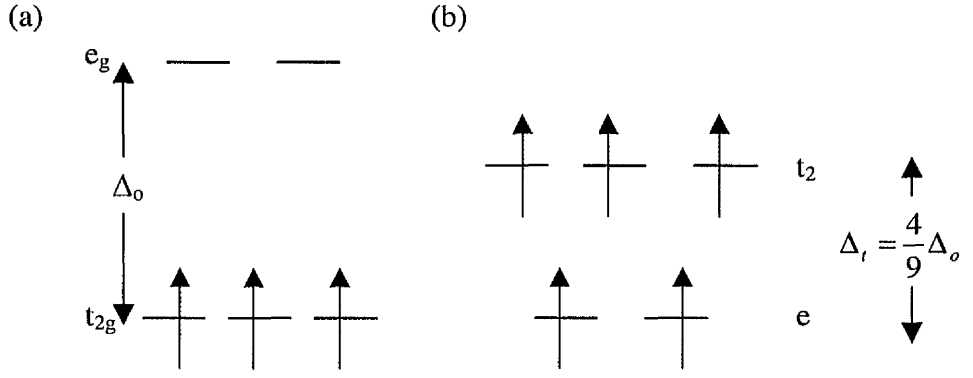

Figure 5.3 *The distribution of electrons in the d-orbitals for (a) an octahedrally Cr (III) ion and (b) a high spin Fe(III) ion which is tetrahedrally co-ordinated.*

For the chromium (III) ion three types of site are available to hybridise with the oxygen orbitals; namely spin-down sites in the t_{2g} level and spin up and spin down sites in the e_g level. However, the spin up sites in the e level are already occupied for the tetrahedrally co-ordinated iron (III) ion, so that only two types of site are available to take part in hybridisation, rather than the three in the case of the chromium (III) ion. The ligand field splitting energy between the t_2 and e levels for a tetrahedrally co-ordinated ion is only 4/9 times that of the equivalent ion in octahedral co-ordination. Therefore the absence of one type of site in the ferrites and the decrease in energy difference between the t_2 and e levels for the tetrahedrally co-ordinated iron ion could lead to the limited features observed in the ferrite spectra compared to the chromites.

5.2.4 Peak energies

Table 5.2 gives the energies of peak D and the energy of the point of steepest gradient prior to the shoulder D* for the aluminates. The latter energy will be referred to as the threshold energy in the aluminate spectra. It is clear that the energies of peak D are within ~1eV of each other, as are the threshold energies, showing that these parameters are little affected by the nature of the metal (II) cation.

The energies of peaks A and D and the energy of the point of steepest gradient on the low energy side of peak A for the chromites are also listed in table 5.2. The latter will be referred to as the threshold energy for the chromites. With the exception of copper chromite, the relative positions of these features are the same to less than 0.1 eV whichever A^{2+} ion is present. In the copper chromite, the separation of peaks A and D is ~0.5 eV

greater than in the other compounds. The absolute energies of these features only vary by ~1 eV as the A^{2+} ion changes.

Compound	Energy of peak A (eV)	Energy of peak D (eV)	Energy of peak W (eV)	Threshold energy (eV)
$MgCr_2O_4$	531.3	541.2	-	530.8
$CoCr_2O_4$	532.1	542.0	-	531.5
$NiCr_2O_4$	532.6	542.5	-	532.0
$CuCr_2O_4$	532.5	543.0	-	531.8
$ZnCr_2O_4$	531.8	541.7	-	531.2
$MgAl_2O_4$	-	540.5	-	535.5
$NiAl_2O_4$	-	541.5	-	535.8
$ZnAl_2O_4$	-	540.6	-	534.7
$MgFe_2O_4$	-	540.0	529.9	528.8
$CoFe_2O_4$	-	540.6	530.3	529.4
$NiFe_2O_4$	-	541.4	530.9	530.0
$ZnFe_2O_4$	-	540.7	530.6, 531.7	529.9

Table 5.2 *The energies of the edge threshold and various features in the fine structure. The standard error in the energies is ±0.2eV.*

The energies for similar features in the ferrites are also quoted in Table 5.2. In the case of the ferrites the edge onset is defined as the point of steepest gradient on the low energy side of peak W. Since peak W is split in the zinc ferrite spectrum the energies of the two peaks have been quoted in this case, since it is difficult to attain the absolute energy of this peak

without the splitting. The absolute energies of the features vary by a slightly larger range in the ferrites than in the aluminates and chromites, but the spread is less than 1.5eV. The energy separation between peak W and peak D increases by 0.2eV when cobalt is substituted for magnesium, and by a further 0.2eV when nickel is substituted for cobalt. However, the standard error in the peak energies is 0.2eV so it is not clear if this trend is real.

The separation between the threshold and peak D is considerably lower in zinc ferrite than in the other ferrites. However, the difference in lattice parameter between zinc ferrite and the other ferrites has to be considered to fairly compare the energy difference between the edge onset and peak D in these compounds. The energy difference is related to the lattice parameter by the $1/R^2$ rule (de Groot, 1994), which states that

$$\Delta E \times R^2 = constant \tag{5.1}$$

where ΔE is the energy separation between the threshold energy and feature of interest and R is the distance between the absorbing atoms and its nearest neighbour. Since the distance to the nearest neighbour depends on the size of the unit cell, Equation 5.1 can be rewritten as

$$\Delta E \times a^2 = constant \tag{5.2}$$

where a is the lattice parameter. Table 4.2 shows that the lattice parameter for zinc ferrite is significantly higher than that of the other ferrites. If the lattice parameter and energy separation for cobalt ferrite are considered to calculate the constant in Equation 5.2, the modified energy separation between these two features for zinc ferrite is now 11.09eV. This new value is very close to the 11.1eV separation in magnesium ferrite. However, lattice parameter effects cannot explain the trend observed in the inverse ferrites that the

separation of peaks W and D increases by 0.2eV as the magnesium ion is substituted for cobalt, and by a further 0.2eV as cobalt is substituted by nickel, if this trend is real. This is because there is no correlation between the changes in lattice parameter and changes in energies in those cases. Such a big change in lattice parameter is not observed within the aluminate or chromite groups, so does not have to be considered for these compounds, when comparing the energies of similar features.

Table 5.2 also allows a comparison between the three types of spinel. This shows that the mean threshold energy is ~4eV and ~5eV lower for the chromites and ferrites respectively than for the aluminates, while the mean energy of peak D in the chromites is ~1eV higher than for the aluminates and ferrites. It is interesting to note that the energies of peak D in zinc aluminate and magnesium aluminate are similar, whereas the peaks in nickel aluminate are observed at higher energies, as shown in figure 5.4. Likewise, this figure shows the energies of peaks A and D in the magnesium chromite and zinc chromite spectra occur at similar energies but the same features are at higher energies for cobalt, nickel and copper chromite. For both the chromites and aluminates, substitution of the magnesium or zinc ion by a transition metal ion with partially filled d-orbitals results in an increase in the peak energies. There is unlikely to be a residual lattice parameter effect in the aluminates and chromites since the lattice parameters for all the spinels within each group are very close. The trend is not observed in the ferrites however. This may be an indication that this trend is complicated by the varying degrees of inversion in these materials.

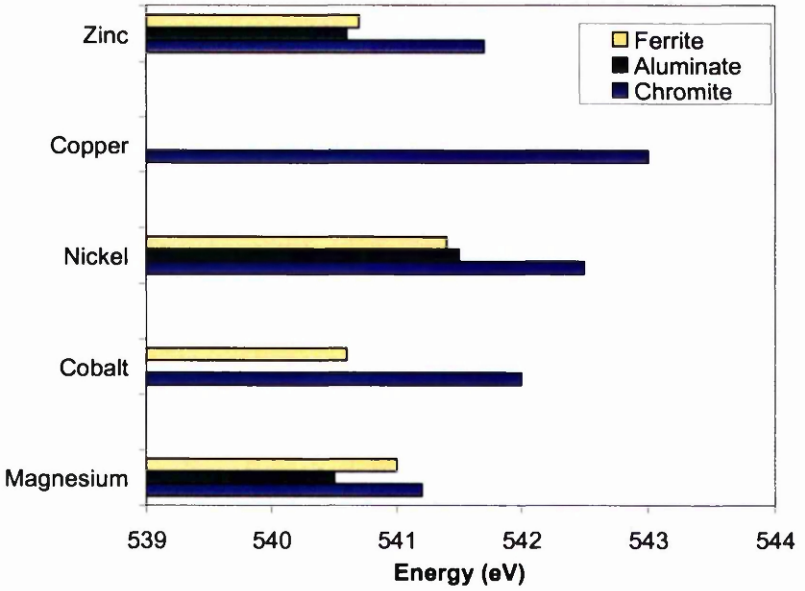

Figure 5.4 *For both the aluminate and chromite series, the energy of peak D is highest when the second metal ion has partially filled d-orbitals.*

5.3 Comparison of the oxygen K-edges from the aluminates

5.3.1 General observations

The comparison between zinc aluminate and magnesium aluminate is complicated by the fact that magnesium aluminate is partially inverse, as shown in table 4.2. Peak D is ~0.5 eV closer to the threshold in magnesium aluminate than in zinc aluminate but, as in the chromites, the shoulder D* is stronger in the magnesium compound. Peak E is split in the zinc compound but the mean energy is close to that in the magnesium compound. There is no pre-peak in the case of zinc aluminate but a very weak pre-peak can be seen in figure 5.1 for the magnesium aluminate. This is considered further in section 5.3.2.

Nickel aluminate is fully inverse. Its oxygen K-edge shows a pre-peak X in addition to the shoulder D*. The intensity of the pre-peak is independent of the electron dose and does not vary from particle to particle. The intensity of D* is greater than that in zinc aluminate and very similar to that in magnesium aluminate. It is thought that the pre-peak X in the nickel aluminate spectrum could be a signature for an inverse spinel. This assignment will be discussed in section 5.3.2.

Apart from the absence of features A, B and C, the main observation is that the features D and D* are more intense relative to the atomic continuum in the aluminates than in the chromites. They are also wider in the aluminates by ~3 eV and, as noted in (a), are lower in energy by ~1eV.

5.3.2 Effect of inversion on the ELNES

A small pre-peak, labelled X, has been observed for all oxygen K-edge spectra recorded from nickel aluminate. A similar pre-peak has also been observed for some grains of magnesium aluminate. Figure 5.5 shows the oxygen K-edge spectra recorded from three different magnesium aluminate particles. It is clear that the intensity of the pre-peak in magnesium aluminate varies from particle to particle but is generally weak.

Previous calculations predict a pre-peak of this type for fully inverse magnesium aluminate (Köstlmeier *et al*, 1999, van Benthem and Kohl, 2000). In the work of van Benthem and Kohl, the shoulder, labelled D* in this paper, decreases in intensity and moves to lower energy, eventually becoming a separate peak as the degree of inversion increases. The

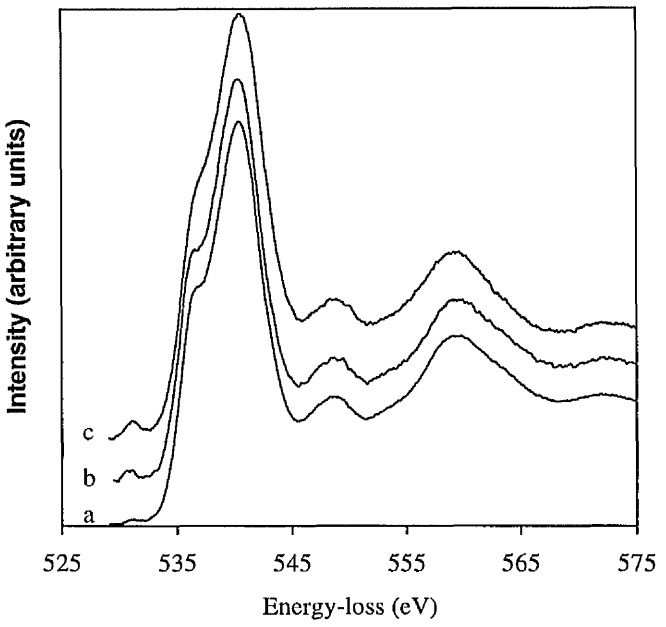

Figure 5.5 *The variation in pre-peak intensity in various grains of magnesium aluminate. The pre-peak is very weak in grain (a), but is clearly observed in grains (b) and (c).*

work of Köstlmeier *et al.* predicts a distinct pre-peak for a completely inverse magnesium aluminate spinel, which is not predicted, or observed, in the normal case.

A more detailed examination of the behaviour of the pre-peak in the experimental data from magnesium aluminate shows that its intensity is independent of electron dose but varies from particle to particle, as shown in figure 5.5. This is in contrast to copper chromite and nickel aluminate where the intensity of the pre-peak does not vary from particle to particle.

Weak pre-peaks are often associated with ion or electron beam damage effects. Here, the specimen preparation does not involve ion beam thinning so the former can be ruled out. As shown in figure 5.1, a pre-peak has been observed in the oxygen K-edges from magnesium aluminate, nickel aluminate and copper chromite. In the latter two of these

three compounds the intensity is independent of which randomly oriented particle the data comes from. In the first, the intensity varies from particle to particle. In five related aluminates and chromites no pre-peak is observed. In no case does the intensity of the pre-peak vary with electron dose. Thus electron beam damage can also be ruled out as the cause of these pre-peaks.

The fact that the intensity of the pre-peak is independent of which randomly oriented particle the data is taken from in two cases also shows that orientation effects are not important with the experimental conditions used. The work of van Benthem and Kohl (2000) predicts that orientation effects would not be expected to have an influence on the intensity of this peak.

The homogeneity of the magnesium aluminate sample has been confirmed by EDX measurements, so that the variation of the pre-peak intensity from particle to particle is not due to variations in composition. Therefore, the pre-peak X has been tentatively assigned as a fingerprint for partial inversion. The range in intensities of this peak suggests that the degree of inversion is not constant throughout the sample of magnesium aluminate. The pre-peak observed in the nickel aluminate spectrum could be the result of inversion. However, it could also be the result of the small number of vacant d-states introduced by the Ni^{2+} ions and further work is required for the correct assignment of this feature.

5.4 Comparison of the oxygen K-edges from the ferrites

5.4.1 General observations

The comparison of the ferrite spectra is complicated by the fact that zinc ferrite is completely normal and the other ferrites are highly inverse, as shown in table 4.2. There are also significant variations between the lattice parameter (1%) and oxygen parameter (2%) in these compounds. As discussed in section 5.2.4 the separation between features W and D, and between the threshold and peak D in the inverse ferrite spectra increase as the metal (II) ion is replaced by one with increasingly full d-orbitals.

The main difference between the ELNES for the normal and inverse ferrites is the splitting of peak W in the zinc ferrite spectrum. Pong *et al* (1996) have studied zinc ferrite and nickel ferrite by X-ray absorption spectroscopy and observed a similar splitting in zinc ferrite but not in nickel ferrite. They have compared their experimental data to spectra simulated using the first-principles spin-unrestricted pseudofunction method and have assigned peak W in zinc ferrite to transitions to states created by the hybridisation of oxygen 2p and octahedrally co-ordinated iron 3d states. In particular, the splitting in peak W results from the hybridisation of the oxygen 2p orbitals with the iron t_{2g} and e_g orbitals.

The interpretation for zinc ferrite is straightforward, given that the iron (III) ions in the octahedral sites are the only metal ions which have 3d orbitals suitable to mix with the oxygen 2p orbitals. In nickel ferrite the situation is more complicated since there are three types of 3d orbital available for hybridisation; namely octahedrally co-ordinated iron (III)

orbitals, tetrahedrally co-ordinated iron (III) orbitals and octahedrally co-ordinated nickel (II) orbitals. Pong *et al* (1996) have considered the probability of hybridisation involving each of these types of orbitals according to the method of Harrison (1980). Harrison has shown that the hybridisation coupling constant, V_{pd}^2 is proportional to (r_d^3/d^7) where r_d is known as the d-state radius, and is a length characteristic of the atom, and d is the bond length from the transition metal ion to the oxygen ion.

Table 5.3 lists the metal-oxygen bond lengths and coupling constants for the three types of hybridisation possible for the three inverse ferrites. It is clear that the tetrahedrally co-ordinated iron (III) ions have the highest hybridisation probability, so feature W will be dominated by transitions to states created by the mixing of tetrahedral iron (III) ion 3d orbitals and O 2p orbitals. In contrast to the two sharp peaks observed in the octahedral site iron 3d DOS in zinc ferrite, the calculations of Pong *et al* for nickel ferrite show broadening of the octahedral site iron 3d band, and a broad featureless band for the tetrahedral site iron 3d band. This explains why the splitting of peak W is not observed for nickel ferrite.

They have also shown that the octahedral site nickel 3d states have a relatively smaller DOS above the threshold region in comparison with the iron sites. The small contribution of the nickel (II) ion to the oxygen p-projected DOS, and the fact that the highest probability for hybridisation is between tetrahedral iron 3d states and oxygen 2p states, explains why there is little change in the ELNES when the metal (II) ion is substituted in the inverse ferrites,

Compound	Metal – oxygen bond length (Å)		p-d coupling constant (x 10^{-3})		
	Tetrahedra site	Octahedral site	Iron in tetrahedral site	Iron in octahedral site	M(II) ion in octahedral site
$MgFe_2O_4$	1.9049	2.0443	5.63	3.431	-
$CoFe_2O_4$	1.9090	2.04448	5.54	3.429	2.94
$NiFe_2O_4$	1.9822	2.03861	5.99	3.50	2.45

Table 5.3 *The p-d coupling constant between the various types of metal sites and the oxygen 2p orbitals in the inverse ferrites.*

5.5 Comparison of the oxygen K-edges from the chromites

5.5.1 General Observations

Table 4.2 shows that all of the chromite samples are essentially normal. Zinc, cobalt and magnesium chromite are cubic, have lattice parameters that are within 0.2% of each other and also have oxygen parameters that are within 0.05% of each other. Assuming that the nominal number of vacant d states taking part in the hybridisation is the controlling factor, magnesium and zinc chromite should have very similar edges shapes because they have the same number of vacant d states. Figure 5.1 shows this to be the case. Relative to the threshold, peaks A, B, D and E and shoulder D* occur at the same energy in each compound. Peaks A, D and E have similar intensities while peak B is lower and shoulder

D* is higher in magnesium chromite. Peak C is strong and narrow in magnesium chromite but is less intense and is split in zinc chromite.

When the spectra from magnesium and zinc chromite are compared to that from cobalt chromite, where the number of vacant 3d orbitals has increased, relatively little has changed. Features A, B, D*, and E occur at very similar energies. Features A, D and E have similar intensities. D* has a similar intensity to zinc chromite adding weight to the idea that the density of the ion core plays a role. Peak C has moved up slightly in energy and is broader and lower than in the other compounds. In addition, it is clear in figure 5.1 and Table 5.1 that if the A^{2+} ion has empty d states, i.e. Co^{2+}, Ni^{2+}, Cu^{2+}, there is an upward shift in the absolute energies of the features amounting to ~1eV compared to those in the Mg^{2+} or Zn^{2+} containing materials.

Table 5.4 shows a comparison of the pd coupling constant, discussed in section 5.4.1, for the octahedral site Cr(III) ion with the O 2p orbitals, and for the tetrahedral site metal (II) ion with the O 2p orbitals for the case of cobalt chromite. Hybridisation involving the chromium ion is favoured. This fact, combined with the larger number of holes per formula unit in the 3d orbitals due to the chromium ion compared to the other metal ion in each chromite probably explains why substitution of the metal (II) ion has little effect on the ELNES.

In summary, the effect of the variation of the number of d vacancies resulting from the substitution of the A^{2+} ion has relatively little effect on the edge shape. The subtle changes observed will be controlled by the detailed interaction of the 3d states of the two metals

with the 2p states of the oxygen. The origins of the small pre-peak, Y, in the copper chromite spectrum will be discussed in the next section.

Compound	Metal – oxygen bond length (Å)		pd coupling constant (x 10^{-3})	
	Tetrahedral site	Octahedral site	Chromium in octahedral site	M(II) ion in tetrahedral site
$CoCr_2O_4$	1.9730	1.9903	5.89	3.77

Table 5.4 *p-d coupling constants for tetrahedral site cobalt ions and octahedral site chromium ions with oxygen in cobalt chromite, illustrating the dominance of the chromium ions in hybridisation.*

5.5.2 Distortions from cubic to tetragonal symmetry

Both the nickel and copper chromites undergo a Jahn-Teller distortion to give tetragonal structures. In terms of the pseudo-cubic cell, as opposed to the conventional tetragonal cell specified in table 4.2, the *c/a* ratios are 1.02 and 0.91, respectively. The Jahn-Teller effect is so weak in nickel chromite that the material undergoes a phase transformation to cubic at 320K (Crottaz *et al*, 1997). The shape of the oxygen K-edge from nickel chromite is very similar to that from cobalt chromite (figure 5.1). In figure 5.6 peak A has been aligned for all spectra and on the relative energy-loss scale 0eV has been defined as the energy of peak A. It is clear that peak A extends to lower energy in nickel chromite than in cobalt chromite. The oxygen K-edge from copper chromite differs more significantly in that peak B is less well defined and there is a clear pre-peak Y.

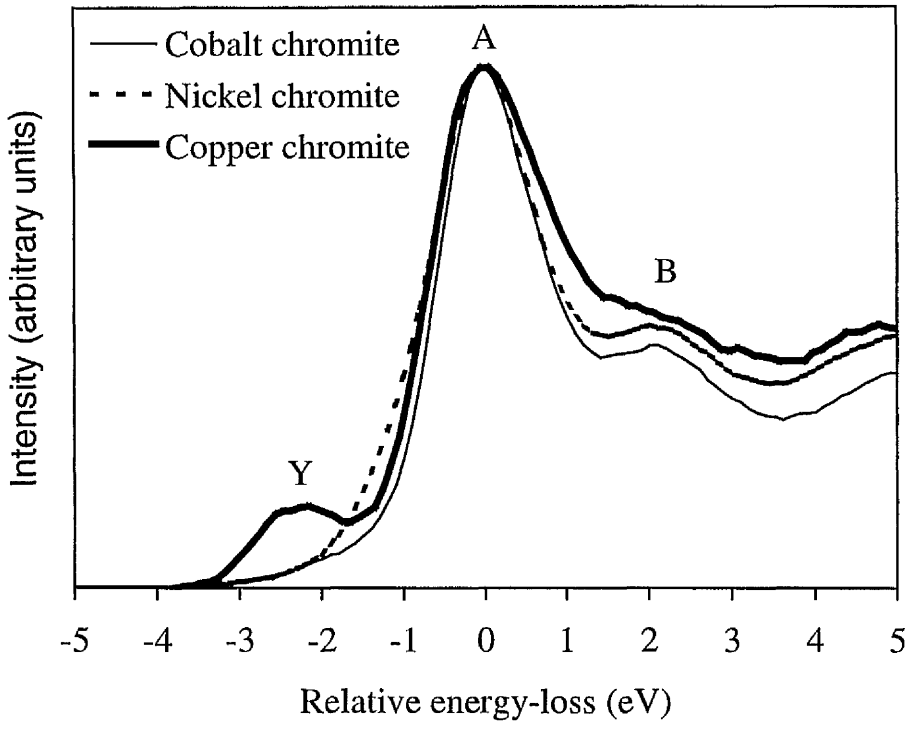

Figure 5.6 *Distortions from cubic symmetry lead to a broadening of the left hand side of the first peak in the nickel chromite edge. When the structure becomes tetragonal , as in copper chromite, a pre-peak is observed.*

This pre-peak has been observed in all of the fifty spectra recorded. This total comprised of approximately seven spectra recorded from each of seven particles studied, as described in section 2.2. Its intensity does not change from particle to particle nor with increasing electron radiation on the same particle. Thus this pre-peak is unlikely to be the result of a beam damage effect. It is also not due to inversion since these compounds are completely normal, as shown in table 4.2. The formation of the low energy tail on peak A in nickel chromite and the pre-peak Y in copper chromite are tentatively interpreted as indicating the degree of tetragonality present, the bigger change in copper chromite being associated with the higher degree of tetragonality.

5.6 Comparison of experimental and simulated spectra

5.6.1 Magnesium aluminate

The first spectrum simulated was that of magnesium aluminate. In the calculations it was assumed that magnesium aluminate was completely normal, since it is difficult to correctly include partial inversion in the calculation. This assumption is justified since there is no major difference between the ELNES for the partially inverse magnesium aluminate and the normal zinc aluminate, apart from the pre-peak in some magnesium aluminate spectra. If the pre-peak is associated with the degree of inversion, then it should be absent in the calculated spectra.

The number and type of ion in each shell included in the calculation is given in table 5.5, and figure 5.7 shows the effect of progressively increasing the number of shells in the cluster. The simulated spectra have been raised in energy by 4.8eV so that the main peaks of the experimental and simulated spectra are aligned. It is clear that, by the time seven shells have been included, the calculation has converged to the accuracy required for comparison with the experimental data, since the inclusion of more shells in the calculation has little further effect on the fine structure simulated. The simulated spectra have been convoluted with a Lorentzian function of 1.2eV full-width at half-maximum (FWHM) to add experimental broadening to the simulated spectra. This value was chosen since it appeared to give the best agreement with the experimental data. This is similar to the work of Kostlmeier *et al.* (1999), who convoluted the simulated spectra with a Gaussian of 1eV FWHM to obtain the best match to experimental data.

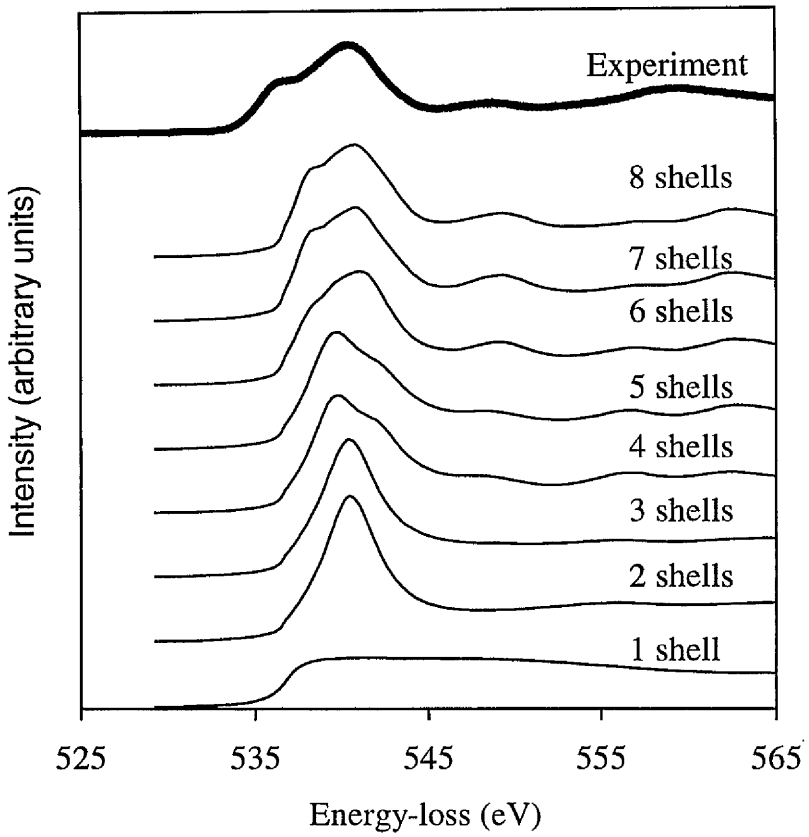

Figure 5.7 *The effect of adding more shells to the cluster used for the multiple scattering calculations for magnesium aluminate, and the comparison to the experimental data when the calculation has converged.*

It can be seen that the fine structure is developed by the addition of shells of oxygen ions, but the addition of shells of metal ions has a negligible effect, showing the fine structure is dominated by the oxygen ions. This agrees with the interpretation of Kostlemeier *et al* (1998), in which a density-functional study assigns the fine structure in the magnesium aluminate oxygen K-edge to transitions to oxygen 2p states, and the surrounding metal ions have little effect on the ELNES. The multiple scattering results are also consistent with work on magnesium oxide, (for example, Rez *et al*, 1995), in which the oxygen ions are considered to be strong scatterers and dominate the multiple scattering.

No. of shells in cluster	No. of atoms in cluster	Type of atom in terminating shell	Cluster radius (Å)		
			$MgAl_2O_4$	$MgCr_2O_4$	$CoCr_2O_4$
1	4	Metal	2.02	1.99	2.00
2	16	Oxygen	2.86	3.23	3.21
3	23	Metal	3.50	3.67	3.66
4	29	Oxygen	4.04	4.38	4.36
5	44	Metal	4.52	4.79	4.78
6	68	Oxygen	4.95	5.27	5.25
7	84	Metal + Oxygen	5.71	5.89	5.89
8	105	Metal	6.06	6.35	6.34

Table 5.5 The atom clusters used in the multiple scattering calculations.

5.6.2 Magnesium chromite and cobalt chromite

The oxygen K-edges for magnesium chromite and cobalt chromite have also been simulated, to investigate the effect of including one and two transition metals in the calculations. These calculations converge when six shells are included in the calculation. Figure 5.8 compares the converged calculations for these compounds to the experimental data and the clusters used are described in table 5.5. The application of 1.2eV broadening, as for the magnesium aluminate case, results in the loss of a lot of the detail in the fine structure. The calculations for the chromites are therefore presented including broadening due to the core hole lifetime but without additional instrumental broadening.

These simulations show additional fine structure compared to the magnesium aluminate case. Three additional peaks in the first 10eV beyond the edge onset, corresponding to the

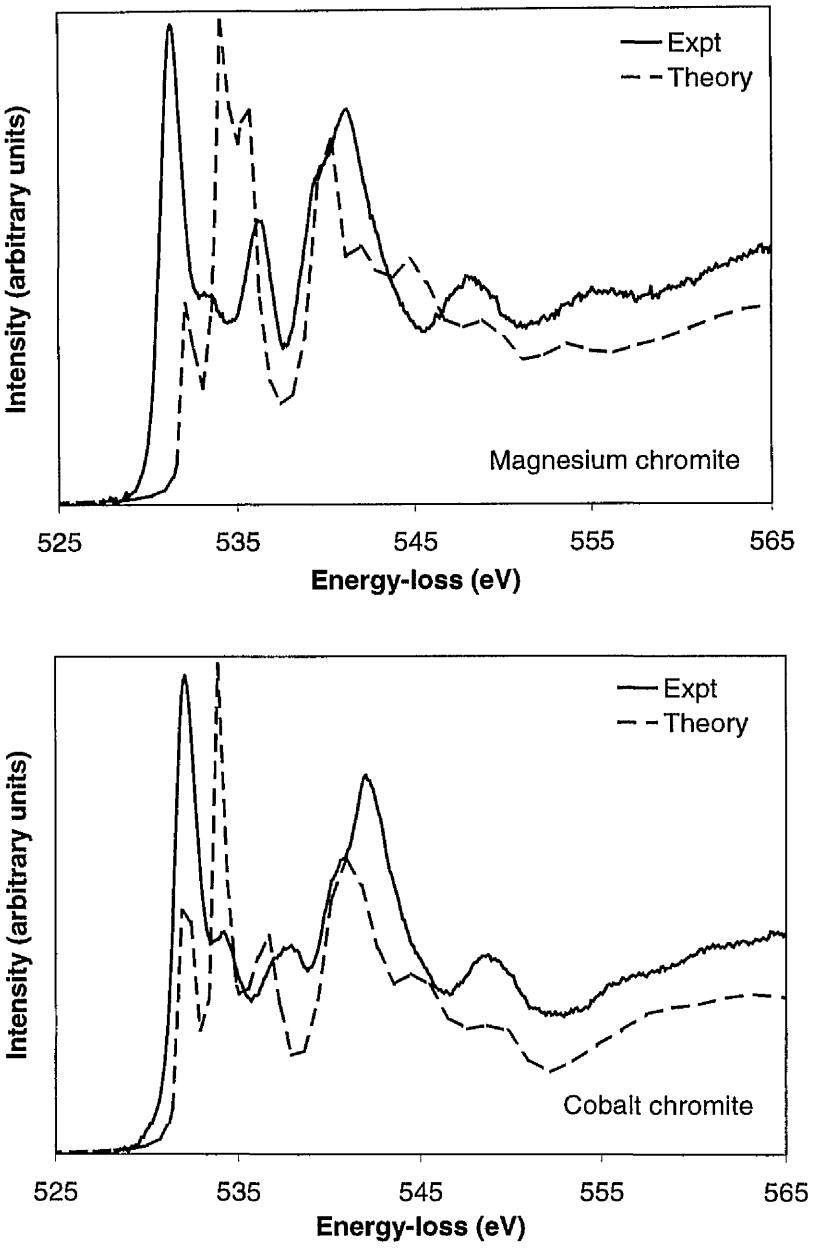

Figure 5.8 *Comparison of the experimental and simulated spectra for magnesium chromite and cobalt chromite.*

peaks due to p-d hybridisation in the experimental data, are present. However, their energies and particularly their intensities are in poor agreement with the experimental data.

The match beyond the first 10eV, where the features D and E are present in the experimental spectrum, is also not as good as in the magnesium aluminate case.

Unlike in the magnesium aluminate case, the detailed shape of the peak at the threshold is sensitive to the exact position of the Fermi level for these compounds. Shifting the position of the Fermi level by the 1eV uncertainty expected from the calculation changes the relative intensity of the first peak but the agreement with the experimental data remains less than satisfactory. As a check, calculations were also performed without the inclusion of the core hole. While this changes the height of the first peak, the agreement remains poor. As for the chromites, the agreement between the experimental data and FEFF8 simulations for magnesium ferrite is also poor.

5.6.3 Comparison of multiple scattering and pseudopotential calculations

It is not clear why there is such poor agreement between the FEFF8 simulations and the experimental data. Figure 5.9 compares the experimental data, FEFF8 simulations and preliminary calculations using a pseudopotential method (Elsässer, 2000) for the oxygen K-edge in magnesium aluminate and magnesium chromite. Details of the pseudopotential method used have been published previously (see for example, Köstlemeier *et al*, 1999). As with the results obtained using FEFF8, the simulations using the pseudopotential method show marked differences between experiment and theory for magnesium chromite while giving reasonable agreement for magnesium aluminate. As with the FEFF8 simulation, the pseudopotential method also gives poor agreement with the nickel chromite oxygen K-edge ELNES.

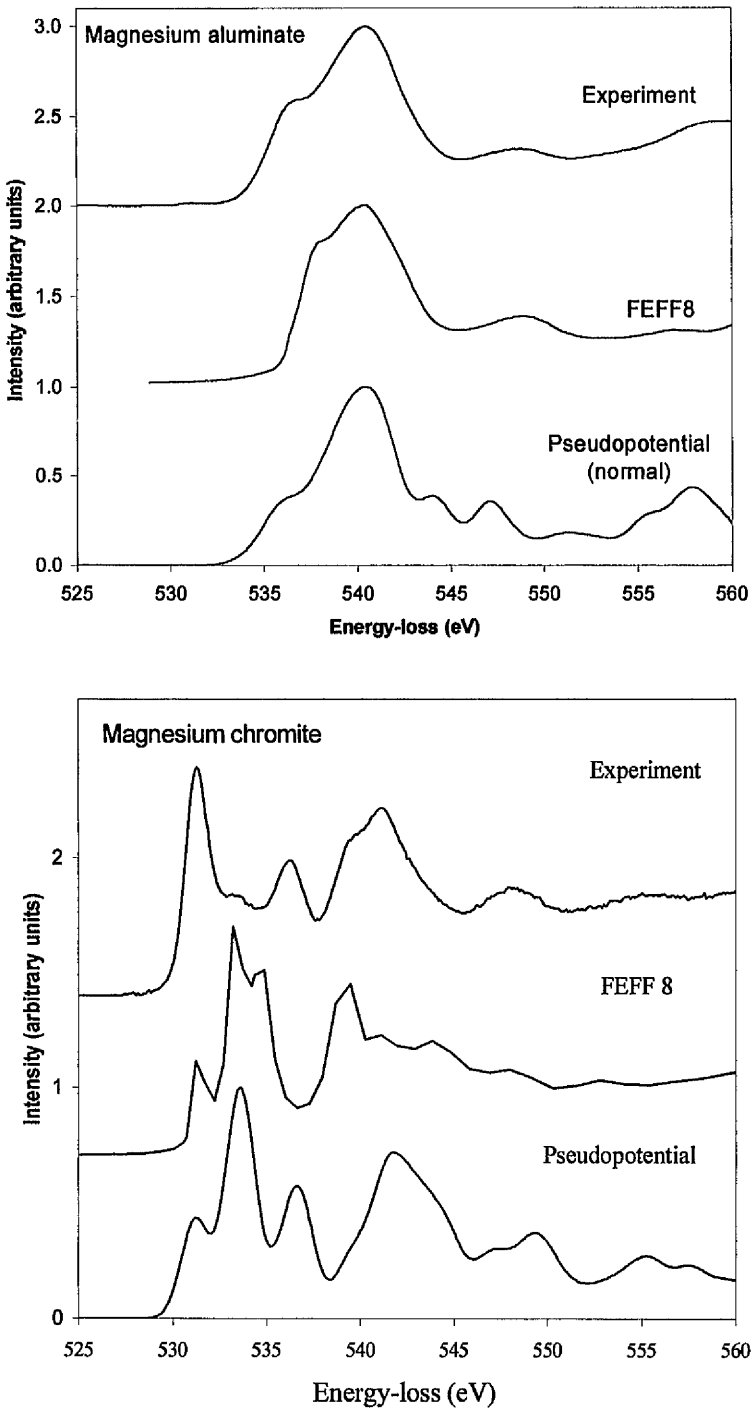

Figure 5.9 *Comparison of the ELNES simulated using FEFF8 and pseudopotential methods, with the experimental data. Both simulation methods reproduce the features in the magnesium aluminate spectrum fairly well, but the agreement is poor from both calculations in the first 10eV beyond the threshold for magnesium chromite.*

The fact that two different calculation schemes give poor agreement with experiment suggests that other factors play a role. One such factor may be the magnetic interactions discussed in section 5.1.3. For the chromium nitride example discussed in section 5.1.3, a local spin density functional calculation with collinear moments based on the known anti-ferromagnetic structure gave better agreement with the experimental edge shape than the equivalent calculation for the non-magnetic phase (Paxton *et al*, 2000). Moreover, the antiferromagnetic state was 336 meV per CrN formula unit lower in energy than the non-magnetic phase. Thus it is not surprising that the band structure of CrN was unaffected over the range of temperature investigated. It has been shown that the electronic structure in the chromites and ferrites is sensitive to the magnetic interactions in these materials (Moriwake *et al*, 2000, Freyria Fava *et al*, 1997 and Pénicaud *et al*, 1992). Thus detailed calculations taking such effects into account might reflect the observed ELNES more accurately.

5.6.4 Evaluation of the FEFF8 code

The full multiple scattering routine of the FEFF8 program produces simulations that converge in the ELNES region. In the case of magnesium aluminate good agreement is obtained between the experimental and simulated spectra. In the case of the chromites, the calculations reproduce the extra fine structure observed in the experimental spectrum, due to transitions to p-d hybrid states. However, the intensities and peak energies in this region poorly match the experimental data. The inclusion of the core hole, and of shifting the Fermi level in the calculation modifies the intensities in this region but does not improve

the agreement with the experimental results. Other effects such as magnetic interactions may have to be included in such calculations for more accurate simulation of the ELNES.

5.7 Summary

The results presented in this chapter provide evidence that the occupation of the d-orbitals of the transition metal ions have a significant influence on the oxygen K-edge ELNES. Common features have been observed in all spectra. However, significant extra fine structure is also present when a transition metal ion is incorporated into the structure, compared to the cases where there are no transition metal ions. This has been assigned to the transition of core electrons into unoccupied states created by the hybridisation of oxygen p and metal 3d ions.

The amount of extra fine structure observed can be related to the strength of the hybridisation interaction by the p-d coupling constant. This has been used to explain, for example, why little change is observed in the series of chromites and ferrites edges as the second metal ion is substituted. However, although no significant change can be observed, it has been shown that the second metal ion influences the peak positions.

A signature for changes from cubic to tetragonal symmetry has been discussed, although a larger study would be necessary to confirm this theory. A fingerprint for inversion has also been tentatively assigned. It will be shown in Chapter 6 however, that the signature for inversion may be more strongly observed in the metal K edge fine structure.

Comparisons of experimental data with simulations show that different modelling methods can successfully predict the oxygen K-edge fine structure for magnesium aluminate but fail to model this for the chromites and ferrites. It has been suggested that a more sophisticated calculation which considers other factor such as magnetic interactions is required for successful simulations for these compounds.

Chapter 6

The metal L_2, L_3 and K edges in spinel

6.1 The origins of fine structure in transition metal L_2 and L_3-edges

The L_2 and L_3 edges arise from the excitation of 2p core electrons. According to the dipole selection rule 2p electrons can be excited into states which are s- or d-like in character. There is a large overlap between the p and d wavefunctions, and the density of states of the metal 4s band is considerably lower than in the 3d band. Therefore the transition probability to d-like states is much higher than to s-like states. Consequently in 3d transition metal oxides these edges are dominated by intense sharp peaks arising from transitions from the 2p core level to the narrow unoccupied metal 3d states.

Figure 6.1 shows a typical spectrum for the L_2 and L_3 transition metal edges from a transition metal oxide. In this case it is the iron edge from an iron (III) ion in octahedral co-ordination. For such a transition the spectrum is dominated by two sharp

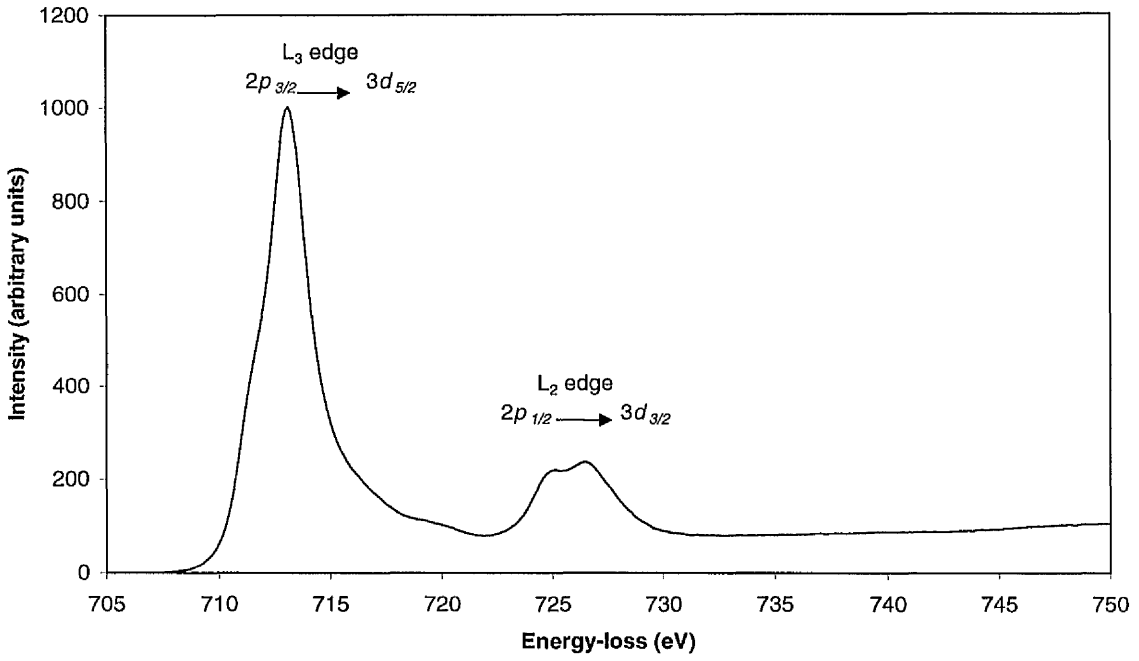

Figure 6.1 The iron L_3 and L_2 edges in magnesium ferrite.

peaks known as white lines. The two peaks are separated by the spin-orbit coupling, which arises from the interaction of the magnetic spin moment of the electron with the magnetic field arising from its orbital motion. The orbital, $\boldsymbol{L}$, and spin, $\boldsymbol{S}$, angular momenta can be combined in various ways. The total angular momentum, $\boldsymbol{J}$, is defined as

$$\boldsymbol{J} = \boldsymbol{L} + \boldsymbol{S} \tag{6.1}$$

Therefore there are states in which $j = l + \frac{1}{2}$ and $j = l - \frac{1}{2}$ according to whether **L** and **S** are parallel or antiparallel respectively. For the 2p states, l=1, so j can therefore have values of $\frac{1}{2}$ or $\frac{3}{2}$. The $2p_{3/2}$ state is at a higher energy than the $2p_{1/2}$ state, so less energy is required to excite a $2p_{3/2}$ electron into the conduction band. The peak at lower energy in the EELS spectrum in figure 6.1 therefore results from transitions from the $2p_{3/2}$ level and is known as the L_3 edge. The L_2 edge at higher energy originates from the transition of $2p_{1/2}$ electrons.

The one-electron approximation, which is the basis of many methods used to model the fine structure, fails to explain many features of the transition metal L_2 and L_3 edges, such as the ratio of intensities of the L_3 and L_2 peaks, and the width of the peaks. This is because of the strong overlap between 2p core orbitals and partially filled 3d valence orbitals, and subsequent electron correlation effects. For accurate modelling of these edges the 2p-3d and 3d-3d Coulomb and exchange interactions and the 2p and 3d spin-orbit interaction must be included in any calculation.

In the case of the transition metal oxides, ligand field effects must also be considered. When a metal ion is octahedrally co-ordinated the five 3d orbitals which are degenerate in the free ion are split into two levels, which have the symmetry representations t_{2g} and e_g. The twofold degenerate e_g state contains orbitals which point directly towards the ligands and the three t_{2g} orbitals point between the ligands. Consequently the electrostatic interactions between the e_g orbitals and the ligands are greater than those of the t_{2g} orbitals and the ligands, so the e_g orbitals are at higher energies. Therefore there are d-states at two different energies which the excited 2p electrons of each spin state can reside in and this results in splitting of each of the main peaks for transitions from each spin state.

In section 6.2 the experimental L_3 and L_2 edges from the transition metals will be presented for all of the compounds whose oxygen K-edges were discussed in chapter 5. This experimental data will be compared to the L_3 and L_2 absorption spectra simulated by van der Laan and Kirkman (1992). They simulated these edges for the first-row transition metal ions in tetrahedral and octahedral crystal field symmetry and have included the effects of electrostatic and spin-orbit interactions. Their study also considered the effect of the magnitude of the crystal field splitting, ranging from 0 to

3eV, on the fine structure. Since no estimate of the crystal field splitting in spinels was found in the literature, the values for the bivalent and trivalent transition metal ions of interest surrounded by water ligands (Schläfer and Gliemann, 1969) were used as approximate values.

In the work of van der Laan and Kirkmann (1992), the spectra have been broadened with Gaussians whose FWHM ranges from 0.095eV to 0.279eV to match their instrumental resolution. The simulated spectra from their study presented here have been convoluted with a Gaussian of appropriate width, such that the spectra have been broadened by a Gaussian of 0.8eV FWHM in total. The value of 0.8eV was chosen since this appeared to give the best match with experimental data.

6.2 Transition metal L_2 and L_3 edges – general observations

6.2.1 Chromium

The chromium L_3 edge onset is at ~574eV. This is only ~40eV higher in energy than the oxygen K-edge, so the chromium edge sits on top of the tail of the oxygen K-edge, as shown in figure 6.2. When acquiring ELNES data at a dispersion of 0.1eV/channel the chromium L_2 and L_3 edges were recorded immediately after an oxygen K-edge, and the spectra spliced together. This meant that the background could be modelled using a window before the oxygen K-edge, and then extrapolated to remove the background from the chromium edges. A disadvantage of this method is that any small errors in the background fitting at the oxygen K-edge onset are magnified for the chromium edges.

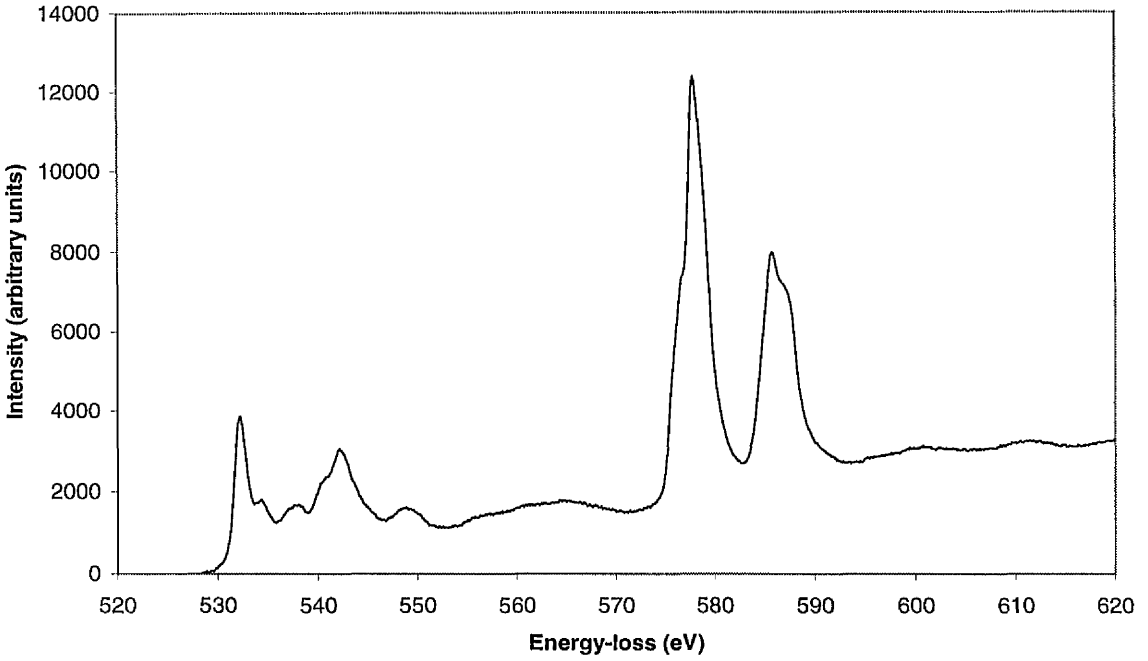

Figure 6.2 *The overlap of the oxygen K and chromium L_2 and L_3 edges from cobalt chromite.*

An attempt to remove the tail of the oxygen K-edge from the chromium L_2 and L_3 edges was made using the oxygen K-edge spectra recorded from the aluminates and ferrites. It was thought that if there was good agreement between the chromite and ferrite or chromite and aluminate spectra in the region of ~565eV, then the tail from the oxygen K-edge in the aluminates or ferrites could be subtracted from the chromium edges. However, there was poor agreement between the oxygen edges of the different compounds in this region so this method was unsuccessful.

The second method used to remove the tails of the oxygen K-edge from the chromium L_2 and L_3 edges was to make use of the atomic cross-section for the oxygen K-edge. The reasoning behind this approach is that there is little difference in the wavefunctions of the core electrons between an individual atom and those in a solid, so an atomic model can be used to indicate the general shape of inner-shell edges. The effect of the

near edge structure is to modify the intensity distribution but the overall intensity remains fairly constant. Therefore an atomic model can be used to calculate the ionisation probability for the oxygen K-edge from the energy threshold, E_{th}, to $E_{th}+\Delta$, where Δ is the energy range above threshold considered, and includes the energy range of the chromium L_2 and L_3 edges. This can be normalised to the total intensity of the experimental edge profile over the energy range from the oxygen K-edge onset to the chromium L_3 edge onset, and subtracted from the experimental spectrum.

The atomic cross-section for the oxygen K-edge was modelled using the Hartree-Slater model using the routine in the EL/P, version 3, program. This model will be described in more detail in section 6.3.2. The intensity of the atomic cross-section was matched to that of the oxygen edge over the range 530eV to 570eV, and the area under the chromium L_2 and L_3 edges was removed from the metal edge. Figure 6.3 shows the

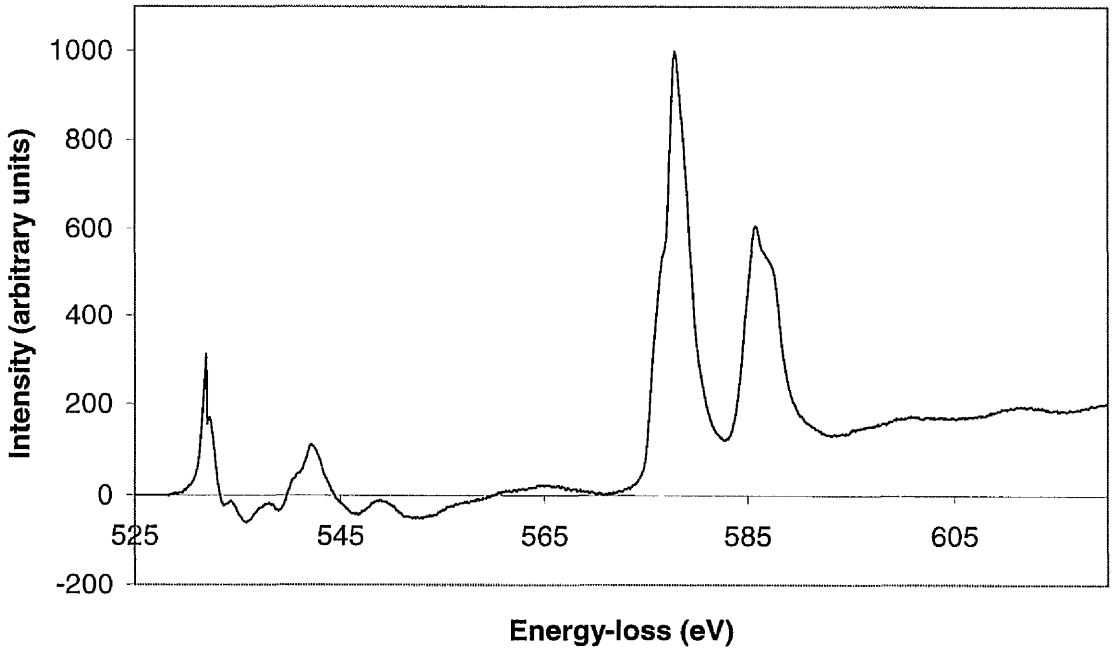

Figure 6.3 *The resultant spectrum for cobalt chromite when the oxygen K-edge is modelled using a partial cross-section model, normalised and subtracted from the experimental spectrum. The residual in the region of the oxygen K-edge oscillates around zero as expected since the fine structure just rearranges the intensity distribution.*

resultant spectrum for the chromium L_2 and L_3 edges from cobalt chromite, and the preceding residual background. It is obvious that the intensity in the region prior to the chromium edge oscillates around zero to some extent, showing there is some success in this method since no large areas of dominantly positive or negative intensity are observed overall. It forms a well-defined procedure that has been repeated on all of the chromium L_2 and L_3 edges in the absence of any better approach. The results are shown in figure 6.4.

The interpretation of the chromium L_3 and L_2 edges is simplified by the fact that all of the chromites are normal, so the chromium (III) ion only occupies octahedral sites. All of the L_3 peaks have a shoulder on the low energy side of the main peak and the L_2 peaks have a high-energy shoulder. This splitting is mainly due to the ligand field effects discussed in section 6.1. It is interesting to note that the shoulders are clearest in the magnesium, cobalt and zinc chromite edges which are cubic compounds, but are less well defined in the case of nickel chromite and copper chromite which are tetragonally distorted. The Jahn-Teller distortion is due to the distribution of the *d*-orbitals in the metal (II) ion and not the chromium (III) ion for each of these compounds, but this shows that this distortion has an effect on the chromium (III) ion site in both cases.

Figure 6.4 also shows the spectrum simulated by van der Laan and Kirkman (1992) for a chromium (III) ion in octahedral symmetry, with a crystal field splitting of 2eV, and 0.8eV experimental broadening. The simulated spectrum has been aligned with the most intense feature of the experimental chromium L_3 edge from zinc chromite. There is good agreement between the experimental and simulated L_3 edge, with both having a shoulder on the low-energy side. The shoulder on the high-energy side of the L_2 edge

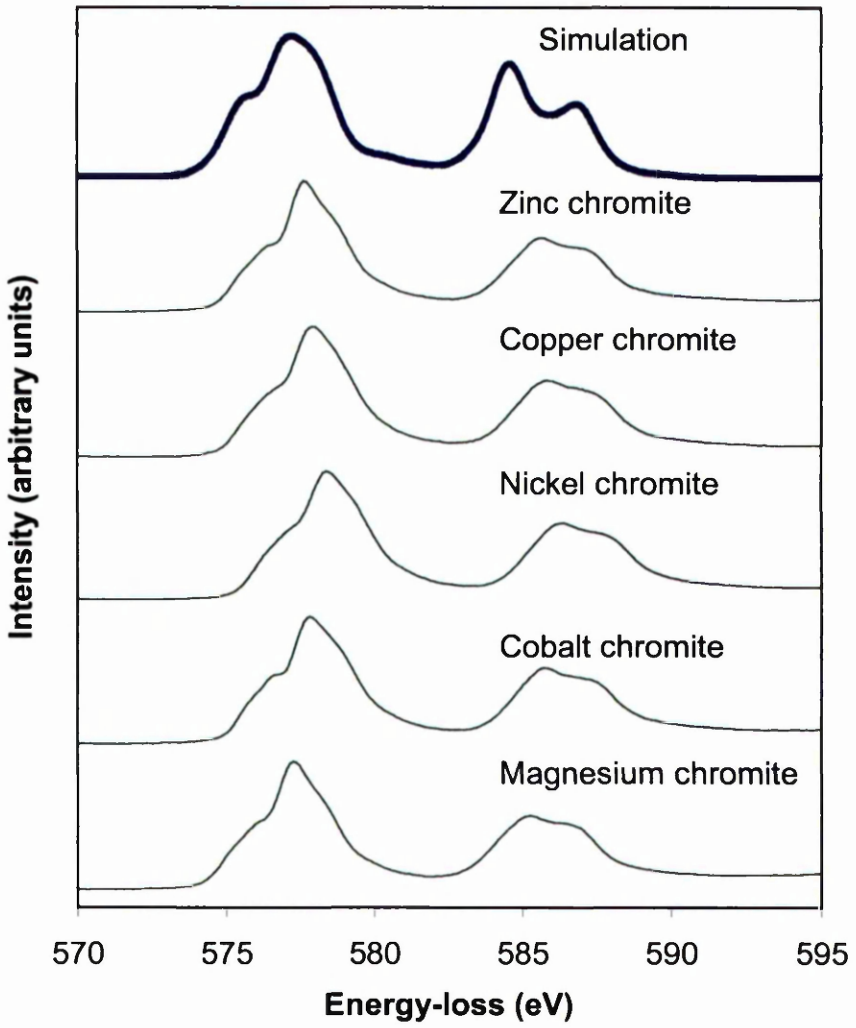

Figure 6.4 *The experimental chromium L_3 and L_2 edges from the five chromite spinels. The tails of the oxygen K-edges have been removed as described in the text. The top spectrum is the simulated spectrum from van der Laan and Kirkman (1992) for an octahedral site chromium ion with a crystal field splitting of 2eV, and 0.8eV experimental broadening.*

in the experimental spectra is also reproduced in the simulation, although the feature is better defined in the simulated spectrum. The simulation reproduces the main features of the experimental edges, suggesting that the experimental data can be explained by considering a model that includes atomic multiplet effects, and that other effects like more distant neighbouring ions have little influence on the fine structure.

Table 6.1 lists the energies of the L_3 and L_2 peaks for all of the chromium edges. The peak energy has been defined as the energy of the most intense point in the edge for all of the compounds. The energies are fairly constant, with a difference of 1.2eV between the highest and lowest values. The separation of the L_3 and L_2 edges is constant throughout the series.

6.2.2 Iron

The experimental and simulated iron L_2 and L_3 edges from the ferrites are shown in figure 6.5. The experimental spectra will be considered first. In all of the experimental spectra the intensity of the L_2 relative to the L_3 peak is smaller than for the chromites. This has been observed for other iron-containing compounds and will be discussed in section 6.3. The L_3 edge has a shoulder on its low-energy side as observed in the chromites, although it is much weaker in the ferrites. This feature is most pronounced in the zinc ferrite spectrum. This may be because zinc ferrite is completely normal, so the iron (III) ion only occupies octahedral sites. The other ferrites are highly inverse, so the iron occupies octahedral and tetrahedral sites. The separation of the t_{2g} and e_g states in a tetrahedrally co-ordinated ion is four ninths of the separation of the levels when the same ion is octahedrally co-ordinated. Transitions to d-states in the octahedrally and tetrahedrally co-ordinated iron ions in the inverse ferrites will result in a superposition of the L_3 and L_2 edges from both types of site and broadening of the peaks observed. The other difference between the chromite and ferrite L_2 and L_3 edges is that the shoulder on the L_2 edge is now on the low energy side of the main peak in the iron edges, and has a higher relative intensity. The energies of the iron L_3 and L_2 edges, given in table 6.1, are constant to within less than 1eV.

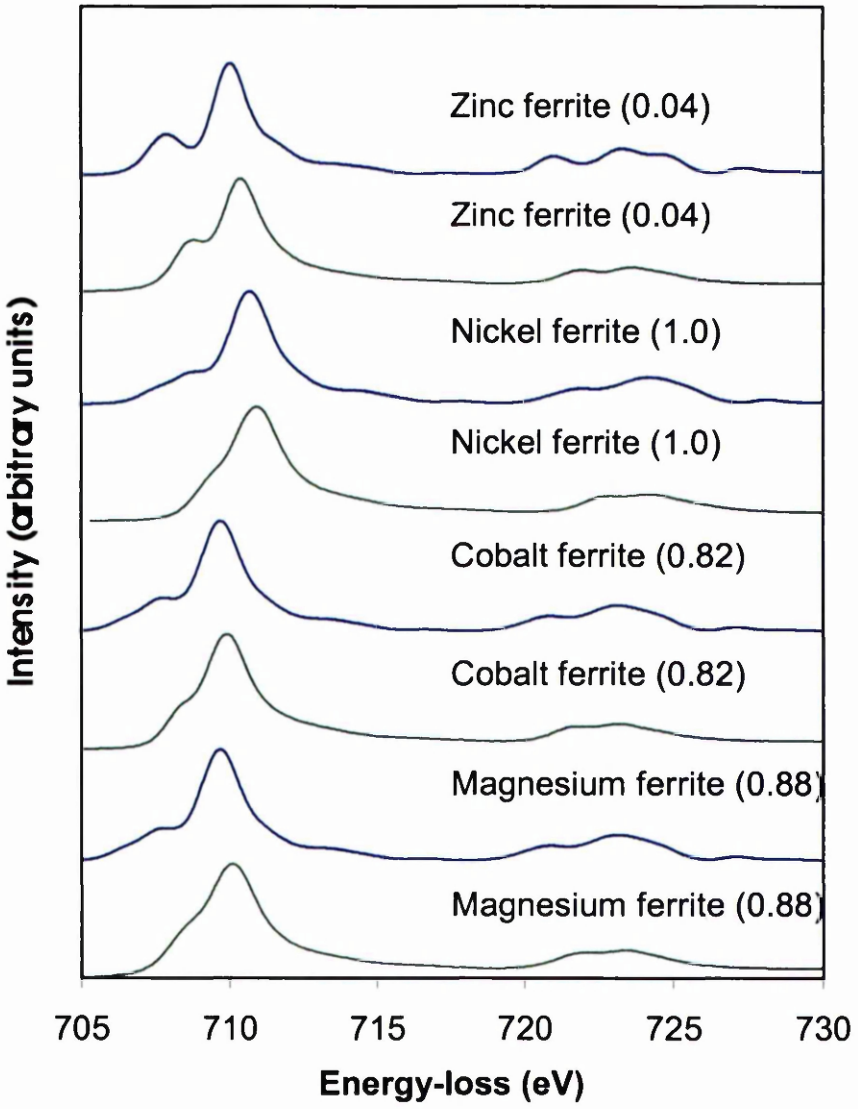

Figure 6.5 *The experimental (green) and simulated (blue) iron L_3 and L_2 edges from the ferrites. The inversion parameter is stated in brackets for each compound.*

Van der Laan and Kirkman (1992) have simulated the L_3 and L_2 absorption edges for the iron (III) ion in tetrahedral and octahedral co-ordination. To investigate if the iron edges from the inverse spinels are direct superpositions of the octahedral and tetrahedral edges, the simulated spectra presented are a weighted sum of the tetrahedral and octahedral edges, according to the inversion parameter of the compound, as listed in table 4.2. As for the simulation of the chromium L_3 and L_2 edges, the simulated

spectra have been broadened by a Gaussian of 0.8eV FWHM in total, and the simulated spectra have been aligned to the highest point in the L_3 edge of the experimental data.

Edge	Compound	Peak energy (eV)		Separation (eV)
		L_3	L_2	
Chromium $L_{2,3}$	$MgCr_2O_4$	577.3	585.3	8.0
	$CoCr_2O_4$	577.8	585.7	7.9
	$NiCr_2O_4$	578.5	586.4	7.9
	$CuCr_2O_4$	578.0	585.9	7.9
	$ZnCr_2O_4$	577.7	585.7	8.0
Iron $L_{2,3}$	$MgFe_2O_4$	710.1	723.5	13.4
	$CoFe_2O_4$	709.9	723.2	13.3
	$NiFe_2O_4$	710.9	724.2	13.3
	$ZnFe_2O_4$	710.4	723.7	13.3
Cobalt $L_{2,3}$	$CoCr_2O_4$	778.8	794.1	15.3
	$CoFe_2O_4$	779.8	795.1	15.3
Nickel $L_{2,3}$	$NiAl_2O_4$	854.3	872.7	18.4
	$NiCr_2O_4$	853.1	871.3	18.2
	$NiFe_2O_4$	854.9	872.1	17.2
Copper $L_{2,3}$	$CuCr_2O_4$	931.0	950.7	19.7

Table 6.1 *Energies and separation of the L_3 and L_2 edges recorded. The energy for each edge is defined as the energy of the most intense point in the edge. The standard error in the energies is ± 0.2eV.*

The top spectrum in figure 6.5 is the simulation for the L_3 and L_2 edges in zinc ferrite. Since this compound is completely normal, the spectrum only comprises of contributions from the edge for the iron (III) ion in octahedral co-ordination. In this case there is good agreement between the experimental and simulated spectra. All of the main features have been reproduced with approximately the correct relative energies and intensities. In the other experimental data the features are less well-defined than in the edges of the normal spinel, but appear to be sharpest in the cobalt

ferrite edge and most diffuse in the nickel ferrite edge. It has already been mentioned that broadening of the features in the inverse spinels may be because the iron (III) ion occupies two types of sites in the inverse structure. The simulated spectra for the inverse ferrites, which are superpositions of the spectra for the iron (III) ion in octahedral and tetrahedral co-ordination in the correct proportions, show slight changes in sharpness of the features, which follow the same trend as the experimental data. However, in all of the inverse cases the features are better defined in the simulated spectra than in the experimental data. This suggests that other factors influence the near-edge structure, which have not been included in the Van der Laan and Kirkman calculations. One possible factor could be the influence of the second nearest neighbours. This will be discussed further when the metal K-edges are considered in section 6.5.

6.2.3 Cobalt

Figure 6.6 shows the experimental cobalt L_2 and L_3 edges from cobalt chromite and cobalt ferrite. As shown in table 4.2, the cobalt (II) ions are tetrahedrally co-ordinated in cobalt chromite, and 80% are octahedrally co-ordinated and the remainder tetrahedrally co-ordinated in cobalt ferrite. For both compounds the splitting of both the L_2 and L_3 edges is much weaker than in the similar chromium and iron edges already discussed. Since this splitting is related to crystal field effects, it may be that the energy resolution is not good enough to observe the splitting in the cobalt chromite case since the ligand field splitting for the tetrahedrally co-ordinated ion is less than half of that for the octahedrally co-ordinated ion. Another explanation can be found by considering that the e and t_{2g} states are full in cobalt chromite and cobalt ferrite respectively. As discussed by van der Laan and Kirman (1992), since there is only one

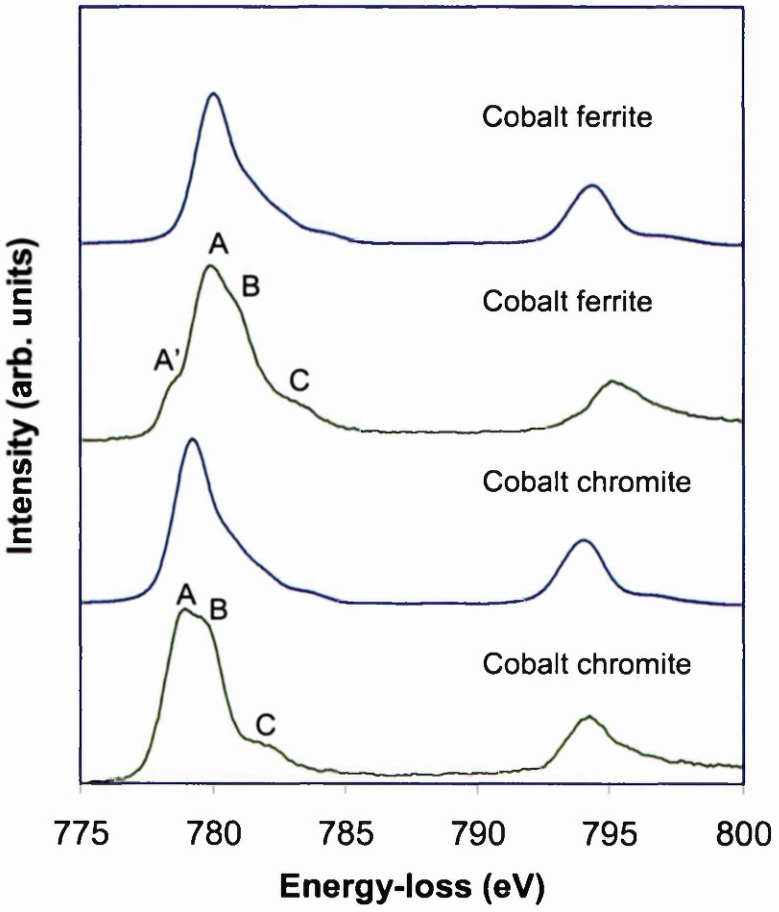

Figure 6.6 *The experimental (green) and simulated (blue) cobalt L_3 and L_2 edges from cobalt chromite and cobalt ferrite.*

type of state vacant in each case, crystal field splitting is not predicted when the ground level *d*-states are full. The energies of the main features in the spectra in Figure 6.6 are given in table 6.1. The relative energy separation between the L_3 and L_2 edges is constant to within experimental error.

Both of the L_3 edges have a shoulder on their high-energy side, labelled C. Three other features, labelled A', A and B can be observed on this edge for cobalt ferrite, but only two features, labelled A and B can be observed in the cobalt chromite case. The extra fine structure observed in the cobalt L_3 edge in cobalt ferrite may be due to the contribution from the cobalt ion in tetrahedral and octahedral environments. For

example, the shoulder A' may be due to transitions to empty t_{2g} states in the tetrahedrally co-ordinated cobalt ions and the main peak to transitions to e_g states in the octahedrally co-ordinated cobalt ions. Further evidence for this assignment is that the low-energy shoulder, A', is at a very similar energy to the main peak, A, in the cobalt chromite L_3 edge, which is due to transition to t_{2g} states in the tetrahedrally co-ordinated cobalt (II) ion.

The L_3 edges both display a broad, low intensity shoulder on their high-energy side which are not well reproduced in the simulations, which will be discussed below. Features of this type have been associated with excitations to orbitals centred on neighbouring atoms which are primarily *p*-like, but exhibit some *d*-like character at the excited atom (Leapman *et al*, 1982). The addition of *p*-like character to the *d*-orbitals results in broadening of the narrow *d*-states.

Figure 6.6 also shows the simulations of van der Laan and Kirkman (1992) for the L_3 and L_2 edges for a cobalt ion in similar local environments to those found in the spinels studied. As for the chromium and iron edges, broadening of 0.8eV has been added in both cases. To best match the immediate surroundings of the cobalt ion in cobalt chromite, which is normal, the simulation for a tetrahedrally co-ordinated cobalt ion, with a ligand field splitting of 1eV is shown. For the case of cobalt ferrite, which is inverse, a cobalt ion in octahedral co-ordination, with a ligand field splitting of 2eV, has been used.

In both cases the general shape and width of the peaks produced by the simulation are in good agreement with the experimental data, but more subtle features which have been recorded are not reproduced. It is interesting to note that there is very little

difference between the simulated spectra for the cobalt ion in octahedral and tetrahedral co-ordination. This suggests that, as for the case of the iron edges, there are other influences on the fine structure, such as second nearest neighbour effects, which are not considered in the calculation.

6.2.4 Nickel

The nickel L_2 and L_3 edges from nickel aluminate, nickel chromite and nickel ferrite are shown in figure 6.7. Splitting of the L_3 edge, of the type associated with crystal field splitting, as observed in the iron and chromium L_3 edges, but not in the cobalt L_3 edges, is not present. It is not expected since, as discussed for the cobalt L_3 and L_2 edges there should be no crystal field effects observed when the ground level t_{2g} or e_g states are full, since there is only one state available that the excited electron can reside in.

The position of the shoulder on the L_2 edge changes for the different compounds. For nickel ferrite, where the nickel (II) ion is octahedrally co-ordinated the shoulder is on the higher energy side of the peak. In nickel chromite the shoulder is on the low-energy side and is less well defined. In nickel aluminate, where the nickel ion mainly occupies octahedral sites, but also occupies tetrahedral sites the peak seems to have split into two equal parts. As for the cobalt and iron edges, the intensity of the L_2 peak relative to the L_3 peak is much lower than in the chromium edges.

The energies of the key features in the spectra are recorded in table 6.1. The spread in the energies of the L_3 peaks is 1.8eV for the three compounds. The lowest energy is for the normal nickel chromite sample, and highest is for inverse nickel ferrite. However, this trend is not observed in the iron L_3 and L_2 edges of the normal and inverse ferrites

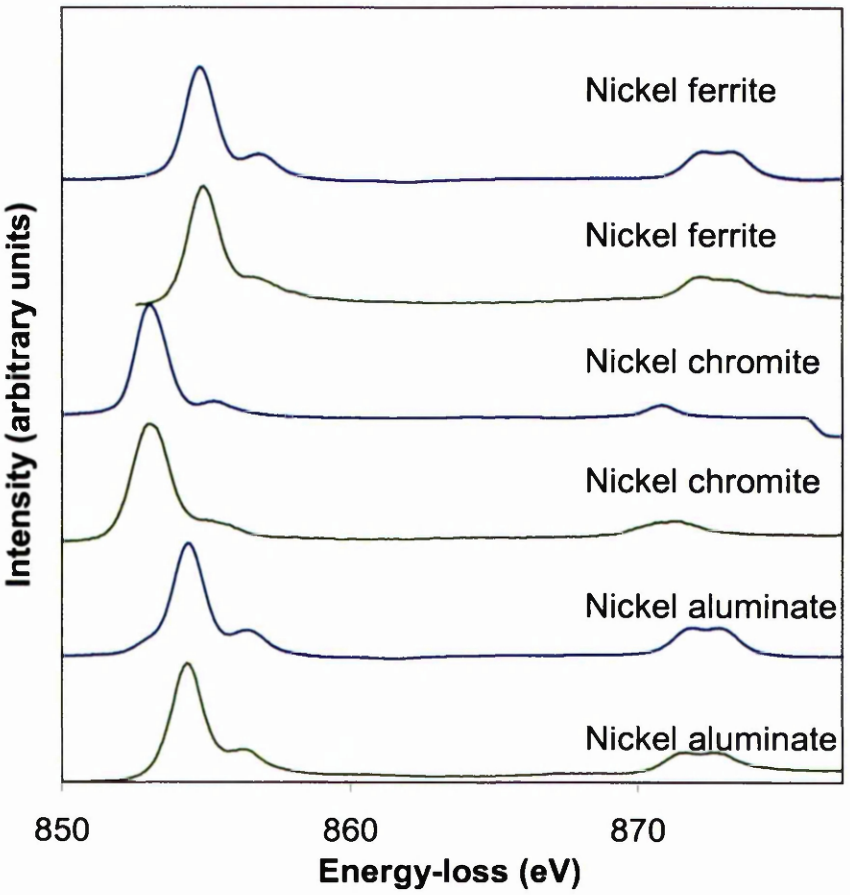

Figure 6.7 *The experimental (green) and simulated (blue) nickel L_3 and L_2 edges from the nickel-containing spinel studied.*

and may be coincidental. The separation of the L_3 and L_2 edges is the same for the nickel aluminate and nickel chromite edges, within experimental error, but is smaller in nickel ferrite. The position of the peaks is defined as the most intense channel in the peak. However, as discussed in the previous paragraph the position of the shoulder in the L_2 edge varies in these three compounds. This will affect the position of the most intense part of the peak and it is therefore unfair to compare the separations of the L_3 and L_2 edges by this method. If a similar position in the L_2 edge for the nickel ferrite is taken as in the other two nickel edges, a more reasonable value of ~18.1eV is obtained.

Figure 6.7 also shows the simulated nickel L_3 and L_2 edges. As before, these edges have been simulated using the data of van der Laan and Lirkman (1993). The data for a

nickel ion in tetrahedral co-ordination with a ligand field splitting of 1eV, and for an octahedrally co-ordinated nickel ion with a ligand field splitting of 2eV were used in the appropriate weightings for each simulation, depending on the degree of inversion of the spinel. Appropriate broadening was added to give an experimental broadening of 0.8eV.

There is fairly good agreement between the experimental and simulated data for all three compounds. The high-energy shoulder on the L_3 peak is broadest in nickel chromite for both the experimental and simulated spectra. However, the simulations fail to reproduce this broadening to the extent required to match the experimental data for nickel chromite and nickel ferrite. In the previous section it was discussed for the cobalt spectra that the broad shoulder may have contributions from transitions to states created by the mixing of oxygen 2p and cobalt 3d states. The nickel edges provide further evidence for this interpretation since the feature is broadest in the nickel chromite and nickel ferrite spectra where there is known to be a significant number of hybrid states, as discussed in section 5.2.2, but is much sharper in nickel aluminate where there is less mixing of the oxygen 2p and metal 3d states. The failure of the simulations to reproduce these features properly is also consistent with this assignment, since hybridisation is not considered in the simulations.

The doublet observed in the L_2 edge in the nickel aluminate and nickel ferrite experimental spectra is also reproduced in the simulation, but is not present in the simulation for nickel chromite, in agreement with the experimental data. This sharpness of the features in this edge follows the same trend for the experimental data and simulations. The reproduction of the small changes observed in the experimental fine structure suggests that these changes are due to atomic effects.

6.2.5 Copper

Figure 6.8 shows the copper L_2 and L_3 edges from copper chromite. This is the only copper-containing compound so there are no other copper L_3 and L_2 edges for comparison. The counting statistics are poorer than for the other metal L_3 and L_2 edges. This has also been observed by Leapman *et al* (1982) in their study of binary oxides, and is due to decreasing cross section with increasing energy loss. The crystal field splitting observed for some of the other metal edges is not observed in either of the L_3 or L_2 peaks. This is consistent with the idea that no crystal field splitting is observed in either peak when the t_{2g} or e_g ground level is completely occupied. However, the small crystal field splitting for the tetrahedrally co-ordinate copper (II) ion would probably

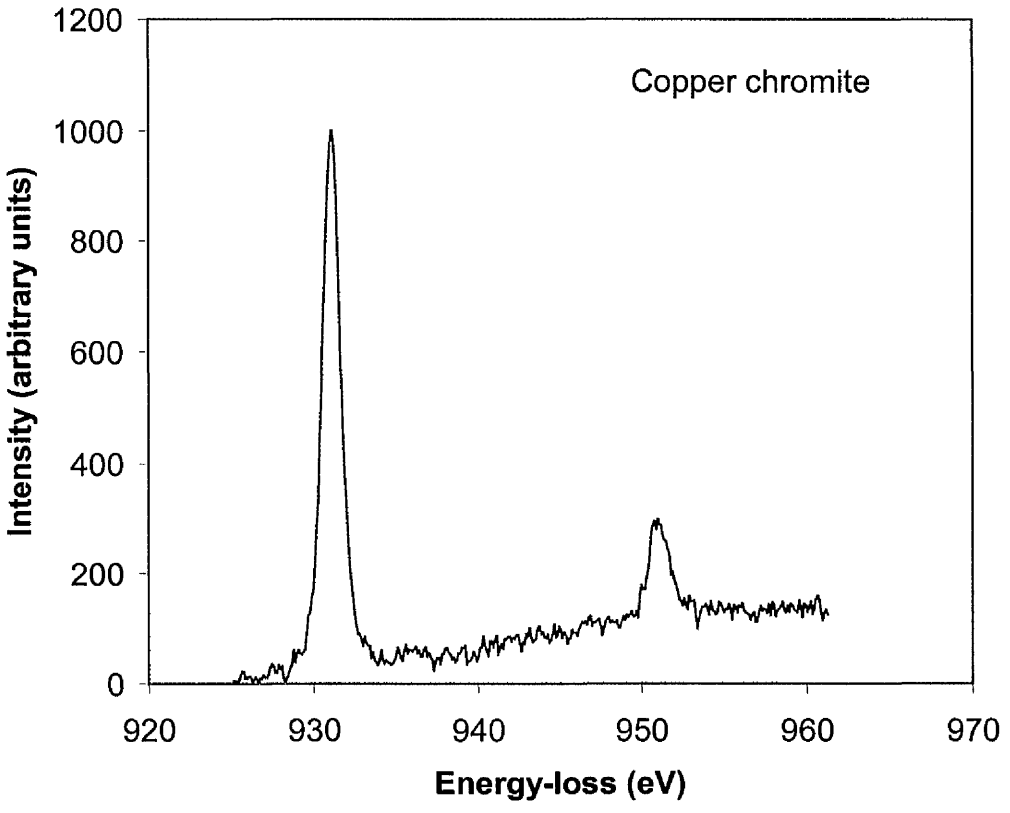

Figure 6.8 The copper L_3 and L_2 edges from copper chromite.

not be resolvable, even if it were present. There is also a weak shoulder on the high-energy side of the main peak in the L_3 edge. This is similar but weaker to that observed in the cobalt and nickel L_3 edges. This shoulder may have contributions from transitions to states created by hybridisation of oxygen p and metal d states. It would be expected that this shoulder would be less intense in the copper case since the copper (II) ion has less d-holes than the nickel (II) or cobalt (II) ions. The copper L_3 and L_2 edges have not been modelled by van der Laan and Kirkman (1992), so no comparison can be made as for the other edges recorded.

6.2.6 Zinc

Unlike the other metal L_2 and L_3 edges which are dominated by two sharp peaks, the zinc L_2 and L_3 edges are broad and featureless, as shown in figure 6.9. This is because the zinc (II) ion has completely filled d-orbitals so the $2p$ electrons cannot be excited

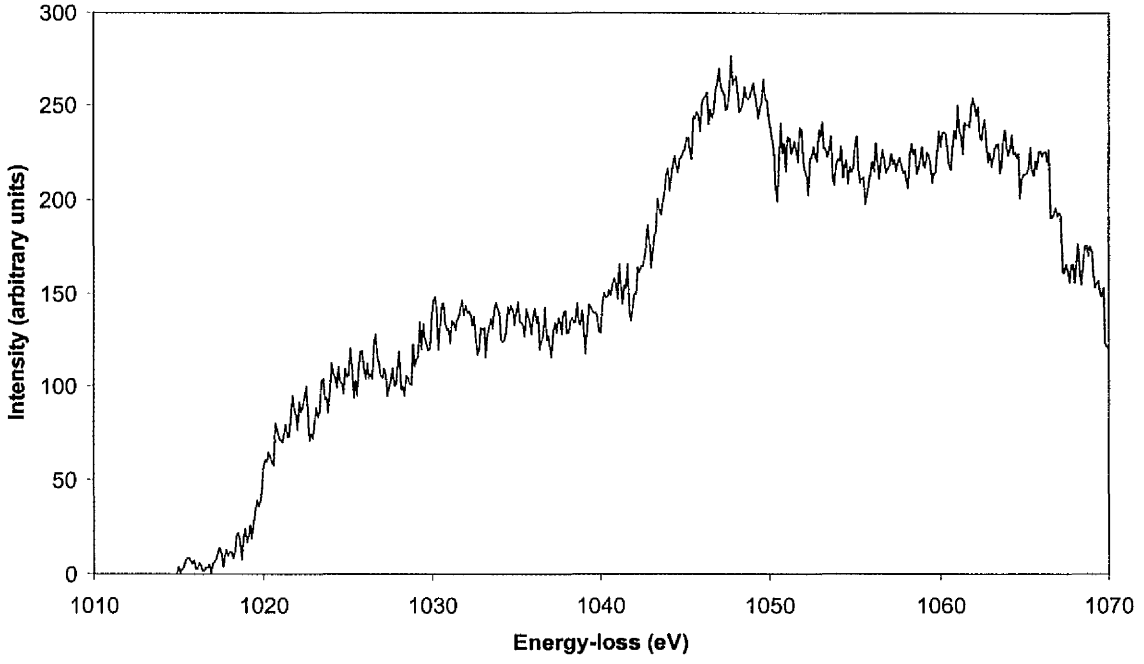

Figure 6.9 The zinc L_3 and L_2 edges from zinc chromite.

into 3d states. The structure observed is therefore mainly from transitions into metal 4s states, which are much broader than the narrow metal 3d states. The 4s states also have a much lower density than the metal 3d states, so the features are much less intense.

6.2.7 Comparison of the L_2 and L_3 edges in the different metals

The same basic shape is observed for the L_2 and L_3 edges for all of the metals, although the splitting in the peaks, which can be related to crystal field effects varies for different metals and different compounds. It is thought that the lack of splitting in the end members of the *3d* transition series is because the ground level t_{2g} or e_g levels are full, so only one type of site is available for the excited electron to occupy. The splitting is also complicated in some cases by the fact that the metal occupies both octahedral and tetrahedral sites.

For all of the L_2 and L_3 edges the L_2 edge is wider than the L_3 edge. This is due to the Coster-Kronig decay mechanism which is available for the L_2 but not L_3 edge. For the L_2 and L_3 edges decay is more likely to result in the emission of an Auger electron rather than radiation. The L_2 to 3d transition can be followed by the transfer of an electron from the 3d to $2p_{1/2}$ state to fill the $2p_{1/2}$ hole. This process generates enough energy for the emission of a $2p_{3/2}$ Auger electron and results in a $L_3^{-1}3d^n$ final state rather than a $L_2^{-1}3d^{n+1}$ state. Such a decay mechanism is not available for excitations to the L_3 states. The Coster-Kronig decay mechanism therefore means that the core-hole lifetime is smaller for the L_2 than L_3 states. Since the core-hole lifetime is inversely proportional to the energy broadening, as shown by equation 3.8, the L_2 states are found to be wider than the L_3.

It is interesting to note that the broad shoulder on the high-energy side of the L_3 peak that has been assigned to transitions to p-d hybrid states is strongest in the cobalt, nickel and copper spectra. In the oxygen K-edge spectra the metal (II) ions were thought to have little contribution to the hybrid states, and hybridisation was dominated by the metal (III) ions. However, in the metal L_2 and L_3 edges the feature thought to be due to transitions to hybrid states is weakest in the L_2 and L_3 edges of the metal (III) ions. This may be because the metal (III) ions have a significant number of extra holes than the metal (II) ions studied so that transitions to the pure *d* states, which have a high density of unoccupied states, are favoured in the metal (III) ions. As discussed in section 6.2.1, it is also interesting that there is some broadening of the shoulder on the chromium L_3 edges for the tetragonal compounds, even though there is no redistribution of the chromium 3d levels. This suggests that each type of ion cannot be considered independently, and the interactions between the ions must also be included for a complete interpretation of the ELNES data.

The separation of the L_3 and L_2 peaks is constant within each group of edges for each metal and, as expected, increases across the transition metal row, ranging from ~8.0eV for chromium to 19.7eV for copper. The position of the L_3 and L_2 peaks is fairly constant in each series, with the largest spread being 1.2eV for the chromium and nickel edges. The intensity of the L_2 peak relative to the L_3 peak is much higher for the chromium edges than for any other metal. This will be discussed further in section 6.4.

6.3 Determination of the occupancies of the 3d transition metal orbitals

6.3.1 Relationship between the L_2 and L_3 edge intensities and the number of d-holes

Since the L_2 and L_3 edges result from the transition of 2p electrons into empty 3d states, many studies have attempted to relate the intensities of these edges to the number of vacant states in the 3d orbitals. Studies for pure transition metals and binary transition metal oxides have found that the ratio of the combined intensity of the L_2 and L_3 edges to the atomic continuum beyond the edges is directly proportional to the number of d-holes in the transition metal (Pearson *et al*, 1993).

An attempt was made to carry out a similar analysis of the L_2 and L_3 edges recorded from the spinels that were discussed in section 6.2. To establish the numerical proportionality between white line intensity and *d*-holes the white lines must be isolated from the background and normalised. This was done using the approach of Okamoto *et al* (1992). The white line intensity was obtained by modelling the continuum intensity in the threshold region using a double step function and removing this from the experimental edges, as shown in figure 6.10. The ratio of the step heights is 2:1 in accordance with the multiplicity of the initial states, which are four and two for the $2p_{3/2}$ and $2p_{1/2}$ states respectively. This is due to the fact that the multiplicity of the states is 2j+1. The continuum was modelled using the partial cross-section for the L_3 and L_2 edges. This was discussed briefly in section 6.2.1 and will be described in more detail in the next section. The white line area is then divided by the area in the

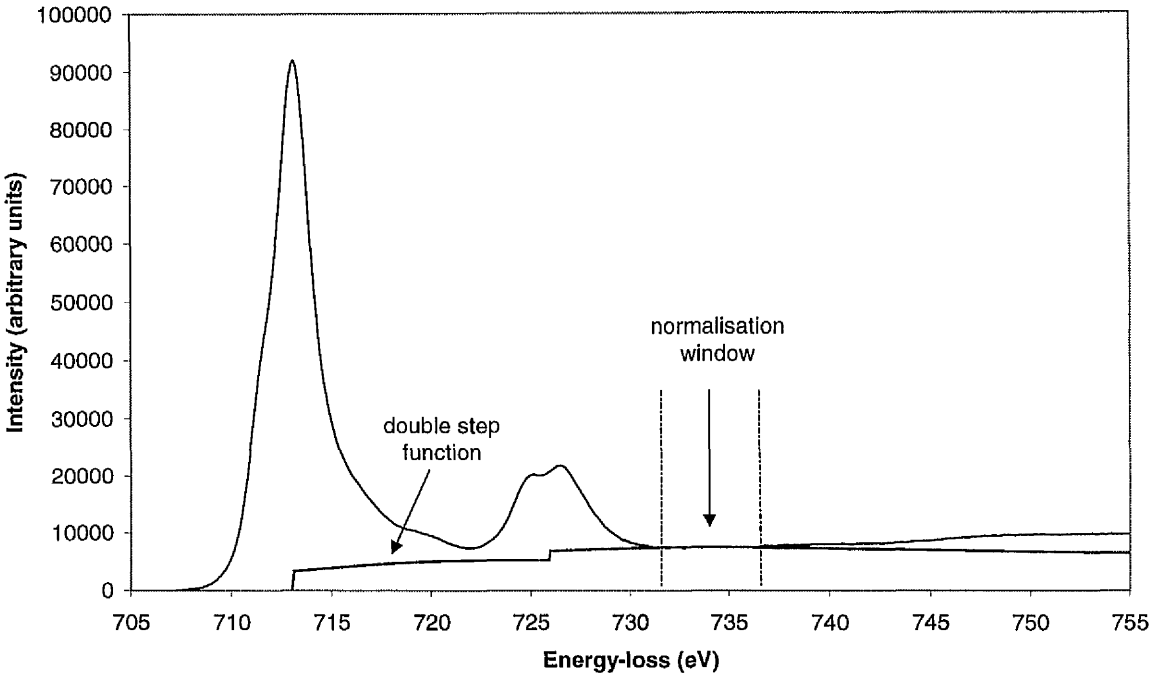

Figure 6.10 The double step function used to remove the background from the white lines.

normalization window. In the method of Okamoto *et al* (1992), this window was chosen to be 50eV wide, beginning 50eV beyond the L_3 edge. However the spectra recorded for the spinels did not extend to this energy-loss so initially a smaller window of 25eV width was chosen much closer to the L_2 and L_3 edges. This will be discussed further in section 6.3.3.

6.3.2 Modelling of the partial cross-section

Two models available in the EL/P program to model the partial cross-section were used. Both models use the general oscillator strength (GOS) (Egerton, 1996) which describes the response of the atom when it collides with a fast electron and is given a certain energy and momentum. The calculation of the GOS requires the initial and final state wavefunctions and the two models differ in how this calculated.

One approach uses the hydrogenic model, which is based on Egerton's programs SIGMAK2 and SIGMAL2 (Egerton, 1996). The GOS for the hydrogen atom can be calculated analytically and the result scaled to give approximate values for atomic number Z. This is achieved by modifying the electrostatic term to take account of the actual nuclear charge Z_e, and the screening of the nuclear field by the remaining (Z-1) electrons. A different effective nuclear charge is used for K and L shells to take account of core hole effects.

The Hartree-Slater (H-S) model is more complicated and is based on calculating the matrix element in the GOS from orthonormal H-S wavefunctions obtained by solving the Schrödinger equation for the bound and unoccupied continuum states in a self-consistent atomic potential.

A big difference between the results obtained using these models is that the hydrogenic model computes the L_2 and L_3 doublet as a single contribution whereas the H-S routine computes each component of the doublet separately. However, since the multiplicity of the states is 2j+1, the intensity of the L_3 edge should be twice that of the L_2 edge and this can be done manually for the hydrogenic case.

6.3.3 Results

Figures 6.11 shows the chromium L_3 and L_2 edges in cobalt chromite which have had the backgrounds removed as described in section 6.3.1 using the H-S and hydrogenic methods respectively. In both figures the partial cross-sections have been normalised to the experimental data using (a) a small window approximately 5eV wide and (b) a large window of approximately 25eV width. Because of the limited data available beyond

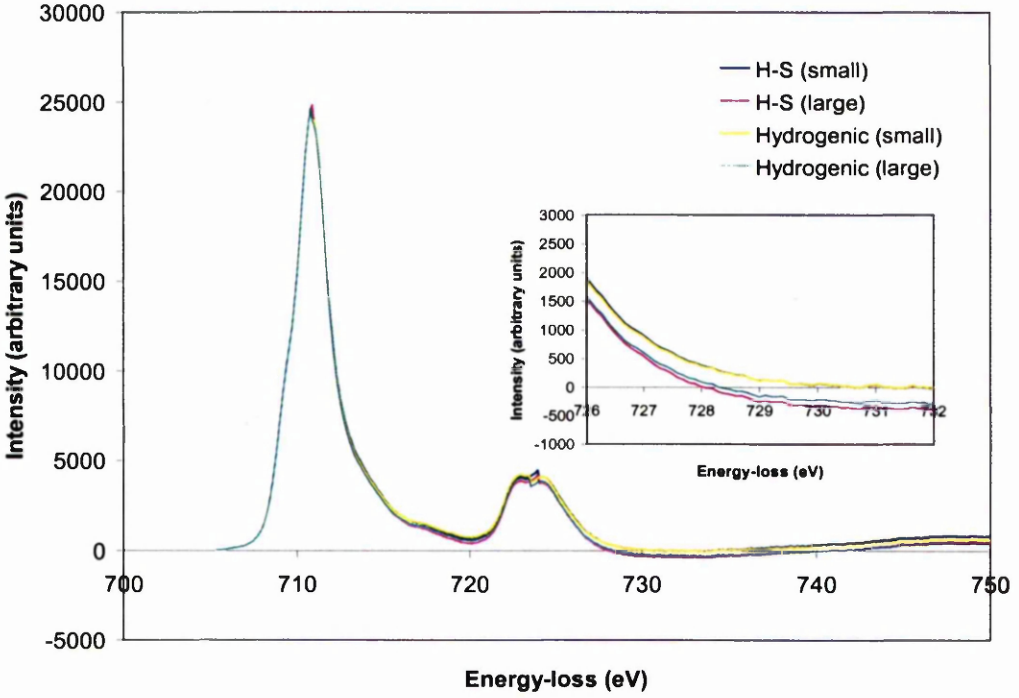

Figure 6.11 *Subtraction of the atomic continuum from the cobalt white lines from cobalt chromite using the hydrogenic and H-S models, and small and large normalisation windows.*

the edges these windows started at the energy at which it was judged that the intensity of the L_2 peak had levelled out. In all cases the removal has introduced a small artefact in the L_2 edge at the point where the intensity of the double step function changes. There is not much difference between the two models. However, for both models, when a large normalisation window is chosen the high-energy side of the L_2 peak appears to fall off more rapidly. It is thought that the small window spectra look more realistic in this area, although the difference is quite small. Therefore the analysis has been performed using a small integration window for the two models.

Figure 6.12 shows the ratio of the sum of the L_3 and L_2 peaks to the background for the chromium L_3 and L_2 edges in the five chromite spinels. In all of these compounds the chromium ion is in a +3 oxidation state, and has seven d-holes, so it would be expected that the ratio would be constant. To test if the observed differences in the ratio between

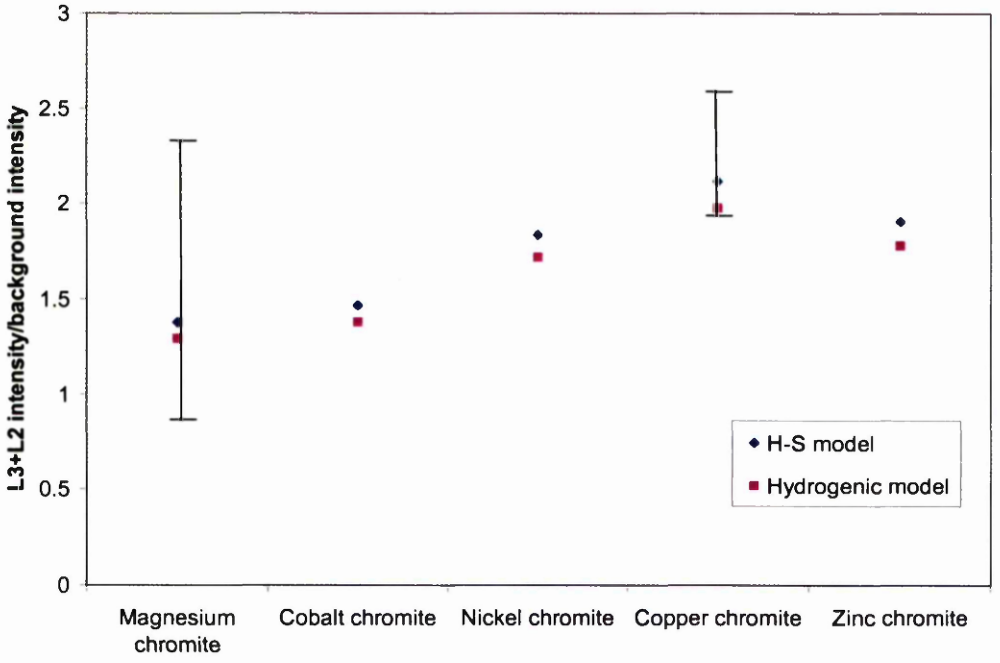

Figure 6.12 The ratio of the total white line intensity to the background for the five chromite spinels.

the compounds were meaningful, the procedure was repeated for the data from six magnesium chromite and five copper chromite particles to assess the particle-to-particle variations. The ratio ranged from 0.86-2.44 and 1.86-2.59 in magnesium chromite and copper chromite respectively suggesting that the differences between the different compounds cannot be taken to be meaningful. Closer examination of the data for these particles showed that the sum of the intensities from the L_3 and L_2 edges was within a fairly narrow range, but there was a large spread in the background intensities. This suggests that the wide variation observed is due to incorrect background intensities, which probably arose from failure to correctly remove the multiple scattering contributions. This would mean that different background intensities would be obtained for particles of different thickness. Therefore an improved deconvolution routine would have to be developed before this data could be properly interpreted.

Improper background subtraction would result in an error in both the intensities of the L_3 and L_2 edges, but the error would be fairly constant for both cases, so could be

regarded as a systematic error to a certain extent. Therefore the ratio of the L_3 to L_2 intensities should be fairly constant, since this error would cancel out to some degree. This was found to be the case since the ratio was 1.67±0.05 and 1.63±0.04 for magnesium chromite and copper chromite respectively. The analysis then concentrated on looking at the L_3 to L_2 intensity ratio rather than the total white line to background intensity ratio.

6.4 L_3 / L_2 white line intensity ratios

6.4.1 Theory

On the basis of the 2j+1 degeneracy of the initial core states, it is expected that the ratio of the intensities of the L_3 to L_2 peaks should be 2: 1. However, many measurements of this ratio in the 3d transition metals and their oxides show that there are large departures from this ratio (for example Leapman and Grunes, 1980, Leapman *et al*, 1982, Sparrow *et al*, 1984 and Morrison *et al*, 1985). One reason for studying this ratio is that it provides information on the pairing of the electrons in the d-states. This can be related to the magnetic moment, which is particularly useful since the transition metals and their oxides have many interesting magnetic properties. The relationship between the white line intensity ratio and the electron pairing arises from the fact that the white lines result from the change in electronic configuration from $2p^6 3d^n$ to $2p^5 3d^{n+1}$. Since there is a spin selection rule, $\Delta S=0$, the $2p_{3/2}$ electrons must be excited into $3d_{5/2}$ holes and the $2p_{1/2}$ electrons must reside in $3d_{3/2}$ holes. Therefore changes in the white line ratio for a particular ion would indicate a transition from a low-spin to a high-spin state for example.

6.4.2 Results and discussion

The intensities of these edges were obtained in the manner described in section 6.3.1. The intensity of the L_3 edge was defined as the number of counts from the edge onset to the minimum turning point between the L_3 and L_2 edges. The intensity of the L_2 edge was defined as the number of counts from the minimum turning point between the L_3 and L_2 edges to the energy at which the intensity became negative on the high-energy side of this edge. For the cobalt, nickel and copper edges, the background subtraction resulted in an area of negative intensity between the L_3 and L_2 edges, when both the hydrogenic and H-S models are used to model the atomic continuum. Figure 6.13 shows the result for the cobalt L_3 and L_2 edges for cobalt chromite. The use of a small or large window for normalisation did not prevent this negative region. This effect has

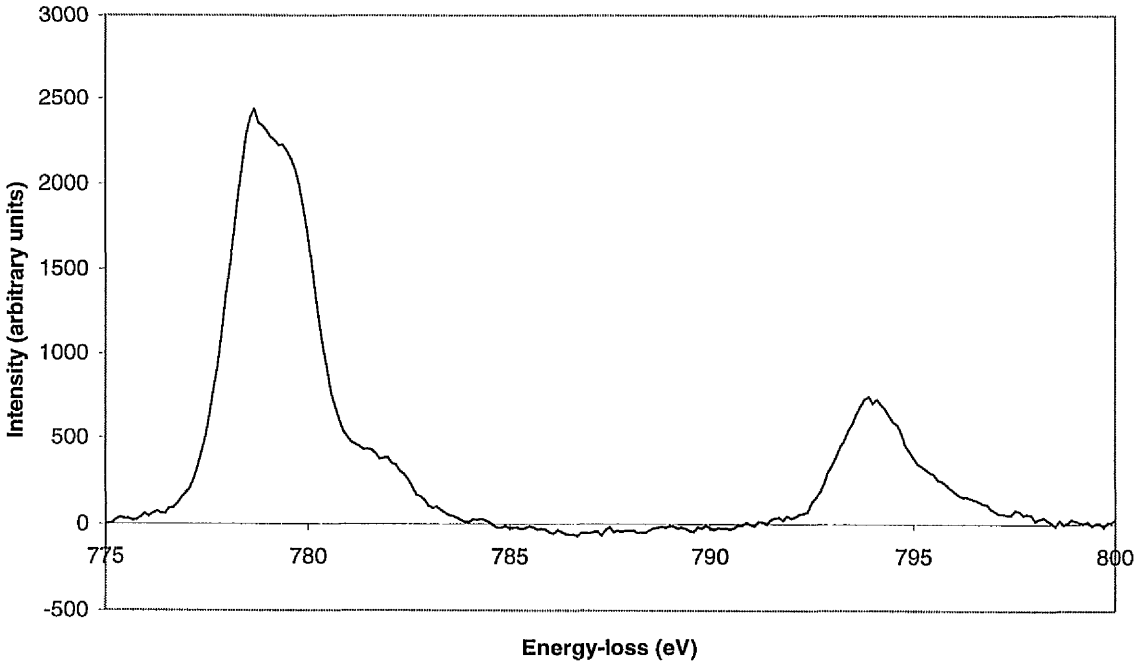

Figure 6.13 Resultant spectrum when the double step function is removed from the cobalt L_2 and L_3 edges from cobalt chromite.

also been observed by Stolojan *et al* (1999). They believe the origin of this effect is extended energy loss fine structure (EXELFS), which causes a redistribution of the intensity. The EXELFS oscillations extend for a few thousand eV beyond the edge onset and the integral of the EXELFS signal over this range is zero. They have modelled the EXELFS for haematite and found that the effect of the EXELFS is to lower the intensity between the L_3 and L_2 edge. They have also found that the total contribution of the EXELFS from the onset of the L_3 edge to the to the first intersection after the L_2 edge of the experimental spectrum with the continuum amounts to zero. Therefore the 'negative' area has to be subtracted from the number of counts in the white line edges. This procedure has been followed for all of the cobalt, nickel and copper L edges.

Figure 6.14 show the L_3/L_2 ratios obtained using the H-S models for all of the transition metal edges recorded. The results from both the H-S and hydrogenic models are very similar, so only those obtained using the H-S model are considered. The values for the

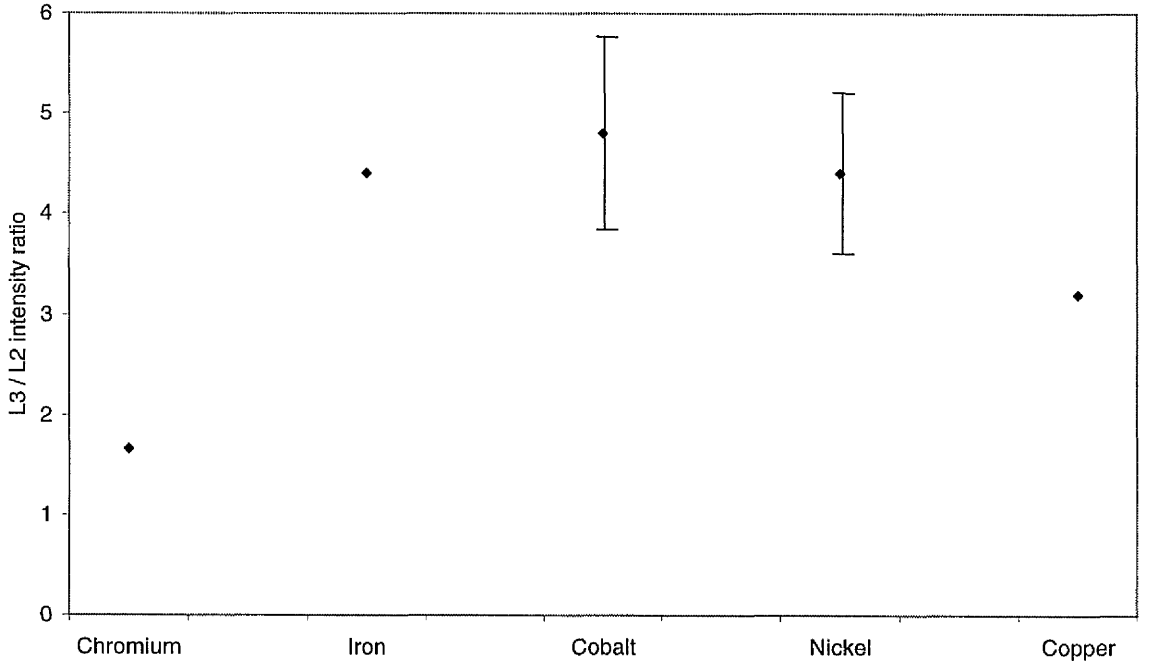

Figure 6.14 The L_3/L_2 intensity ratios for the transition metals studied.

chromium and iron edges, with standard deviations of 0.04 and 0.16 respectively, are consistent but there is a larger variation in the ratios for the cobalt and nickel edges. The standard deviations for cobalt and nickel are 0.95 and 0.85 respectively. There is only one copper-containing compound so it is not known how accurate the result is for the copper ratio. To test how significant the variation observed in the nickel ratios was, the ratio was obtained for five nickel aluminate particles. The spread in the results was 3.6 to 5.1 indicating the differences between the compounds are not meaningful. In the work of Morrison *et al* (1985) on iron germanium alloys with different iron ratios, a jump in the white line ratio from ~3.8 to 7 was observed and was related to a change in the magnetic moment at that composition. However, the value 3.8 was the average of three ratios that ranged from 2.9 to 4.5. This spread is of the same order observed for the spinel edges. Therefore the spread observed is not thought to indicate changes in the electron spin pairing in these compounds and may be due to errors in the complicated routine used to separate the white line intensities from the background. No correlation can be drawn between the thickness of the particles and the values obtained so it is not thought that the problems with the deconvolution routine, discussed in section 6.3.3 have a significant effect on this ratio.

Table 6.2 compares the average ratios for each metal obtained in this study with those of Leapman *et al* (1982) and Sparrow *et al* (1984). Results for spinels cannot be found in the literature, so this comparison has been made to binary transition metal oxides. Since the transition metal ions are in the same oxidation states in these compounds, a valid comparison can be made. Leapman *et al* (1982) have obtained the ratios using the technique described in section 6.2.1 (method 1) and a deconvolution technique (method 2) described in detail in their paper. The results from this study for the chromium, nickel and copper ions are in fairly good agreement with those of Leapman *et al.* The

ratios of Sparrow *et al* are consistently lower than those obtained in this study. There is good agreement for the chromium ions but a significant difference for the other ions. The ratios obtained by Sparrow *et al* were obtained in the same manner to this study, but the background was normalised over a 100eV wide window, rather than 25eV in this case.

Metal	Number of *d*-electrons	L_3/L_2			
		This study	Leapman *et al*		Sparrow *et al*
			Method 1	Method 2	
Cr (III)	3	1.7	1.7	1.8	1.6
Fe (III)	5	4.4	-	-	3.6
Co (II)	7	4.8	-	-	2.6
Ni (II)	8	4.2	4.0	3.8	2.5
Cu(II)	9	3.2	3.5	3.5	1.1

Table 6.2 *Comparison of the L_3/L_2 ratio from different studies for various transition metals .*

For all of the results in table 6.2 there are significant deviations from the 2:1 ratio predicted. There is no simple reason for the deviation and the complete explanation is likely to involve many factors. Leapman *et al* (1982) have discussed a number of possible explanations which mainly are due to the many-body effects already discussed in this chapter. The anomalous white line ratios are another example of how important exchange interactions and other factors are in the interpretation of the L_2 and L_3 edges and illustrate how unsuitable the one-electron approximation is for these edges.

6.5 Metal K-edges

6.5.1 Introduction

In this section the magnesium K and aluminium K edges from the appropriate spinels studied will be discussed. These edges have nominal energies of 1240eV and 1330eV respectively and can be studied in the HB5 STEM used. The first row transition metal K-edges occur at higher energy losses and are outwith the range accessible to the HB5. An X-ray source at a synchrotron would be the normal mode of excitation employed to observe their fine structure.

The magnesium and aluminium K-edges have been recorded using the method described in section 2.3.2. Their energies are not known as accurately as for the oxygen K and metal L_2 and L_3 edges for two reasons. Firstly, as discussed in that section it was necessary to use a dispersion of 0.5eV per channel to collect an adequately large signal in a sufficiently small time to avoid damaging the sample with the electron beam, and to avoid the sample drifting. The EL/P software used calibrates the energy dispersion by applying known voltages to shift the zero loss peak. However, the energy dispersion is non-linear with increasing energy-loss, so the energies of the edges calculated by using a dispersion of 0.5eV per channel are only approximate at such a high energy-loss. Secondly, the sequence of spectra recorded was a zero loss peak followed by three spectra of the metal K-edge. The large integration times required to record these core edges mean that there may have been some drift of the zero loss peak which was not detected, which would also lead to inaccuracies in the energy calibration of these edges. Therefore in this section the energies stated can only be regarded as approximate. The emphasis will be on comparing the spectra qualitatively and looking

at relative energy changes rather than a detailed analysis of changes in absolute energies as carried out for the other core-loss edges already discussed.

6.5.2 Magnesium K-edges

6.5.2.1 General observations

The magnesium K-edges recorded from magnesium aluminate, magnesium chromite and magnesium ferrite are shown in Figure 6.15. All of the spectra display three distinct peaks labelled A-C, although the relative intensities of these peaks vary for the three compounds. A shoulder on peak A, labelled A', is also observed in the magnesium chromite edge. The edge recorded from magnesium chromite displays a peak, labelled D, that is not observed for the other compounds. The magnesium aluminate edge exhibits a well-defined peak, labelled E, at a higher energy-loss than peak D. For the other two compounds an increase in intensity is observed in a similar energy-loss region, but a well-defined peak is not observed.

The relative energy differences between the main features in the spectra are given in table 6.3. As already discussed at the beginning of section 6.5, the absolute energies are not known accurately so only a comparison of the relative energies will be made. With the exception of the same energy separation between peaks A and B for magnesium chromite and magnesium aluminate, the general trend observed is that the separation between the features decreases as the degree of inversion increases.

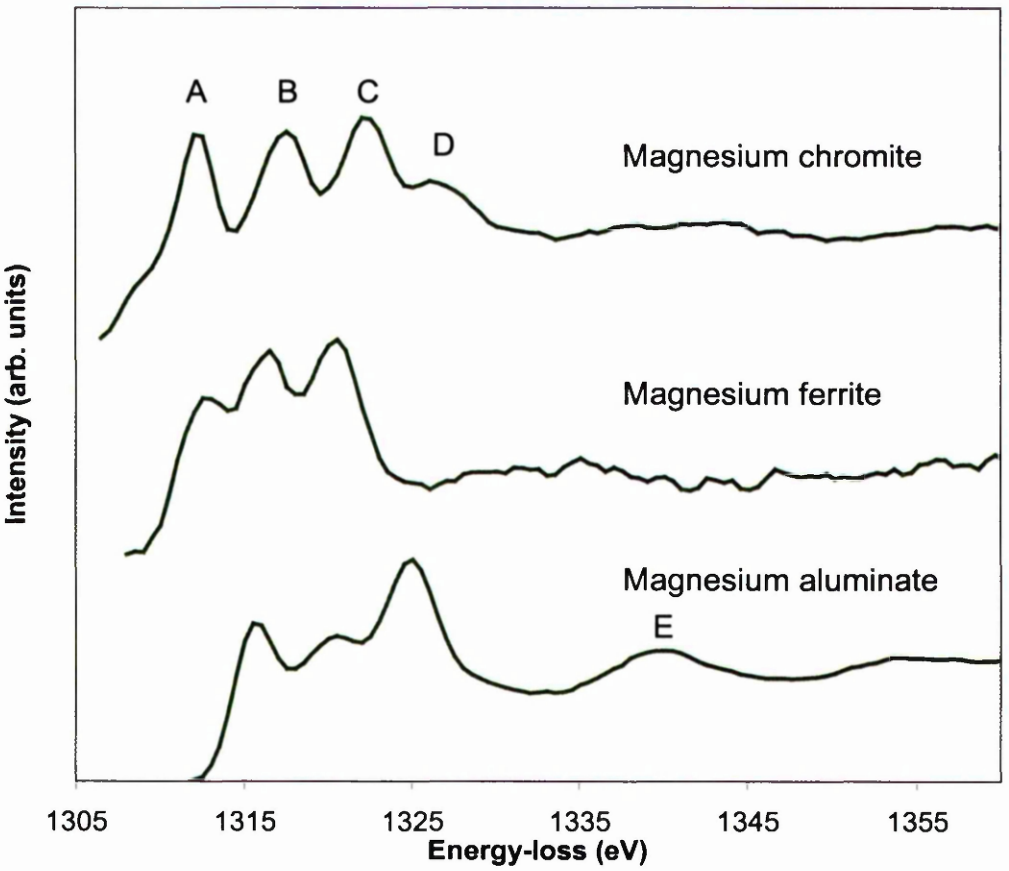

Figure 6.15 *The magnesium K-edges recorded from the three magnesium-containing spinels.*

Compound	Inversion Parameter	Relative Energy Separation Between Peaks (eV)	
		A and B	A and C
$MgAl_2O_4$	0.32	5.0	9.5
$MgCr_2O_4$	0.00	5.0	10.1
$MgFe_2O_4$	0.88	3.5	7.5

Table 6.3 *Relative energy separations between various features in the magnesium K-edge spectra.*

6.5.2.2 Magnesium ferrite

As shown in table 4.2, magnesium ferrite is completely inverse, so all of the magnesium ions occupy octahedral sites. No example of this edge can be found in the literature, but the spectrum can be compared to other materials where the magnesium ion exclusively occupies six-fold sites.

Ildefonse *et al* (1995) and Cabaret *et al* (1998) have recorded the magnesium K-edge from the mineral diopside using the XANES technique. The magnesium ions are also found in regular MgO_6 octahedra in this compound. The magnesium K-edge from both studies is compared to the magnesium K-edge from magnesium ferrite in figure 6.16. The fine structure for diopside from both studies comprises of three main peaks, labelled A, B and C, spanning an energy-loss range of ~10eV, and a broader resonance, labelled D, at ~20eV beyond the edge onset.

Cabaret *et al* (1998) have modelled the magnesium K-edge fine structure for diopside using the FMS formalism discussed in section 3.4. A cluster of 99 atoms was required to reproduce the first three peaks observed in the 10eV beyond the edge onset in the experimental spectrum. For smaller clusters these peaks are not resolvable and appear as one broad peak. This indicates that these three peaks are related to medium range order.

Another case in which the fine structure in the magnesium K-edge is dominated by medium range order is magnesium oxide. The magnesium ions also form regular MgO_6 octahedra in this compound. Ildefonse *et al* (1995) and Aritani *et al*(1996) have published this spectrum, which are also shown in figure 6.16. Both studies produced

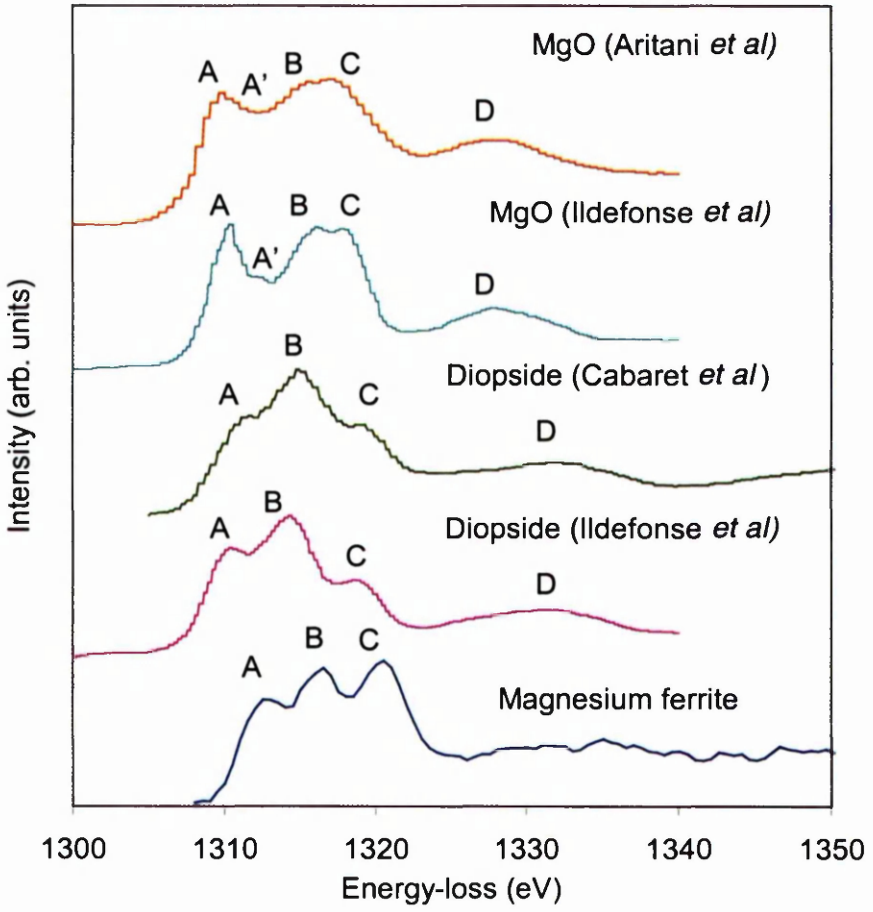

Figure 6.16 *Comparison of the magnesium K-edges from a number of compounds in which the magnesium ion is octahedrally co-ordinated to six oygen ions.*

spectra that exhibit similar features, namely a sharp peak at the edge onset, A, that has a small shoulder on the high-energy side, A', and a wider peak that has split into a doublet, labelled B and C at slightly higher energy-loss. A broad resonance, D, is also present about 12eV beyond this doublet. The relative intensity of peak A is higher in the work of Ildefonse *et al* than in the work of Aritani *et al*. This spectrum is similar to that of diopside in that there are three resolvable features in the first 10eV beyond the edge onset, whose positions relative to the edge onset are approximately the same in both cases. In the case of diopside the three peaks are quite distinct, rather than split into a single and double peak as in the magnesium oxide spectrum, and the relative intensities vary between the two cases.

For both compounds the magnesium ion is octahedrally co-ordinated to six oxygen ions. The differences in fine structure for the two cases, and the multiple scattering calculations of Cabaret *et al* (1998) suggest that the fine structure is dominated by more distant neighbouring ions than the first co-ordination shell. This is especially significant given that the nearest neighbours are oxygen ions. For the oxygen K-edges presented in section 5.2, the oxygen ions were the dominant scatterers compared to the metal ions, so it may have been expected that the nearest neighbour oxygen ions would have the largest influence on the magnesium K-edge.

6.5.2.3 Magnesium aluminate

The only publication of the magnesium K-edge in magnesium aluminate which can be found in the literature is that recorded by Ildefonse *et al* (1995) using the XANES technique. Their spectrum is compared to that recorded in this study in figure 6.17. Both spectra have three main peaks, labelled A, B and C. The relative separation of the peaks is similar in both studies, but all features are at higher energies in this study. It has already been stated that there are inaccuracies in the absolute energies in this work, so no comparison of the absolute energies will be made. The features in the spectrum of Ildefonse *et al* are sharper than observed in this work. Peak B in particular is much sharper. The other main difference is that in their study peaks B and C have similar relative intensities to this work, but the intensity of peak A is slightly greater than that of peak C, whereas in this study it is lower than peak C. They have also observed a feature that can be compared to peak D in this study. In their work this peak has split into a doublet, labelled D and D'.

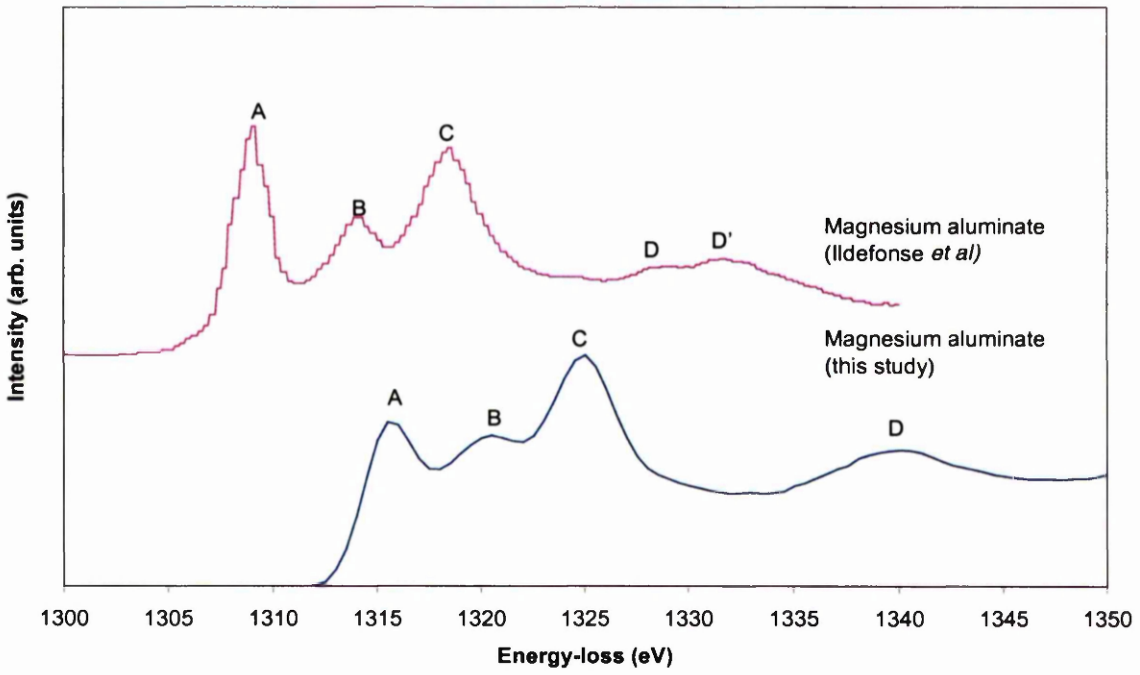

Figure 6.17 *Comparison of the magnesium K-edge in magnesium aluminate from this study and the literature.*

The clearer distinction between peaks B and C and the splitting of peak D into a doublet observed by Ildefonse *et al* may not have been observed in this study if the energy resolution was lower in this work. It is not known if this is the case since the energy resolution was not given be Ildefonse *et al*. However, experimental limitations cannot explain the difference in the relative intensities of peak A in the two studies. One reason for the differences observed could be that the samples have different degrees of inversion in the two cases. Ildefonse *et al* do not discuss inversion, but they do assume the magnesium ions only occupy tetrahedral sites. As shown in table 4.2, it is known that the sample used in this study is partially inverse. The magnesium aluminate spectrum from this study in figure 6.17 therefore has contributions from magnesium ions in both tetrahedral and octahedral sites.

Mo and Ching (1996) have used density functional theory to calculate the site and symmetry projected density of states for the magnesium ion in normal and inverse magnesium aluminate. For the magnesium ion at the tetrahedral site in normal spinel the p-like states at the bottom of the conduction band comprise of three peaks which span an energy-loss range of 5eV. The peak at highest energy in this group has a sharp shoulder on its high-energy side. In the case of the inverse spinel, when all of the magnesium ions are placed at the octahedral sites, there is broadening of the three peaks. The shoulder is no longer observed on the highest energy peak but a shoulder is now present on the low energy side of the lowest energy peak. Mo and Ching have attributed this broadening of the partial DOS to the increased disorder due to cation exchange in the inverse spinel. This finding is in agreement with the discussion in section 6.5.2.2 that the magnesium K-edge fine structure is dominated by medium range order, since the nearest neighbour co-ordination remains ordered for the inverse spinel. The disagreement between the experimental spectrum presented in figure 6.17 and that of Ildefonse *et al* (1995), in particular the differences in the sharpness of the features, may therefore be due to difference in the degree of inversion in both samples.

6.5.2.4 Magnesium chromite

No example of this edge could be found in the literature for comparison. Since, as shown in table 4.2, this compound is essentially normal, the magnesium ions only occupy tetrahedral sites. Therefore a comparison was made with a material in which the magnesium ions are solely in tetrahedral co-ordination. This approach may not be valid if this edge is dominated by medium range order, as discussed in sections 6.5.2.2

and 6.5.2.3, but was considered to further investigate the importance of the local co-ordination environment.

The only suitable example that could be found in the literature was the magnesium aluminate spectrum of Ildefonse *et al* (1995), already discussed in section 6.5.2.3. This spectrum is compared to the magnesium K-edge recorded from magnesium chromite in figure 6.18. The intensity of peak A is greater in the experimental magnesium chromite spectrum than in that recorded for magnesium aluminate in this study and is therefore closer to that observed by Ildefonse *et al.* However, the intensity of peak B in the magnesium chromite spectrum is much greater than observed in their study. Peak E in the magnesium chromite experimental spectrum, and the shoulder on the low-energy side of peak A are not observed in their study. The differences between the experimental spectrum and that of Ildefonse *et al* (1995) provide further evidence that

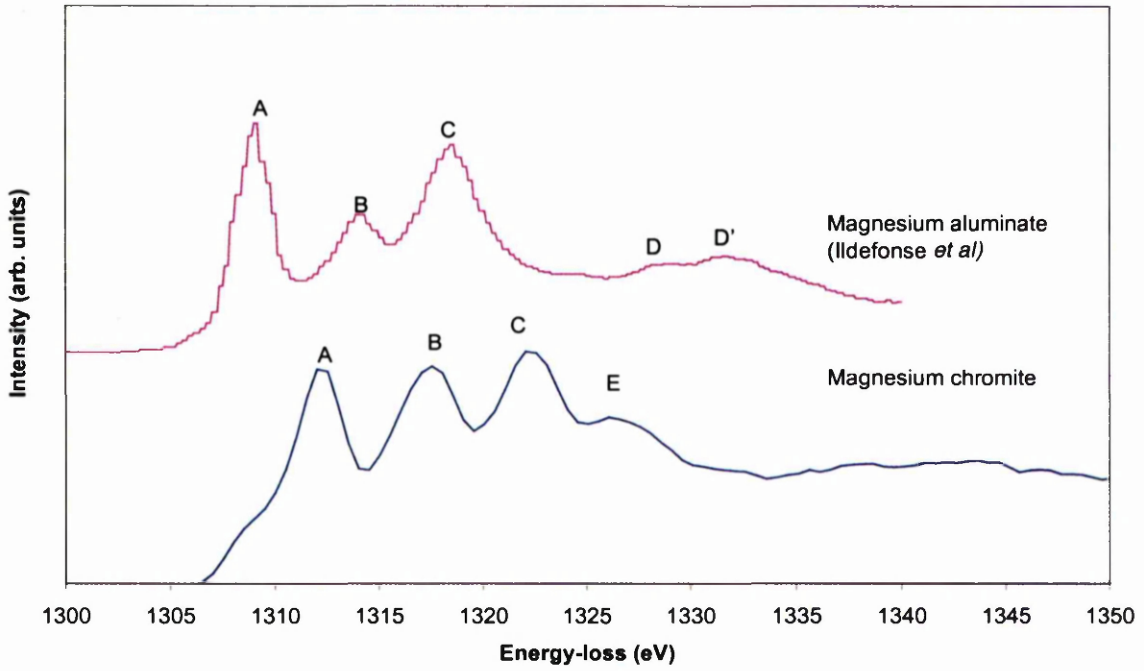

Figure 6.18 *Comparison of the magnesium K-edge in magnesium chromite from this study with that from magnesium aluminate from the literature. The magnesium ion is mainly tetrahedrally co-ordinated to oxygen in both compounds.*

the magnesium K-edge fine structure is not dominated by the immediate neighbourhood of the excited atom.

It is interesting to note that although significant variations are observed between the spectra for the other compounds and those discussed in the literature, the general form of the fine structure is a group of three peaks near the edge onset. Magnesium chromite is the only compound in which an additional peak, labelled D in figure 6.16, is observed. This compound is the only spinel that is completely normal out of the three considered. It has already been discussed that inversion may lead to broadening of the fine structure, as illustrated by Mo and Ching (1996). Therefore peak D may have been obscured by broadening for the other two spinels considered. However, a more extensive study including other normal spinels would have to be undertaken to investigate this idea further.

6.5.3 Aluminium K-edges

6.5.3.1 General observations

The aluminium K-edges recorded from magnesium aluminate, nickel aluminate and zinc aluminate are shown in figure 6.19. In the near-edge region all of the spectra have the same general form, namely a large peak near the edge onset, labelled A in figure 6.19, and a less intense peak, B, at higher energy-loss. A number of broad resonances are also present at higher energy-losses. Peak A has a slight shoulder on both the low and high-energy sides in all cases. The relative energy separation between peaks A and B is constant to within 0.5eV as shown in table 6.4. Figure 6.20 also illustrates that

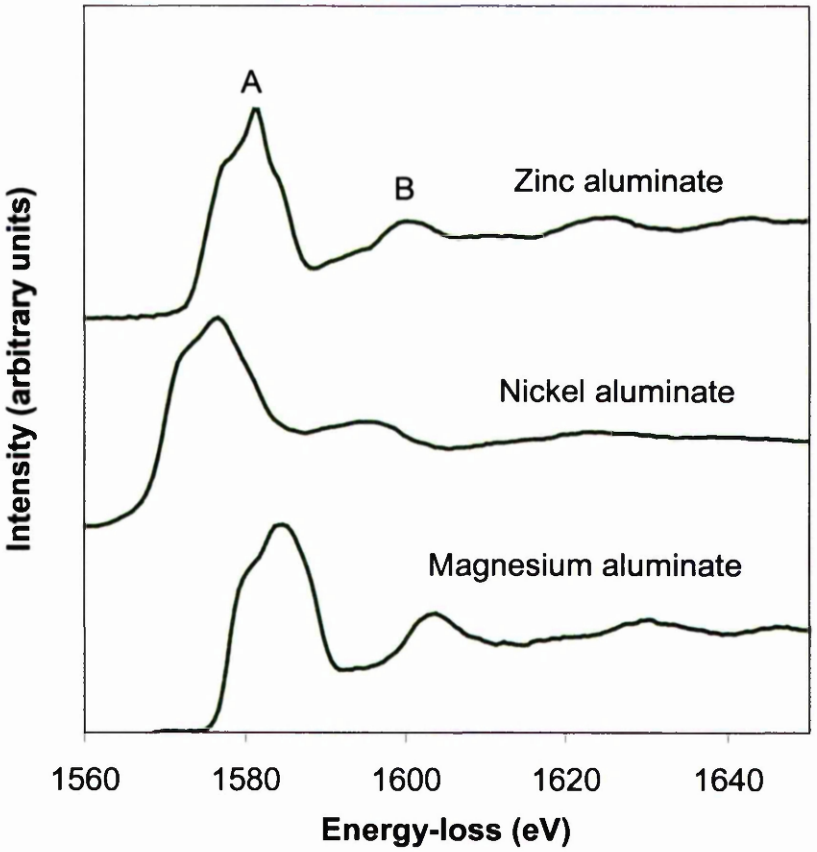

Figure 6.19 *The aluminium K-edges from the aluminium-containing spinels studied.*

peak B occurs at the same energy-loss relative to peak A in all cases. In this figure the spectra have been aligned and normalised to peak A.

	Relative Energy Separation Between Peaks A and B (eV)
$MgAl_2O_4$	19.5
$NiAl_2O_4$	19.0
$ZnAl_2O_4$	19.1

Table 6.4 *The relative energy separation between features A and B in the aluminium K-edges recorded.*

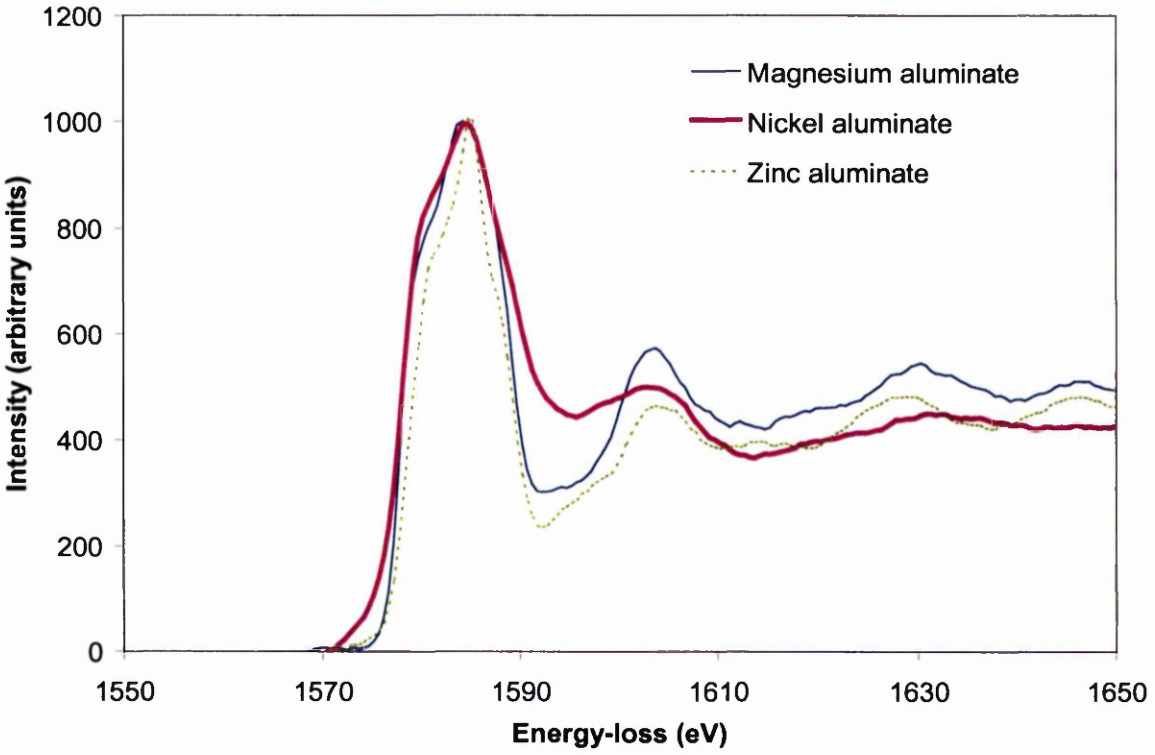

Figure 6.20 *The aluminium K-edges recorded aligned and normailsed to the most intense point in peak A.*

Figure 6.20 also illustrates that the width of peak A is greatest in the spectrum recorded from nickel aluminate and narrowest in that of zinc aluminate. It is interesting to note that the widest peak corresponds to the most inverse aluminate spinel, and the narrowest to the most normal. This could be predicted for two reasons. Firstly, in the inverse case the edge has features from aluminium ions in both tetrahedral and octahedral co-ordination. Secondly, in section 6.5.2 it has been shown that for the magnesium K-edge, inversion leads to a widening of the near-edge structure due to the disorder in the medium range order which dominates the fine structure in this region. A similar observation has been made by Mo and Ching (1996) from their density functional calculations of the site and symmetry projected density of states for the aluminium ion in octahedral co-ordination in normal and inverse spinel. The change in

inversion leads to a broadening of the conduction band states, which they have attributed to second-nearest-neighbour effects.

6.5.3.2 Six-fold co-ordination aluminium

No recording of the aluminium K-edge for any spinel can be found in the literature. The best comparison that can therefore be made is with the aluminium K-edge recorded from compounds in which the aluminium ion is octahedrally or tetrahedrally co-ordinate to oxygen ions. There have been a number of studies to investigate the effect on the near edge structure of changing the co-ordination number of the aluminium ion.

In corundum, or α-alumina, Al_2O_3, the cation is at the centre of a slightly distorted octahedron of oxygen ions, so the local environment is therefore structurally similar to that of the aluminium ion in normal spinels. The aluminium K-edge XANES spectrum for this material has been reported by a number of workers, including Cabaret *et al*, 1996, Mottana *et al*, 1998 and van Bokhoven *et al*, 1999, and is shown in figure 6.21. An intense, sharp feature at the edge onset, A, which has a weak shoulder on the low energy-loss side, A', dominates the near-edge structure. A second strong, but not as sharp feature, B, is present around 4eV beyond this sharp peak. A less intense, but well-defind feature, C, can be observed at higher-energy loss. The aluminium K-edge from zinc aluminate is shown in this figure for comparison since zinc aluminate is essentially normal, so almost all of the aluminium ions are octahedrally co-ordinated. The best correlation which can be made between the edges from zinc aluminate and corundum is that the general edge shape is dominated by one large intense peak near the edge onset, which has a number of smaller intensity features superposed on it.

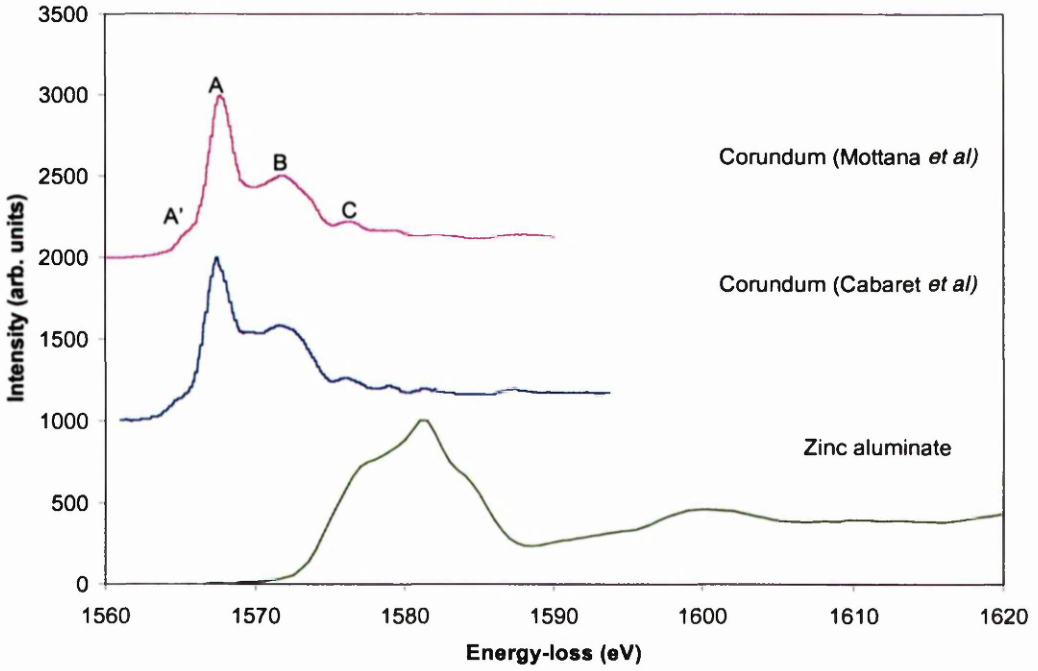

Figure 6.21 *The aluminium K-edge from zinc aluminate and corundum. The alumnium ion is octahedrally co-ordinated to six oxygen ions in both cases.*

These lower intensity features do not have similar intensities or energy separations relative to the edge onset for the two compounds.

Multiple scattering simulations by Cabaret *et al*, 1996 and Mottana *et al*, 1998 have confirmed that as in the case of the magnesium K-edges, part of the fine structure is dominated by medium-range order. The most intense peak can be assigned to short range order, but the other features arise from interactions of the photoelectron with atoms in the second or higher co-ordination sphere. In particular the shoulder on the most intense peak can only be reproduced when using a large cluster size. The lack of similarity between the corundum and zinc aluminate edges, and the requirement of a large cluster size to successfully reproduce the features in the corundum edge provide further evidence for the large influence of the medium range order on the near edge structure.

6.5.3.3 Four-fold co-ordinated aluminium

The aluminium ion in berlinite, $AlPO_4$, is at the centre of a slightly distorted AlO_4 tetrahedron. The Al K-edge has been recorded by Cabaret *et al*, 1996 and Bugaev *et al*, 1998. Similar features are observed in both studies, and the edge recorded by Cabaret *et al* is shown in figure 6.22. Unlike the case where the aluminium ion is octahedrally co-ordinated, the spectrum consists of a single, well-defined resonance, A, which has an extremely weak shoulder, A', on its low energy side. The second most intense feature, C, occurs about 9eV beyond the edge onset, but is significantly weaker than the most dominant peak. A small broad resonance, B, is visible between these two main features. Another broad resonance, D, is observed around 18eV beyond the edge onset. No spectra from spinels have been included in this figure since no spinel has been studied in which the aluminium ion exclusively occupies tetrahedral sites. However, it

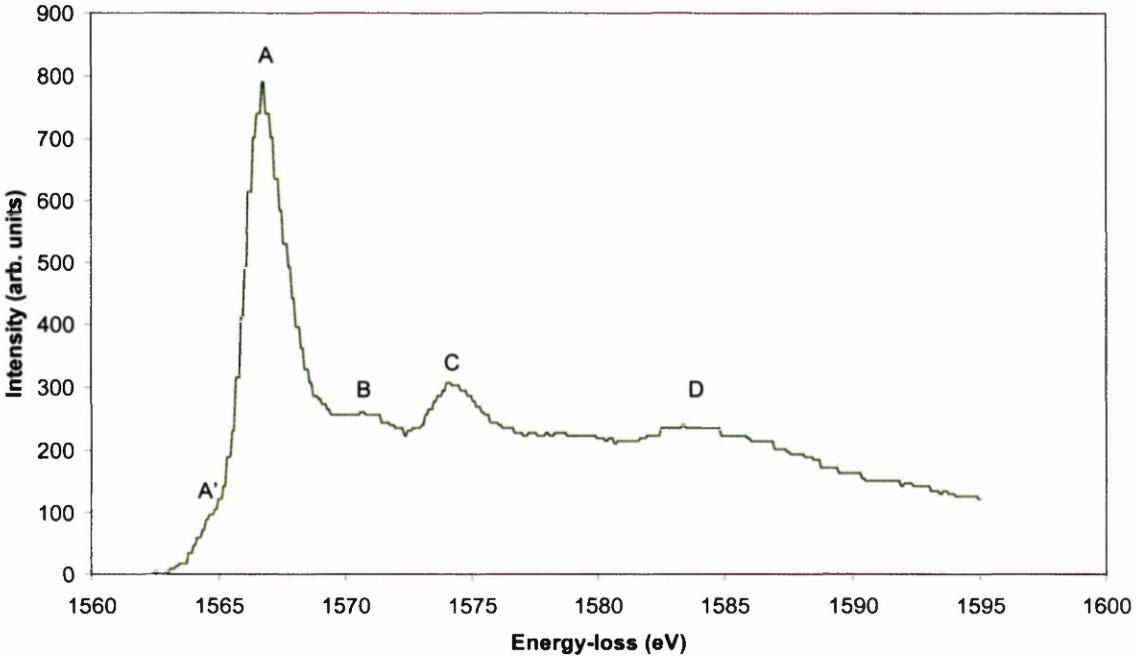

Figure 6.22 The aluminium K-edge from berlinite, recorded by Cabaret et al (1998). The aluminium ion is tetrahedrally co-ordinated in this compound.

obvious that, as for the case of the aluminium K-edge from aluminium in sixfold co-ordination, there are few similarities between the edge from aluminium in fourfold co-ordination and the experimental data from the spinels.

The multiple scattering calculations of Cabaret *et al*, 1996, for this material indicate that the a large cluster again has to be used to reproduce all of the features in the fine structure, again showing the importance of medium-range order on the fine structure for the metal K-edges studied.

6.5.4 Summary of results

In this section the magnesium and aluminium K-edges recorded have been presented. Although the general shape of the fine structure is the same within each group, a number of trends have been observed which may be related to the degree of inversion in the sample.

In the case of the aluminium K-edges, the broadness of the main peak increases as the degree of inversion increases. This may be expected since in a normal spinel the aluminium ion only occupies one type of site, but occupies two types in an inverse spinel. In the magnesium K-edges an extra peak is observed in the magnesium chromite spectrum. This is the only magnesium-containing sample that is normal. If inversion causes broadening of the fine structure this feature may be present but obscured for the other magnesium spinels. Examples from the literature of simulations of these edges for similar compounds show that the fine structure is dominated by medium range order rather than the nearest neighbour environment, and that disorder in the medium range environment results in broadening of the density of conduction band

states. This provides further evidence that changes in the degree of inversion could have a noticeable effect on the near-edge structure.

To confirm a link between the fine structure of these edges and the degree of inversion a more extensive study of samples with a wide range of degrees of inversion would have to be undertaken. It would also be interesting to simulate these edges to investigate the effect of changing the degree of inversion. Although no conclusive link can be drawn at present, far more obvious relationships between the fine structure in these edges and the degree of inversion can be immediately noticed compared to the oxygen K or metal L_3 and L_2 edges.

Chapter 7

Comparison of the metal and oxygen edges

This chapter will complete the discussion of the near-edge structure of spinels by attempting to correlate the oxygen K-edges presented in chapter 5 and the metal L_3, L_2 and K-edges discussed in chapter 6, for some of the spinels studied. In chapters 5 and 6 a number of factors were found to influence the fine structure, such as hybridisation and the degree of inversion in the sample. This chapter will look at the effect of some of these factors on the fine structure on both the metal and oxygen edges, to investigate the consistency and complementary nature of the information obtained from each type of site.

7.1 Effect of d-orbital occupancy on the ELNES

7.1.1 Hybridisation

In section 5.1 significant extra fine structure was observed on the oxygen K-edges when the metal (III) ion was changed from a main group species, aluminium, to chromium, a transition metal ion. In contrast, changing the metal (II) ion from one with full or empty d-orbitals to one with partially filled d-orbitals, had little effect on the fine structure in the chromites. A similar trend was observed when the metal (III) ion was changed from chromium to iron, *i.e* the iron (III) ion again results in extra fine structure compared to the main group case. As in the chromites, replacement of a main group metal (II) ion in the ferrites to a transition metal had little effect on the fine structure. The extra fine structure was assigned to transitions to unoccupied states created on the oxygen sites by the interaction of the oxygen 2p and transition metal 3d orbitals.

In section 5.1.3 a semi-quantitative explanation for these observations was given in terms of the number of empty d-states, and the strength of the interaction between the oxygen 2p and metal 3d orbitals. The magnitude of this interaction was found by calculating the p-d coupling constant for all of the cases studied. The p-d coupling constants calculated showed the interaction is greater between the chromium 3d and oxygen 2p orbitals in the chromites and between the iron 3d and oxygen 2p orbitals in the ferrites, than between the oxygen 2p and any other transition metal 3d orbitals considered. The extra fine structure in the oxygen K-edges was therefore considered to be dominated by transitions to p-d hybrid

states formed between the oxygen 2p and chromium 3d orbitals in the chromites and oxygen 2p and iron 3d orbitals in the ferrites.

As discussed in section 6.1, the L_3 and L_2 edges of the cations result from the excitation of 2p electrons into empty 3d states. In general the fine structure on these edges is described in terms of atomic multiplet effects. However, since some of the fine structure on the oxygen K-edges has been assigned to transitions to oxygen 2p / metal 3d hybrid states, it would be reasonable to expect some deviation of the L_3 and L_2-edge ELNES from that predicted by a purely atomic model. In figure 7.1 the oxygen K-edges and chromium L_3 edges have been aligned and overlaid for the chromites. The spectra have been normalised to the intensity of the first main peak in each spectrum, so that the oxygen K-edges and chromium L_3 edges can be compared in this region, *i.e.* before the onset of the L_2-edge. A similar approach has been taken for the oxygen K-edges and the L_3 edges of the ferrites and is also shown in this figure.

Close examination of this figure shows that some of the subtle variations observed in the fine structure on both the oxygen and metal edges have similar relative energy separations. Lines have been drawn through pairs of features of this type. In section 6.2.1 splitting of this type on the chromium L_3 and L_2 edges was related to crystal field effects. The regions in which it is observed in the oxygen K-edges are on features that have been assigned to transitions to pd hybrid states. Therefore these features on the oxygen K-edge may results from transitions to oxygen 2p orbitals hybridised with different types of 3d-orbitals. For example, oxygen 2p orbitals hybridised with chromium e_g orbitals, or with chromium t_{2g}

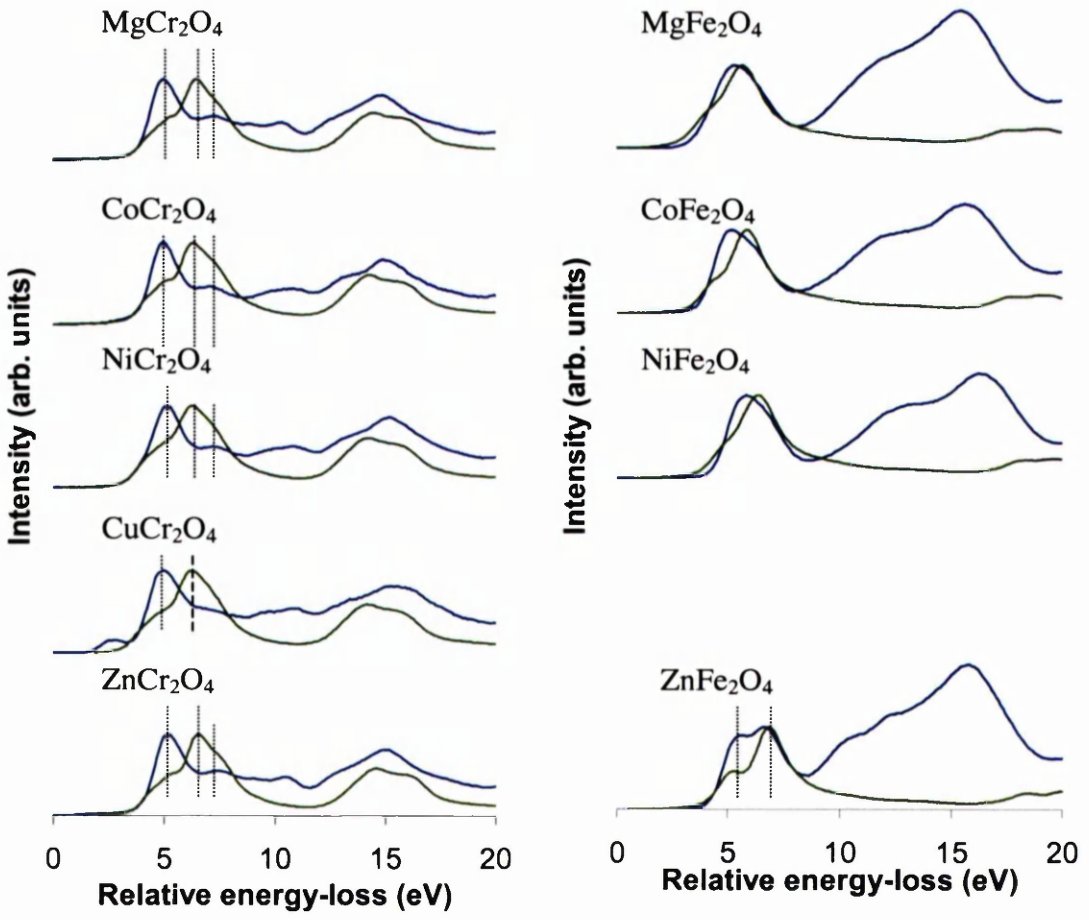

Figure 7.1 *Comparison of the oxygen K-edges (blue) and chromium L_3 and L_2 edges (green) in the chromites, and of the oxygen K-edges (blue) and iron L_3 and L_2 edges (green) in the ferrites.*

orbitals, would give different types of overlap resulting in distinct features in the fine structure.

For the chromites a correlation can be drawn between both the oxygen and metal L_3-edges for three features in the fine structure in all cases except copper chromite. In the spectra from this material the feature at highest energy-loss is not distinct in the oxygen K-edge. It is interesting to note that this is the chromite spinel that has the biggest structural distortion

due to the Jahn-Teller effect. The effect of cubic to tetragonal phase transformations on the fine structure will be discussed in section 7.3.2.

For the ferrites, a similar correlation can be drawn between the iron L_3 edge and the oxygen K-edge for zinc ferrite. Two distinct features in the oxygen K-edge fine structure, which were assigned to transitions to oxygen 2p and iron 3d hybrid states in section 5.4 have a similar energy separation to the splitting in the iron L_3 edge. In section 6.2.2 this splitting in the L_3 edge was related to crystal field effects. For the other ferrites similarities between the metal and oxygen edges cannot be so readily observed. This is mainly because there is more broadening in the oxygen K-edges of the ferrites than of the chromites. In section 5.4 this was attributed to the inversion in all of the ferrites except zinc ferrite, which is normal, and the consequent broadening of the density of states. The effect of inversion on the fine structure will be discussed in section 7.2.

It can also be observed that the main feature on the L_3-edge is the same width as the first main peak on the oxygen K-edge in the case of zinc ferrite. However, for the inverse ferrites the L_3-edge peak is wider than the corresponding oxygen K-edge peak. This is expected since it was shown in section 5.4 that this peak on the oxygen K-edge is due to transitions to states created by hybridisation of oxygen 2p orbitals and iron 3d orbitals from tetrahedrally co-ordinated iron ions. However, the L_3-edge has contributions from iron ions in both tetrahedral and octahedral sites, so is therefore expected to be wider. In the case of zinc ferrite, which is normal, the iron ions only occupy one type of site and the L_3-edge is consequently narrower than for the inverse ferrites.

It is interesting to note that for the pairs of features marked in the spectra from the chromites, a point of maximum intensity on the oxygen K-edge corresponds to a minima on the chromium L_3-edge, and *vice versa*. This inverse correlation suggests that a strong peak on the L_3-edge means the final state wavefunction is highly localised on the metal site and has little effect on the oxygen site. In contrast, the part of the band that hybridises most strongly with the oxygen 2p orbitals is less highly localised and in creating unoccupied states on the oxygen sites, leaves the density of d-character on the metal site depleted. However, for the edges recorded from zinc ferrite, the opposite trend is observed since there is a correlation between points of maximum intensity on the oxygen K-edge and iron L_3-edge, and similarly for point of minimum intensity.

All of the chromites and zinc ferrite are normal. Therefore the change from an inverse correlation in the intensities in the chromites to a direct correlation in zinc ferrite is a consequence of the addition of two electrons to the d-orbitals in the case of the ferrite. It is difficult to explain these observations in a molecular orbital or rigid band model. However, evidence has been presented in sections 5.6 and 6.2 that the single electron view of these systems is inappropriate. In fact, these spinels appear to be highly correlated systems and consequently the addition of extra d-electrons not only fills previously unoccupied levels, but also alters the band structure.

7.1.2 Effect of number of d-holes

It has already been mentioned in this section that changing the metal (III) ion in a spinel from a main group ion to chromium or iron has a large effect on the oxygen K-edge fine

structure, but that substitution of the metal (II) ion has little effect. In section 5.1.2 this was attributed to the large orbital overlap between the chromium 3d orbital and oxygen 2p orbitals in the chromites, and between the iron 3d orbitals and the oxygen 2p orbitals in the ferrites. In section 5.1.1 it was shown that as well as the interaction between the orbitals, the number of holes in the d-orbitals must also be considered to understand the degree of hybridisation taking place. The substitution of chromium or iron for aluminium in the spinel structure introduced a large number of d-holes, whereas substitution of the metal on the tetrahedral site in the chromites and ferrites has a relatively small effect.

It was discussed in sections 6.2.3-6.2.5 that the shoulder on the high-energy side of the L_3 edge of the cobalt, nickel and copper edges could not be reproduced properly in the simulations of Van der Laan and Kirkman. One reason discussed for this broadening was that it was due to transitions to states created by the hybridisation of oxygen 2p and cobalt, nickel or copper 3d orbitals. The addition of p-like character to the d-orbitals would result in broadening of the narrow d-states. Although it has been stated that hybridisation involving chromium or iron orbitals would be much stronger, the higher atomic number first row transition metals could also take part in hybridisation to a weaker extent. It was discussed that the features due to hybrid states in the cobalt, nickel and copper L edges are more dominant than in the corresponding chromium and iron edges because the metal (III) ions have a significant number of extra holes than the metal (II) ions studied. Therefore transitions to the pure d-states, which have a high density of unoccupied states, are favoured in the metal (III) ions. In the case of the oxygen K-edges no states that are purely d-like in character are available for the excited electron to occupy due to the dipole selection rule. They will therefore preferentially reside in the hybrid states that have the

highest density of d-holes, so hybridisation involving chromium and iron is preferred to any of the other transition metal studied. The consideration of the number of d-holes in this way helps to explain why p-d hybridisation is important in the cobalt, nickel and copper L edges but not in those of chromium and iron. It can also be used to predict that p-d hybridisation involving iron and chromium will dominate the oxygen K-edges, and the other transition metals already mentioned will have a fairly insignificant effect.

7.1.3 Metal K-edges

In section 6.5.2 some changes were observed in the magnesium K-edges, the most significant of which was an extra peak in the edge recorded from magnesium chromite. If this peak was due to hybridisation it would be predicted that a similar feature would be present in the magnesium ferrite K-edge. This is not observed, and the differences between these edges are thought to be due to changes in the degrees of inversion between the different compounds, which will be discussed in section 7.2.2. Similarly in the aluminium K-edges subtle changes can be observed which cannot be linked to hybridisation effects and are more likely to be due to changes in the degree of inversion. Hybridisation effects are not expected to be an influence on the aluminium and magnesium K-edges since in these elements the empty d-orbitals are too high in energy to participate in hybridisation. Also, the metal ions in this structure are too far apart for the highly localised d-orbitals of the other transition metal ions in the compound to probe the p-orbitals at the magnesium and aluminium sites.

7.1.4 Peak Energies

In section 5.2.4 it was noted that the edge onset and the main features in the oxygen K-edges occurred at higher energies in the chromites when the metal (II) ion was a transition metals with partially filled d-orbitals, compared to when it was a metal with full or empty d-orbitals. A similar trend was observed in the aluminate spinels. In the case of the ferrites there was a similar pattern with the exception of the zinc ferrite sample. It was shown that this was due to the difference in lattice parameters between zinc ferrite and the other ferrites, and when this was taken into consideration zinc ferrite also matched this trend.

Table 7.1 compares the energies of the edge onsets of the oxygen K-edges in the chromites and inverse ferrites with the energies of the highest point in the chromium and iron L_3 edges. The normal ferrite has not been included due to the discrepancies due to lattice parameter effects already discussed. The energies of the L_2 edges are not given since it has been shown in Table 6.1 that the energy separation between the L_3 and the L_2 edges is constant for all of the chromium and iron edges.

Table 7.1 shows that for all of the chromites studied the spread in the differences between the energies of the oxygen K-edge and chromium L_3 edge is constant to within experimental error. This shows that the energies of the chromium L_3 and L_2 edges shift to higher energies when a second transition metal is incorporated in the spinel structure in the same magnitude as the oxygen K-edge energies move. This trend is also observed in the edges recorded from cobalt ferrite and nickel ferrite, to within experimental error. For

magnesium ferrite the energy difference is slightly larger. It is not clear how significant the difference is in this case compared to the other ferrites.

Compound	Energy-loss (eV)		Difference (eV)
	Oxygen K-edge	Metal (III) L_3-edge	
$MgCr_2O_4$	530.8	577.3	46.5
$CoCr_2O_4$	531.5	577.8	46.3
$NiCr_2O_4$	532.0	578.5	46.5
$CuCr_2O_4$	531.8	578.0	46.2
$ZnCr_2O_4$	531.2	577.7	46.5
$MgFe_2O_4$	540.0	710.1	170.1
$CoFe_2O_4$	540.6	709.9	169.3
$NiFe_2O_4$	541.4	710.9	169.5

Table 7.1 *The energies of the edge onsets of the oxygen K-edges and chromium L_3 edges in the chromites. The error in the energies is ±0.2eV.*

The change in energies as the metal (II) ion is varied suggests that a rigid band model cannot be used to fully describe this system. This model is often applied to describe the alloying process in brass alloys. The electronic structure of the alloy is assumed to be the band-structure of pure copper throughout the concentration range of the alloy and the bands remain unchanged on alloying (Altmann, 1994). However, the constant energy shift in the oxygen K and chromium L_3 and L_2-edges does suggest there is some rigidity in the band structure.

7.2 Effect of inversion on the ELNES

7.2.1 Oxygen K-edges

In section 5.3.2 a pre-peak was observed on the K-edges of magnesium aluminate and nickel aluminate, which are partially inverse, that was not present in the edge recorded from zinc aluminate, which is normal. As discussed in that section, beam damage effects can be discounted as the origin of the pre-peak, and it was tentatively assigned as being due to inversion in the magnesium aluminate sample. This is in agreement with the pre-peak predicted by the calculations of Köstlmeier *et al*, (1999), and van Benthem and Kohl, (2000) for inverse magnesium aluminate, which was not predicted in the normal case. In the case of nickel aluminate further work is required to determine if the origin of this peak is inversion or hybridisation involving nickel 3d and oxygen 2p orbitals.

In the case of the ferrites, zinc ferrite was the only normal sample studied and the other ferrites were highly inverse. As shown in figure 5.1, the first peak in the oxygen K-edge recorded from zinc aluminate displays two distinct features, but the corresponding peak in the oxygen K-edges recorded from the other ferrites is broad with no fine structure. The splitting in the oxygen K-edge of zinc ferrite and lack of splitting in that of nickel ferrite has also been observed by Pong *et al* (1996). They assigned the splitting of the first peak in the spectrum from zinc ferrite to the hybridisation of the oxygen 2p orbitals with the ocathedrally co-ordinated iron t_{2g} and e_g orbitals resulting in two distinct features. They showed that in the case of nickel ferrite, which is inverse, this peak was mainly due to transitions to states created by the hybridisation of the 3d orbitals of iron in tetrahedral sites

and oxygen 2p ions, and the iron ions in the octahedral sites had little influence. Their calculations for nickel ferrite showed broadening of the octahedral site iron 3*d* band, compared to the zinc ferrite case, and a broad featureless band for the tetrahedral site iron 3*d* band. This explains why the splitting of this peak is not observed for nickel ferrite, and can probably be applied to the other inverse ferrites.

7.2.2 Metal K-edges

In section 6.5.2 the magnesium K-edges recorded from magnesium aluminate, magnesium chromite and magnesium ferrite were presented. There were three peaks common to all the spectra, although their relative intensities varied. The spectrum recorded from magnesium chromite also had a shoulder on the low-energy side of the peak that occurred at the lowest energy-loss in this group of three peaks. This spectrum also exhibited an extra peak at a higher-energy loss which was not observed in the magnesium K-edges recorded from the other types of spinels.

If these features were due to hybridisation effects, it would be expected that they would be present in the magnesium ferrite spectrum, since this compound also contains a transition metal, as in the case of magnesium chromite. It is not surprising that hybridisation is unlikely to be the origin of this extra fine structure. As discussed in section 7.1.3, the empty magnesium d-orbitals are too high in energy to take part in hybridisation, and the chromium and iron d-orbitals are highly localised and too far away from the magnesium orbitals to interact with them.

The aluminium K-edges recorded from magnesium aluminate, nickel aluminate and zinc aluminate were presented in section 6.5.3. In contrast to the magnesium K-edges, the same features were observed for all of the compounds, albeit with varying relative intensities. The only other significant difference between the edges was the width of the main peak. It was noted that the width became greater as the degree of inversion in the sample increased. This was explained by considering that the edge had contributions from aluminium ions in both octahedral and tetrahedral co-ordination in the inverse spinels, but only tetrahedral co-ordination in the normal case.

In sections 6.5.2 and 6.5.3 the calculations of Mo and Ching (1996) of the site and symmetry projected DOS of normal and inverse magnesium aluminate showed that cation exchange during inversion leads to a broadening of the partial DOS. In these sections the importance of medium-range order on the fine structure was illustrated by the calculations of Cabaret *et al* (1996), Cabaret *et al* (1998) and Mottana *et al* (1998) for the magnesium and aluminium K-edges recorded from other minerals. The results of these simulations correlate with the experimental observations that cation exchange leads to broadening of the fine structure. This may also explain why extra fine structure is observed in the magnesium K-edge from magnesium chromite, since this compound is normal. The broadening in the magnesium K-edge spectra of the other magnesium-containing compounds, which are inverse, may obscure these features.

7.2.3 L_3 and L_2-edges

One of the best examples of the effect of inversion on the L_3 and L_2 edges is consideration of the ferrites. Figure 6.5 shows these edges from the four ferrites studied. The features are sharpest in the edges from zinc ferrite, which is the only normal ferrite. Broadening is observed on the edges from the other ferrites, which are highly inverse. In this figure the simulations of van der Laan and Kirkman (1992) have been compared to the experimental data. For accurate comparison, the simulated spectra are superpositions of the spectra simulated for iron in tetrahedral and octahedral co-ordination in the correct proportions to give the desired inversion parameter. As for the experimental data, broadening is observed on the edges simulated for the inverse spinels. However, it is consistently less than the experimental broadening indicating there are other factors that have an important influence on these edges.

It appears that the degree of inversion has a larger effect on the oxygen K and metal K-edges. A possible reason for this is that the d-states are far more highly localised than the p states, and are less affected by changes in medium range order. Therefore there is less influence on the fine structure observed on the L_3 and L_2 edges.

7.3 Effect of structural changes on the ELNES

7.3.1 Lattice parameter effects

The Rietveld refinement of neutron and X-ray diffraction data gave the lattice parameters for all of the compounds studied. These results are presented in table 4.2. The aluminates and chromites all had similar sizes of unit cell, within each set. The inverse ferrites had unit cells of similar dimensions, but the lattice parameters of zinc ferrite, which is normal, were larger. This is due to the effects of the larger metal (II) ion occupying the smaller tetrahedral sites, as discussed in section 1.5.1.

Table 5.2 showed that the energy differences between the edge onset and features of interest on the oxygen K-edges were constant to within experimental error within each group for the chromites, aluminate and inverse ferrites, but the energies recorded from the zinc ferrite edge did not match this trend. In section 5.1.4 the effect of the change in lattice parameters on the energy-losses at which features on the edges occurs was considered to explain this observation. It followed the discussion of de Groot (1994) that there is an inversely proportional relationship between the energy difference from the edge onset to a particular feature, and the square of the lattice parameter. The energy separation between the edge onset and first main peak on the oxygen K-edge from zinc ferrite was found to be smaller than the same separation in the other ferrites. When the change in lattice parameter was considered, the energy difference between the features in the zinc ferrite oxygen K-edge became consistent with the other ferrites.

7.3.2 Cubic to tetragonal phase transformations

In section 1.5.2 one of the problems discussed in using spinels as a set of standard materials was that the majority are cubic, but some are tetragonal. Out of the spinels examined all are cubic with the exception of nickel chromite and copper chromite, which undergo a Jahn-Teller distortion to give a tetragonal structure. In terms of the pseudo-cubic cell, as opposed to the conventional tetragonal cell specified in Table 4.2, the *c/a* ratios are 1.02 and 0.91, respectively. Nickel chromite is only weakly tetragonal and undergoes a cubic to tetragonal phase transformation at 320K (Crottaz *et al*, 1997).

The oxygen K-edges recorded from the chromites were displayed in figure 5.1. and a detailed examination of the edge onset in figure 5.6 showed that there was broadening of the edge at the onset in the nickel chromite edge, and a distinct pre-peak in the copper chromite edge, which were not present for the other chromites. A number of reasons for this additional intensity were discounted and it was assigned to being a signature for tetragonality in the sample, although a more extensive study would be required to confirm this.

The Jahn-Teller effect results in redistribution of the d-orbitals. Therefore it is not unreasonable to expect to observe changes in the metal L_3 and L_2 edges between spinels which are cubic and tetragonal. The only copper L_3 and L_2 edges were recorded from copper chromite, so no comparison can be made for cubic and tetragonal materials containing copper. The nickel ion in nickel chromite exclusively occupies tetrahedral sites. In the other nickel-containing spinels the nickel ion is dominantly in octahedral sites, so it

is difficult to make a fair comparison of the effect of the tetragonal distortion on the L_3 and L_2 edges.

7.4 Summary

The aim of this chapter was to correlate the influence of a number of structural and electronic effects on the fine structure on the metal and oxygen edges. It has been shown that changes in the fine structure can be related to a number of factors such as hybridisation between the transition metal d orbitals and oxygen p orbitals, the degree of inversion, and changes in the structure of the spinels. The major changes in the ELNES are observed in the oxygen K-edges. Significant effects are also observed in the magnesium and aluminium K-edges, but the changes are far more subtle on the L_3 and L_2 edges. This may be because the K-edges result from transitions to states which are predominantly p-like in character and the L_3 and L_2 edges are due to transitions which are mainly d-like in character. The d-states are much more highly localised than the p-orbitals and may therefore be less perturbed by changes in the local environment than the spatially extended p-orbitals.

Chapter 8

Conclusions and further work

8.1 Conclusions

The aim of this project was to improve the understanding of the fundamental interactions that give rise to ELNES by systematically studying a series of spinels. In particular the effect of the occupancy of the d-orbitals of the metal ions was to be investigated by systematically varying the metals present in the structure. The interpretation of the experimental data was to be aided by simulation of the fine structure using multiple scattering calculations.

Spinels were chosen as a suitable class of materials since they have a well-defined structure. A series of spinels were synthesised which would allow the effect of a variety of

metals in octahedral and tetrahedral co-ordination on the ELNES to be investigated. To use them as standards in the ELNES experiments, and to model the ELNES data as precisely as possible it was vital that they were well characterised, since a number of spinels deviate from their ideal structure, as discussed in Chapter 1. A number of techniques, described in Chapter 4, were used, and where possible the same results from different techniques were compared and shown to be in good agreement.

The largest effect on the ELNES observed was that substitution of the metal (III) ion from a group III metal to a transition metal resulted in extra fine structure on the oxygen K-edge. This was assigned to transitions to states arising from the hybridisation of the oxygen 2p orbitals and the 3d orbitals of the transition metal (III) ion. Substitution of the metal (II) ion had little effect on the fine structure and this was explained by considering the number of d-holes in each transition metal ion, and the orbital overlap between the oxygen 2p and metal 3d orbitals which are important factors in hybridisation. It was shown that the substitution of the group (III) ion had the largest effect on the number of d-holes per formula unit. The orbital overlap was considered in terms of the p-d coupling constant. This was shown to be greatest between the oxygen 2p orbitals and transition metal (III) ions than between the oxygen 2p orbitals and transition metal (II) ions. Weak fine structure, which is thought to have a contribution from transitions to hybrid states, was observed on the cobalt, nickel and copper L_3 edges. It is thought that this is not present on these edges from transition metals further to the left of the first row because they have a higher density of d-holes, and transitions to these states are favoured over transitions to the hybrid states. A trend was also observed that the position of the edge onset and features in the oxygen K-edge were at highest energies in spinels which contained two transition

metals, and lowest when only group (III) metals were present. The same trend was observed in the chromium and iron L_3 and L_2 edges as the metal (II) ion was substituted.

Changes in the fine structure were also observed which could be related to the degree of inversion in the samples. In particular a pre-peak was observed on the oxygen K-edge recorded from magnesium aluminate, which is partially inverse. The calculations of Kostlemeier *et al* (1999) and van Bethem and Kohl (2000) predicted a pre-peak for inverse magnesium aluminate, but not for the normal case. The pre-peak was not observed in the same edge recorded from zinc aluminate, which is normal. The pre-peak was therefore assigned to being a signature for inversion. A similar feature was observed on the oxygen K-edge recorded from nickel aluminate, but it is unclear if this is due to inversion or hybridisation effects in this case. Inversion was also observed to add broadening to the oxygen K, metal K and metal L edges recorded. In the case of the metal K edges this is in agreement with the calculations of the site and symmetry projected DOS at the magnesium and aluminium sites in normal and inverse magnesium aluminate by Mo and Ching (1996). Similar results were also obtained by Pong *et al* (1996) for the oxygen K-edges recorded from some of the ferrites used in this study. This broadening is expected since the metal ions occupy both octahedral and tetrahedral sites in partially inverse spinels. Changes in the degree of inversion were not observed to have any effect on the energies of features on the edges.

Another case in which a pre-peak was observed on the oxygen K-edge was in the spectrum recorded from copper chromite. This compound is normal so the feature is not due to inversion in this case. It has been assigned to the compound being tetragonal, and having a

c/a ratio of 0.91. The other compound studied which was weakly tetragonal was nickel chromite, which has a c/a ratio of 1.02. The oxygen K-edge recorded from nickel chromite had some broadening at the edge onset but a clear pre-peak was not observed. This may be because the effect is so weak for this compound. The other factor which could influence it is that nickel chromite undergoes a tetragonal to cubic phase transformation at 320K (Crottaz *et al*, 1997). The energetic electron beam used to excite the core electrons may induce this transformation. It would be interesting to repeat this experiment using a cooling stage so that the spectrum could be recorded at a temperature further away from the transition temperature. To confirm that there is a link between the pre-peak and tetragonality would require the study of a more extensive range of spinels which have a tetragonal structure.

The oxygen K-edges from the chromites and magnesium aluminate were simulated using the multiple scattering code FEFF, version 8. Good agreement was obtained for the magnesium aluminate edge when a large cluster was used. Examples were cited from the literature in which the magnesium and aluminium K-edges were simulated from similar minerals to spinel. In those cases a large cluster size was also necessary for accurate reproduction of the experimental features, again showing the importance of medium range order on the ELNES. It would be interesting to simulate the aluminium and magnesium K edges which were recorded from the spinels, but time did not permit this. The agreement between the experimental and simulated spectra for the oxygen K-edges from the chromites was much poorer than obtained with magnesium aluminate. Pseudopotential calculations also failed to reproduce the fine structure satisfactorily. It was suggested that the reasons for this might be the failure of these calculations to account for magnetic

interactions. Examples were cited from the literature that showed the influence of magnetic interactions on the electronic structure of chromite and ferrite spinels. Therefore it would be interesting to repeat these simulations using a suitable code in which magnetic interactions could be incorporated in the calculations.

8.2 Further work

The aim of studies of this type is to gain a fundamental understanding of the ELNES for a system in which the structure and chemistry of the compounds are well understood, so the same technique can be applied to poorly characterised samples. In Chapter 1 examples of spinels that have industrial applications were given. Many of the technologically important spinels have complex structures that often include dopants. The ultimate goal of a study of this type is to be able to use ELNES to characterise materials of this type.

This study has produced a good basic understanding of many of the fundamental interactions which influence the ELNES in spinels. By incorporating a wider range of samples in the study the fingerprints suggested for inversion and tetragonality could be confirmed or denied. Further work on the simulations could give information about important factors which are not being considered at present, such as magnetic interactions. It would be important to gain an understanding of these for accurate interpretation of the fine structure from the important ferrite spinels for example. The application of this technique could then be extended to studying technologically important spinels. Results are attainable by this method with much higher spatial resolution than by other techniques

available, and could be valuable in understanding the electronic and structural properties of spinels and subsequently improving their performance in a variety of applications.

Appendix 1

The definition of Green's functions and their relationship to the density of states

For a partial differential equation of the general form

$$(H(r)-E)\Psi(r)=0 \tag{A1.1}$$

where H(r) is a general Hermitian operator, the Green's function is defined as the solution of the equation

$$(H(r)-E)G(r,r',E)=-\delta(r-r') \tag{A1.2}$$

In terms of the eigenvalues E_n and eigenfunctions $\Psi_n(r)$ of the defining operator

$$(H(r)-E_n)\Psi_n(r)=0 \tag{A1.3}$$

the $\Psi_n(r)$ will form a complete set of orthonormal functions, in terms of which we can write

$$G(r,r',E)=\sum_{n,n'}G_{n,n'}\Psi_n(r)\Psi_{n'}(r) \tag{A1.4}$$

Then

$$(H(r)-E)G(r,r',E)=\sum_{n,n'}G_{n,n'}(E-E_n)\Psi_n(r)\Psi_{n'}^*(r') \tag{A1.5}$$

i.e.

$$\delta(r-r')=\sum_{n,n'}G_{n,n'}(E_n-E)\Psi_n(r)\Psi_n^*(r') \tag{A1.6}$$

Since

$$\sum_n\Psi_n(r)\Psi_n^*(r')=\delta(r-r') \tag{A1.7}$$

then,

$$G_{nn'} = \frac{\delta_{nn'}}{E - E_n} \tag{A1.8}$$

and

$$G(r,r',E) = \sum_n \frac{\Psi_n(r)\Psi_n^*(r')}{E - E_n} \tag{A1.9}$$

An imaginary infinitesimal quantity i0 is usually added to the denominator of the right hand side of equation A1.9, since otherwise the Green's function is undefined when $E=E_n$. Hence

$$G(r,r',E) = \sum_n \frac{\Psi_n(r)\Psi_n^*(r')}{E + i0 - E_n} \tag{A1.10}$$

Equation A1.9 is of the form

$$\int_{-\infty}^{\infty} (E-a)^{-1} f(E) dE \tag{A1.11}$$

for f(E) a well behaved function, and can be solved by defining the principal value P, which is obtained by removing a small area from a-ε to a+ε, where ε is a very small quantity from the range of integration. However, it is better to include this quantity by integrating along a path close to the real axis, while avoiding the pole at E=a. A possible integration path is where the contour follows the real path plus an infinitesimally small semicircle along

$$z = a + \exp i\theta \tag{A1.12}$$

which carries the contour around the pole. Substituting A1.12 for a in equation A1.11, making the change of variable $dE=i\theta\varepsilon\exp i\theta$, and integrating from π to 0 gives the solution of $(-i\pi f(a))$. Hence the Green's function can also be defined as

$$G(r,r',E) = P\sum_n \frac{\Psi_n(r)\Psi_n^*(r')}{E - E_n} - i\pi \sum_n \Psi_n(r)\Psi_n^*(r')\delta(E - E_n) \tag{A1.13}$$

Equation A1.6 follows from equation A1.13 since operating with (E-H) on Ψn gives $(E-E_n)\Psi_n$, cancelling the denominator, and $\Sigma_n \Psi_n(r)\Psi_n^*(r)$ is the unit operator $\delta(r-r')$. In a region of space excluding r=r', equation A1.6 reduces to the Schrodinger equation, since the right hand side will be zero.

The local density of states is defined as

$$n(E,r) = \sum_n \Psi_n(r)\Psi_n^*(r')\delta(E-E_n) \qquad \text{(A1.14)}$$

Hence from comparing equations A.13 and A1.14 it is obvious that

$$n(E,r) = -\frac{1}{\pi}\mathrm{Im}(G(r,r',E)) \qquad \text{(A1.15)}$$

It can be shown (Inkson, 1984), that for the time-dependent Green's function, G(r,r',t,t') which is a solution to the time-dependent Schrodinger equation,

$$\Psi(r,t) = \int G^R(r,r',t-t')\Psi(r',t')dr' \qquad \text{(A1.16)}$$

where G^R(r,r',t-t') is the retarded Green's function. Hence if we know the eigenfunction at some particular space-time point, r',t', the Green's function tells us how the wavefunction develops in time, or how the particle described by the wave function propagates.

References

Altmann, S., Band theory of solids: an introduction from the point of view of symmetry, 1994, Oxford, Clarendon Press.

Aly, M. and Baumgarten, E., App. Cat. A (2001) **210** 1.

Andersen, O.K., Phys. Rev. B (1975) **12** 3060.

Ankudinov, A.L., Ravel, B., Rehr, J.J. and Conradson, S.D., Phys. Rev. B (1998) **58** 7565.

Aritani, H., Tanaka, T., Funabiki, T., Yoshida, S., Kudo, M. and Hasegawa, S., J. Phys. Chem. (1996) **100** 5440.

Banerjee, S. K., O'Reilly W. and Johnson, C. E., J. App. Phys. (1967) **38** 1289.

Baudour, J. L., Bouree, F., Fremy, M. A., Legros, R., Rousset, A. and Gillot, B., Physica B (1992) **180&181** 97.

Blasse, G. and Fast, J.F., Philips Res. Rep. (1962) **18** 393.

Blasse, G., Philips Res. Rep. Supp. (1964) No.3.

Borg, R.J. and Dienes, G. J., The Physical Chemistry of Solids, 1992, Academic Press Inc.

Bugaev, L.A., Ildefonse, P., Flank, A.M., Sokolenko, A.P. and Dmitrienko, H.V., J. Phys. Cond. Matt. (1998) **10** 5463.

Burdett, J. K., Chemical Bonding in Solids, 1995, Oxford University Press.

Cabaret, D., Sainctavit, P., Ildefonse, P. and Flank, A.M., Am. Min. (1998) **83** 300.

Cabaret, D., Sainctavit, P., Ildefonse, P. and Flank, A.M., J. Phys. Cond. Mat. (1996) **8** 3691.

Corradi, A.B., Leonelli, C., Manfredini, T., Pozzi, P. and Romagnoli, M., Am. Cer. Soc. Bull. (1993) **72** 63.

Cox, P.A., Transition Metal Oxides: An Introduction to their Electronic Structure and Properties, 1995, Oxford University Press.

Craven, A.J. J. Mic. (1995) **180** 250.

Craven, A.J. and Buggy, T.W., Ultramic. (1981) **7** 27.

Crottaz, O., Kubel, F. and Schmid, H., J. Mat. Chem. (1997) **7** 143.

David, W.I.F., Ibberson, R.M. and Mathewman, J.C., Report RAL-92-032, (1992) Rutherford Appleton Laboratory, U.K.

Davisson, G. and Germer, L.H. Phys. Rev. (1927) **30,** 705.

De Broglie, L. Ann. De Physiques (1925) **3** 22.

De Groot, F.M.F., Grioni, M., Fuggle, J.C., Ghijsen, J., Sawatzky, G.A. and Petersen, H. Phys. Rev. B (1989) **40** 5715.

De Groot, F.M.F., Sol. Stat. Comm. (1994) **92** 991.

De Guire, M.R., O'Handley, R.C. and Kalonji, G., J. App. Phys. (1989) **65** 3167.

Dunitz, J. D. and Orgel, L. E., J. Phys. Chem. Solids (1957) **3** 20.

Durham, P.J., Chem. Anal. (1988) **92** 53.

Egerton, R.F, Electron energy-loss spectroscopy in the electron microscope, 2nd edition, 1996, New York; London: Plenum.

Elsässer, C., private communication (2000).

Fletcher, D.A., McMeeking, R.F. and Parkin, D.J., Chem. Inf. Comput. Sci. (1996) **36** 746.

Fischer, D.W., J. App. Phys. **41** (1970) 3922.

Fischer, D.W., Phys. Rev. B **5** (1972) 4219.

Freyria Fava, F., Baraille, I., Lichanot, A., Larrieu, C. and Dovesi, R., J. Phys.: Cond. Matt. (1997) **9** 10715.

Fritsch, S., Sarrias, J., Brieu, M., Couderc, J.J., Baudour, J.L., Snoeck, E. and Rousset, A., Sol. Stat. Ionics (1998) **109** 229.

Garvie, L.A.J. and Craven, A.J., Phys. Chem. Minerals (1994) **21** 191.

Garvie, L.A., Craven, A.J. and Brydson, R. Am. Min. (1994) **79** 411.

Glen, G.L. and Dodd, C.G., J. App. Phys. (1968) **39** 5372.

Gobbi, G. C., Christoffersen, R., Otten, M. T., Miner, B., Buseck, P. R., Kennedy, G. J. and Fyfe, C. A. , Chem. Letters (1985) 771.

Goldstein, J.I., Scanning Electron Microscopy and X-ray Microanalysis: A Text for Biologists, Materials Scientists and Geologists", 2nd Edition, 1992, New York; London: Plenum.

Grioni, M., Czyzyk, M.T., de Groot, F.M.F., Fuggle, J.C. and Watts, B.E., Phys. Rev. B (1989) **39** 4886.

Hahn, T., International Tables for Crystallography, 4th ed., 1995, Kluwer Academic Publishers.

Hansen, P.L., Brydson, R., McComb, D.W. and Richardson, I., Microsc. Micoanal. And Microstruct. **5** (1994) 173.

Harris, V. G. , Williams, C. M., Abe, M. and Zhang, Q., J. de Phys. IV (1997) **7** C2 1155.

Harrison, W.A., Electronic structure and the properties of solids, 1980, Freeman.

Hébert-Souche, C., Louf, P.H., Blaha, P., Nelhiebel, M., Luitz, J., Schattschneider, P., Schwarz, K. and Jouffrey, B., Ultramic. (2000) **83** 9.

Heine, V., Sol. Stat. Phys. (1980) **35** 1.

Henry, N.F. and Lonsdale, K.Y., The International Tables for X-ray Crystallography Vol. I, 1969, Kynoch Press.

Hohenberg, P. and Kohn, W., Phys. Rev. (1964) **136** B864.

Ildefonse, P., Calas, G., Flank, A.M. and Lagarde, P., Nuc. Inst. Meth. B (1995) **97** 172.

Inkson, J.C., Many-body theory of solids: an introduction, 1983, New York, Plenum Press.

Jebarathinam, N.J., Eswaramoorthy, M. and Krishnasamy, V., Bull. Chem. Soc. Jap. (1994) **67** 3334.

Jeyadevan, B., Tohji, K. and Nakatsuka, K., J. App. Phys. (1994) **76** 6325.

Kamiyama, T., Haneda, K., Sato, T., Ikeda, S. and Asano, H., Sol. Stat. Comm. (1992) **81** 563.

Knoll, M. and Ruska, E. Z. Physik (1932) **78**, 318.

Kohn, W. and Rostoker, N., Phys. Rev. (1954) **94** 1111.

Kohn, W. and Sham, L.J., Phys. Rev. (1965) **140** A1133.

Korringa, J., Physica (1947) **13** 392.

Köstlmeier, S., Elsässer, C., Meyer, B. and Finnis, M.W., Phys. Stat. Sol. (a) (1998) **166** 417.

Köstlmeier, S. and Elsässer, C., Phys. Rev. B (1999) **60** 14025.

Krivanek, O.L., Ahn, C.C. and Keeney, R.B., Ultramic. (1987) **22** 103.

Krivanek, O.L. and Paterson, J.H. Ultramic. (1990) **32** 313.

Kuznetsov, M.V., Pankhurst, Q.A. and Parkin, I.P., J. Mat. Chem. (1998) **8** 2701.

Langford, J.I. and Louer, D., Rep. Prog. Phys. (1996) **59** 131.

Leapman, R.D. and Grunes, L.A., Phys. Rev. Lett. (1980) **45** 397.

Leapman, R.D., Grunes, L.A. and Fejes, P.L. Phys. Rev. B (1982) **26** 614.

Lie, K., Holmestad, R., Marthinsen, K. and Høier, R., Phys. Rev. B (1998) **57** 1585.

McClure, D. S., J. Phys. Chem. Solids (1957) **3** 311.

McComb, D.W., Hansen, P.L. and Brydson, R., Microsc. Microanal. Microstr. (1991) **2** 561.

McComb, D.W., Brydson, R., Hansen, P.L. and Payne, R.S., J. Phys.: Condens. Matter (1992) **4** 8363.

McKie, D. and McKie, C., Crystalline Solids, 1974, London, Nelson.

Manoharan, S.H. and Patil, K.C., J. Am. Ceram. Soc. (1992) **75** 1012.

Mattheiss, L.F., Phys. Rev. B (1964) **133** A1399.

Metz, R., Caffin, J. P., Legros, R. and Rousset. A., J. Mat. Sci. (1989) **24** 83.

Millard, R. L., Paterson R. C. and Hunter, B. K., Am. Min. (1995) **80** 885.

Mo, S.D. and Ching, W.Y., Phys. Rev. B (1996) **54** 16555.

Mocala, K. and Navrotsky, A., J. Am. Ceram. Soc., (1989) **72** 826.

Moriwake, H., Tanaka, I., Oba, F. and Adachi, H., Jap. Journ. App. Phys. Part 1 (2000) **39** 513.

Morrison, T.I., Brodsky, M.B., Zalzuzec, N.J. and Sill, L.R., Phys. Rev. B (1985) **32** 3107.

Mottana, A., Murata, T., Marcelli, A., Della Ventura, G., Cibin, G., Wu, Z.Y. and Tessadri, R., J. App. Cryst. (1998) **31** 890.

Murthy, K.S.R.C. and Ghose, J., J. Cat. (1994) **147** 171.

Okamoto, J.K., Pearson, D.H., Ahn, C.C. and Fulz, B., in Transmission Electron Energy Loss Spectrometry in Materials Science, ed. Disko, M.M., Ahn, C.C. and Fulz, B., 1992, p.183, The Minerals and Metals Society, Warrendale, Pennsylvania.

O'Neill, H.S., Eur. J. Min. (1992) **4** 571.

O'Neill, W., Virgo, D. and Annersten, H., Am. Min. (1992) **77** 725.

O'Neill, H.S. and Dollase, W.A., Phys. Chem. Min. (1994) **20** 541.

Parkin, I.P., Affleck, I., Aguas, M.D., Cross, W., Kuznetsov, M., Pankhurst, Q.A. and Steer, A., Abstr. Pap. Am. Chem. Soc. (1999) 217:527-INOR.

Paterson, J.H. and Krivanek, O.L. Ultramic. (1990) **32** 319.

Paxton, A.T., van Schilfgaarde, M., MacKenzie, M. and Craven, A.J., J. Phys.: Cond. Matt. (2000) **12** 729.

Pearson, D.H., Ahn, C.C. and Fulz, B., Phys. Rev. B (1993) **47** 8471.

Pénicaud, M., Siberchicot, B., Sommers, C.B. and Kubler, J., J. Magn. Magn. Mat. (1992) **103** 212.

Peterson, R. C., Lager, G. A. and Hitterman, R. L. Am. Min. (1991) **76** 1455.

Pickett, W.E., Comp. Phys. Rep. (1989) **9** 115.

Pong, W.F., Su, M.H., Tsai, M.H., Hsieh, H.H., Pieh, J.Y., Chang, Y.K., Kuo, K.C., Tseng, P.K., Lee, J.F., Chung, S.C., Chen, C.I., Tsang, K.L. and Chen, C.T., Phys. Rev. B (1996) **54** 16641.

Rehr, J.J., Jap. Journ. App. Phys. Supp. (1993) **32-2** 8.

Rez, P., Weng, X. and Ma, H., Microanal and Microstruct. (1991) **2** 143.

Rez, P., Bruley, J., Brohan, P., Payne, M. and Garvie, L.A.J., Ultramic. (1995) **59** 159.

Roelofsen, J.N., Peterson, R.C. and Raudsepp, M., Am. Min. (1992) **77** 522.

Schläfer, H.S. and Gliemann, Inorg. Chem. (1969) **8** 1137.

Schmocker U. and Waldner, F., J.Phys.C: Solid State Phys. (1976) **9** L235.

Seah, M.P. and Dench, W.A., Surf. Interface. Anal. (1979) **1** 2.

Skriver, H.L., The LMTO method, 1984, Springer, Berlin.

Slater, J.C. and Johnson, K.H., Phys. Rev. B **5** (1972) 844.

Smart L. and Moore, E., Solid State Chemistry: An Introduction, 1995, Chapman and Hall.

Smith, R.I. and Hull, S., Report RAL-94-115 (1994) Rutherford Appleton Laboratory, Oxon, U.K.

Sparrow, T.G., Willimas, B.G., Rao, C.N.R. and Thomas, J.M., Chem. Phys. Lett. (1984) **108** 547.

Stolojan, V., Walsh, C.A., Yuan, J. and Brown, L.M., Inst. Phys. Conf. Ser. (1999) **161** 235.

Thompson, G.P. and Reid, A. Nature (1927) **119**, 890.

Torii, Y., Tsuzuki, A., Kato, K., Uwamino, Y., Choi, B.H. and Lee, M.J., J. Mat. Sci. (1996) **31** 2603.

Van Benthem, K. and Kohl, H., Micron (2000) **31** 347.

Van Bokhoven, J.A., Sambe, H., Ramaker, D.E. and Koningsberger, D.C., J. Phys. Chem. B (1999) **103** 7557.

Van der Laan, G. and Kirkman, I.W., J. Phys. Cond. Matt. (1992) **4** 4189.

Von Dreele, R.B. and Larson, A.C. (1998) GSAS- Generalised Crystal Structure Analysis System, Neutron Scattering Centre, Los Alamos National Laboratory, California.

Weng, X. and Rez, P. Phys. Rev. B (1988) **39** 7405.

Weng, X., Rez, P. and Sankey, O.F., Phys. Rev. B (1989) **40** 5694.

West, A. R., Basic Solid State Chemistry, 1988, John Wiley and Sons Ltd.

Whipple, E. and Wold, A., J. Inorg. Nucl. Chem. (1962) **24** 23.

Williams, A.R. and Kubler, J., Phys. Rev. B (1979) **19** 6094.

Williams, D.B. and Carter, C.B., Transmission electron microscopy: a textbook for materials science, 1996, Plenum.

Wold, A. and Dwight, K., Solid State Chemistry: Synthesis, Structure and Properties of Selected Oxides and Sulfides, 1993, Chapman and Hall Inc.

Wood, B.J., Kirkpatrick, R.J. and Montez, B., Am. Min. (1986) **71** 999.
Yao, T., Imafuji, O. and Jinno, H. J. Am. Ceram. Soc., (1991) **74** 314.

Young, R.A., The Rietveld Method, 1993, Oxford University Press.

Zabinsky, S.I., Rehr, J.J., Ankudinov, A., Albers, R.C. and Eller, M.J., Phys. Rev. B (1995) **52** 2995.